DESIGN AND VALIDATION OF AN IMPROVED HYBRID PNEUMATIC-ELECTRIC ACTUATOR

DESIGN AND VALIDATION OF AN IMPROVED HYBRID PNEUMATIC-ELECTRIC ACTUATOR

By Graham Ashby, B.Eng

A Thesis

Submitted to the School of Graduate Studies

In Partial Fulfillment of the Requirements

For the Degree

Master of Applied Science

McMaster University

MASTER OF APPLIED SCIENCE (2015)

McMaster University

(Mechanical Engineering)

Hamilton, Ontario

TITLE: Design and Validation of an Improved Hybrid Pneumatic-Electric Actuator

AUTHOR: Graham Ashby, B.Eng (McMaster University, Canada)

SUPERVISOR: Dr. Gary M. Bone, Professor

NUMBER OF PAGES: xxvi, 207

Lay Abstract

Robots which work directly with people are becoming increasingly numerous in industry as their costs decrease. As robots and humans work more and more closely there is a desire for the robot to be more inherently safe, by merit of the underlying mechanical design. Previous research resulted in a prototype hybrid pneumatic-electric actuator (HPEA) designed to improve inherent safety by merit of its low inertia, low friction, and low stiffness. This prototype proved successful, but was of low payload capacity and unreliable mechanical design. The goal of the research was to design, build, model, control, and validate a second generation HPEA, with a larger payload capacity and of more reliable mechanical design while maintaining low friction, inertia and stiffness. Furthermore the improved actuator should maintain or improve upon the good position trajectory tracking of the prior actuator. These goals were successfully achieved with the improved prototype developed in this work.

Abstract

As collaborative robotics become more prevalent, it is desirable to improve the inherent robot safety, on a mechanical level, while maintaining good position tracking. One method is to replace the electric motor+gearing currently used with an alternate actuator which introduces less inertia, friction, and stiffness. A promising approach is the use of hybrid pneumatic-electric actuators (HPEAs). A first generation (GEN1), proof-of-concept, HPEA with low payload capacity and poor mechanical reliability was improved upon to produce the next generation of HPEA. The 2nd generation (GEN2) actuator developed in this work was designed to increase payload capacity and improve mechanical reliability while maintaining low inertia, low friction and low stiffness. The torque capacity was improved by 511% while increasing inertia by only 292%.

The majority of the system was modeled via relevant physical laws. The solenoid valves' inverse model was provided by a black box artificial neural network (ANN), and the electric motor's was empirical. The models were used to develop a position controller with an inner loop pressure controller based upon the ANN. An alternate (non-model-based) pressure controller was also developed to compare to the ANN based controllers. The system could operate as a purely pneumatic actuator, or as a HPEA.

Experimentally it was found that the position control based upon the two pressure controllers led to similar performance, but the ANN based were superior more often. The hybrid mode reduced the purely pneumatic mode position error for vertical cycloidal position tracking by approximately 55%. The GEN2 achieved lower position tracking errors as compared to prior works of other HPEAs as well as purely pneumatic actuator control publications. Compared to the GEN1, the GEN2 achieved better position tracking errors in both pneumatic and hybrid operation. The GEN2 will serve as a superior testbed for future HPEA control and collaborative robotics research.

Acknowledgment

First and foremost, my thanks to Dr. Gary Bone, without whom this work would not have been possible. My graduate studies have allowed me to learn a lot and gain skills across a wide variety of topics. Of course this time was made all the better by the support of my colleagues: Mantian Xue, Justin Flett, Yile Zang, Venu Kurella and Kai Xue.

Certainly nothing would ever have been actually made without the excellent technical skills and assistance of Mark, Michael, Joe, John, and Ron.

Finally, thanks to my friends and family who have been nothing but supportive.

Contents

List of Figures

List of Tables

Abbreviations

ALTB: Alternate Pressure Controller Based Pneumatic Position Controller

ANN: Artificial Neural Network

ANNB: ANN Pressure Controller Based Pneumatic Position Controller

ANSI/RIA: American National Standards Institute/Robotics Industries Association

BIBO: Bounded Input Bounded Output

CSA: Canadian Standards Association

DAQ: Data Acquisition System

DVMPC: Discrete Value Model Predictive Control

FANN: Fast Artificial Neural Network

GEN1, GEN2, GEN3: Generation 1, 2 and 3

HANNB: ANN Pressure Controller Based Hybrid Position Controller

HALTB: Alternate Pressure Controller Based Hybrid Position Controller

HPEA: Hybrid Pneumatic-Electric Actuator

IVM1, IVM2: Inverse Valve Model 1 and 2

ISO: International Standards Organization

MAE: Maximum Absolute Error

MB: Model Based

MPWM: Modified Pulse width Modulation

PAM: Pneumatic Artificial Muscle

PD: Proportional Plus Derivative

PID: Proportional Plus Integral Plus Derivative

PTP: Point-to-Point

PWM: Pulse Width Modulation

RMSE: Root Mean Squared Error

RMPSE: Root Mean Squared Pressure Error

SC: Switching Controller

SSE: Steady State Error

Nomenclature

A_{screw}: Area of a single coupling screw.

A_A, A_B: Chamber A and B areas.

A_{pneum}: Total pressure area of each cylinder group.

d_{CW}, $d_{coupler}$, d_{link}, $d_{payload}$: Distance from the point of rotation of the counterweight, coupler, link, and payload.

d_v: Distance between center of bearings and load.

F', F'': Primary and secondary shear.

$F_{bearing}$:Force supported by the angular contact bearings.

$F_{Cyl,push}$ $F_{Cyl,pull}$: Forces of the cylinder groups “pushing” and “pulling” the load.

F_{cyl}, $F_{cyl,N}$, $F_{cyl,T}$: Force produced by each cylinder, and the normal/tangential components at gear meshing.

$F_{g,gear}$ force of gravity due to mass of rack gear.

F_{group1}, F_{group2}: Force produced by the chamber groups 1 and 2.

$F_{loadcell}$:Force measured by the load cell.

$F_{M,payload}$, $F_{v,payload}$: Forces on bearing due to moment and shear effects of the payload.

$F_{preload}$: Preload force on the rack gear, per ball roller.

F_{roller} : Force supported by each ball roller.

g : Gravitational constant.

INV_1, INV_2 : Functions representing the inverse valve models 1 and 2.

J_{total} , $J_{payload}$, J_{shaft} , $J_{cyls+racks}$, $J_{link+CW}$, J_{motor} : Rotational inertias of respective components, with respect to rotation about the output shaft.

k : ratio of specific heats of air.

$K_{P,motor}$, $K_{D,motor}$: Motor proportional and derivative gains.

$K_{P,\theta}$, $K_{D,\theta}$, Position controller proportional and derivative gains for pneumatic components.

$K_{P,pressure}$ $K_{I,pressure}$: Proportional and derivative gains for ANN based controller.

$K_{P,pressure,alt}$, $K_{D,pressure,alt}$, $K_{FF,pressure,alt}$: Alternate pressure controller proportional, derivative, and feedforward gains.

L_{link} : Length of link.

m_{gear} , m_{cyl} , $m_{payload}$, m_{link} , m_{CW} , $m_{coupler}$: Masses of respective components.

$m_{payload,\max}$: Maximum payload mass.

$\dot{m}$, $\dot{m}_{des}$, $\dot{m}_{model}$: Mass flow rate, desired mass flow rate, model based contribution to mass flow rate.

$\dot{m}_1$, $\dot{m}_2$: Mass flow rates through valves 1 and 2.

n_{screw} : Number of screws used in bolt circle.

N_{points} : Number of data points being evaluated.

P , P_{des} : Pressure and desired pressure.

P_1 , P_2 , $\dot{P}_1$, $\dot{P}_2$: Pressures and rates of pressure change in chamber groups 1 and 2.

$\hat{P}_1$, $\hat{P}_2$, $\hat{\dot{P}}_1$, $\hat{\dot{P}}_2$: Estimated pressures and rates of pressure change in chamber groups 1 and 2.

$P_{1,des}$, $P_{2,des}$: Desired pressures in chamber groups 1 and 2.

$\hat{\dot{P}}_{des}$, $\hat{\dot{P}}_{1,des}$, $\hat{\dot{P}}_{2,des}$: Estimated desired pressure rate of change, and desired rates of change in chamber groups 1 and 2.

R : Universal gas constant.

r_{circ} : Radius of bolt circle of coupling screws.

r_{gear} : Pinion gear pitch radius.

r_{ID} , r_{OD} : Inside and outside diameter of link.

r_{piston} , r_{rod} :Radius of cylinder piston and cylinder rod.

T : Ambient temperature.

T_s : Sampling period.

t_i , t_{i-1} : Current sample time, previous sample time.

t_{move} : Length of time for PTP move.

$u_{deadzone}$: Deadzone compensation for valve control signal (duty cycle).

u_{motor} : Motor control signal.

u_{total} , u_{model} : Total control signal (duty cycle) sent to a valve, and model derived portion.

u_1 : Control signal (duty cycle) of valve 1.

$u_{1,INV}$: Control signal (duty cycle) resultant of the inverse valve model for valve 1.

$V_{loadcell}$: Measured loadcell voltage.

v , $\dot{v}$, $v_{deadzone}$: Chamber volume, volume rate of change, and deadzone volume.

$\hat{v}$, $\hat{\dot{v}}$: Estimated chamber volume and volume rate of change.

$v_{1,deadzone}$, $v_{2,deadzone}$: Group 1 and 2 deadzone volume totals.

$v_{1,Bdeadzone}$, $v_{1,tubing}$, $v_{1,Adeadzone}$: Constituent volumes of group 1 deadzone volume.

$v_{2,tubing}$, $v_{2,Bdeadzone}$, $v_{2,Adeadzone}$: Constituent volumes of group 2 deadzone volume.

v_1 , v_2 , $\dot{v}_1$, $\dot{v}_2$: Total volumes and volume rates of change in groups 1 and 2.

$\dot{v}_{A,1}$, $\dot{v}_{B,1}$, $\dot{v}_{A,2}$, $\dot{v}_{B,2}$: Chamber specific volume rates of change.

$w_{bearing}$: Width of each angular contact bearing.

y : Linear position.

$y_{A,1}$, $y_{B,1}$, $y_{A,2}$, $y_{B,2}$: Chamber lengths, per valve group.

$\dot{y}_{\max}$: Maximum linear velocity at tool location.

θ , $\dot{\theta}$, $\ddot{\theta}$: Angular position, velocity, and acceleration.

$\hat{\theta}$, $\hat{\dot{\theta}}$: Estimated angular position, and velocity.

θ_{Des}, $\dot{\theta}_{Des}$, $\ddot{\theta}_{Des}$: Desired angular position, velocity, and acceleration.

θ_{offset}: Offset between system defined 0 and chamber 0 positions.

$\theta_{A,1offset}$, $\theta_{A,1offset}$, $\theta_{A,1offset}$, $\theta_{A,1offset}$: Offset between system defined 0 and chamber specific 0 positions.

$\theta_{neutral}$, θ_{amp}: Sine trajectory shift from neutral=0, and sine amplitude.

θ_{start}, θ_{end}: Angular move starting and ending angular positions.

$\eta_{transmission}$: Pneumatic to output torque efficiency.

$\lambda_{\dot{\theta}}$, $\lambda_{\dot{P}}$: Velocity and pressure rate of change filter coefficients.

$\sigma_{\text{yeild, shear}}$, $\sigma_{\text{yeild, tension}}$: Shear and tension yield stresses.

φ: Sine trajectory phase shift.

ϕ: Rack and pinion gear pressure angle.

τ_{motor}, τ_{pneum}: Motor torque and pneumatic cylinder total torques.

$\tau_{motor,des}$, $\tau_{pneum,des}$: Desired motor and pneumatic torques.

$\tau_{motor,measured}$: Motor torque measured by loadcell.

$\tau_{net,system}$: Net system torque.

$\tau_{g,payload}$, $\tau_{g,link}$: Gravitational torques due to payload and link masses.

τ_{f}: Friction compensation torque.

τ_{f+}, τ_{f-}: Positive and negative friction compensation constants.

$\tau_{f+,offset}$, $\tau_{f-,offset}$: Positive and negative friction offsets.

$\hat{\tau}_{grav}$: Estimated gravitational torque.

$\tau_{inertia}$: Inertial torque.

$\tau_{friction}$: Friction torque.

τ_{*}: Highest stress condition on coupling screws.

ω, ω_s: Cycloidal and sine trajectory angular frequencies.

Chapter 1 – Introduction

1.1 Motivation

Robots have been used industrially for decades, typically in the embodiment of the "robot arm". Robots arms (also known as "manipulators") are used to move tools and/or other objects through a large area around themselves (known as their "workspace") to perform a large variety of tasks. They enable the automation of tasks, but retain flexibility that inflexible or "hard" automated machines cannot match. They are a soft automation tool which can be relatively quickly reprogrammed and/or reconfigured to complete different tasks, as required. Robots can perform tasks that humans are physically incapable of, such as carrying large payloads, following accurate paths, or working in environments that are harmful to humans. Furthermore, robots are capable of performing tasks tirelessly in a repeatable manner. Yet there remain situations, industrial or otherwise, in which it is currently undesirable, impractical, not cost effective, or even impossible to implement a robotic or automation system to replace human workers. For example, a manufacturing line involving irregular materials, or unexpected situations. Or perhaps a disabled person needs assistance in the complex and unpredictable world in which we live. In these situations, and many more, a human is required to accomplish the task. But even so, the human's experience, efficiency and even base capability might be improved through the assistance of a robot. In this way, the complex environment, and high level decision making can be evaluated by the human operator, and their capability in achieving their goals can be augmented via robotics.

Systems in which robots are working directly with or in close proximity to humans fall within the purview of what is called "collaborative robotics". The international industrial standard on the vocabulary of robotic devices, (ISO 8373:2012(en), 2012), defines a collaborative robot as a "robot designed for

direct interaction with a human" and collaborative operation as a "state in which purposely designed robots work in direct cooperation with a human within a defined workspace". Inherent then to collaborative robotics is the close physical proximity between humans and robots. This proximity between relatively powerful machines and relatively fragile humans raises the question of the safety of the human. Robots, unlike most machines, are flexible, and capable of a variety of tasks. This means that though a robot arm might be less capable of physical harm than say a hydraulic press, the robot is capable of more unpredictable behaviour. The press has only a few clear, repeatable functions, which can be easily guarded or indicated as dangerous points. The machine is designed in such a way the human is kept back from moving parts, which are contained in a known area. A human, properly trained, is capable of interacting with the press in a safe manner with high confidence in how the machine will behave, even in the event of a failure in the system. A robot on the other hand is much more variable, and can be programmed to respond in almost infinite ways to external stimuli, depending on the sensors the robot contains.

To reduce risk during collaborative robot operation, industrial standards, such as the Canadian standard CAN/CSA-Z434-14 (CAN/CSA, 2014), have been written. They are built around mitigating risks by controlling the way in which a robot is capable of operating when human(s) are within its working proximity, depending on the task being accomplished. Currently the CAN/CSA-Z434-14 standard requires collaborative robots to be used only for specific, predefined operations which require a risk assessment to establish the specific safety features which must be included for the particular situation. If a major change in the operation is performed the risk assessment must be performed again to ensure it meets the standard. Several possible collaborative scenarios are outlined within CAN/CSA-Z434-14, including:

- **Hand Over Window:** where the robot is otherwise guarded, save for a specific location within the workspace accessible by the human, typically to load/unload objects to/from the robot's area. The robot must operate at a reduced speed near the window, and not otherwise operate near the window.
- **Interface Window:** where the robot stops in specific windows of its work space, and is otherwise guarded. The robot must operate at a reduced speed near this window. Once stopped the robot can be manually moved outside the window. This manual operation requires hold-to-run switches.
- **Collaborative Workspace:** where autonomous operation is allowed within the same workspace where humans could be present. The robot must operate at a reduced speed or stop when a human enters the workspace. A sensor based human detection system must be in place.
- **Inspection:** where the robot can operate autonomously within a guarded collaborative workspace, but when a human enters the collaborative workspace the robot must operate at a reduced speed and a reduced range within the workspace. A sensor based human detection system must be in place.
- **Hand Guided Robot Operation:** Where the human hand guides the robot along a path. The robot must operate at a reduced speed, with a hold-to-run switch, and the workspace allowable is determined by the hazards present.

Anandan (2013), summarized ANSI/RIA R15.06-2012 (2012), the ANSI standard which is based around the same ISO standard (ISO 10218, (2011)) as CAN/CSA-Z434-14 (2014). Anandan outlines that depending on a risk assessment of the particular scenario to operate collaboratively the robot must be limited by at least one of: a safety rated stop, operate by hand guiding, speed and separation monitoring, or be power/force limited.

Regardless of the requirements of the safeguards for the particular situation, the robot itself must also be within the category of "robots with features specifically designed for collaborative operation" CAN/CSA-Z434-14 (2014). A risk assessment of the specific, defined collaborative situation in which the robot specifications (max speed, torque, etc), the end effector properties, and the layout of the robot and workspace, the operators proximity to the robot and the robots path/environment, any other fixtures in the workspace, limitations due to protective equipment, and any other application specific hazards.

The robots which are software limited to reduced speed, acceleration, or force operating conditions for collaborative tasks are still physically capable of larger speeds and torques. These robots could operate in a manner which could cause injury to humans. This could be, for example, due to programming error, sensor failure, or operator error. As such, the safer the robot can be inherently made, the more flexible the applications can become as established by the risk assessment. The cheaper and more available robotic systems become, the more they will be incorporated to augment humans to better achieve tasks. The more prevalent collaborative robots become the more opportunities for failures that could cause human injuries exist. Collaborative robot arms have been under development in academic and industrial research labs for over ten years and several are now being sold (Zinn *et al.* (2004), Anadan, (2013)). For example the Rethink Robotics' Baxter (Rethink Robotics, (2015)), the Universal Robots' UR5(Universal Robots, (2015)), and ABB's YuMi (ABB, (2015)), are commercial robot arms approximately the size of a human arm. This size allows the robots to be more easily incorporated into collaborative settings, which are typically designed to accommodate humans rather than robots.

As more and more robots are designed and marketed for collaborative use, designs have been developed with the goal of being safer for humans than traditional robots. The most common type of robot arm employs six actuated rotary joints connected serially to six rigid links. In the majority of robot arms the

actuator consists of an electric motor connected through high reduction gearing to the next link. It is not uncommon to see robots with gear reduction ratios of 100:1 to 200:1 (Spong, & Vidyasagar (1989)). This high reduction ratio allows for smaller, higher speed motors to be used and be able to produce adequate torque. The gearing has the secondary effect of reflecting (to the output side) the motor's inertia multiplied by the gear ratio squared, which can be as large as 40,000 (200:1 gearing). In addition, high ratio gearing introduces a large amount of friction into a system. Electric motors and gearing have traditionally been used due to their excellent precision, ease of control (due in part to the gears' high stiffness), and the ease of integrating an electric power source. However, due to the large reflected inertia, high stiffness and large friction of the gearing, if the robot was to impact a human, a large force would be transmitted over a short time period with the potential to cause injury (Zinn *et al.* (2004)).

A variety of actuator designs have been developed commercially and in the literature for robots which are more inherently safe. A robot is inherently safe if it does not rely on sensors or software to prevent impacts causing serious injuries. For example, the Baxter robot (Rethink Robotics, (2015)) uses series elastic actuators. The electric actuator is connected to its link through an elastic component. This makes the system much more compliant, so that if an impact does occur the elastic spring compliance reduces the impact. Yet the inclusion of the elastic component also makes the position of the link difficult to precisely control. For example the Baxter has a rated 5-10 mm accuracy (Guizzo & Ackerman, 2012), quite poor for robotics. This is a disadvantage since many applications of robots require precise position control. An alternate approach to inherent safety which has been investigated is by changing the power source of the actuator.

Pneumatic actuators are another actuator type often used in industrial manufacturing, typically for point-to-point motion where precisely following a position trajectory is not important. Pneumatic actuators have the advantage of

high power density while maintaining low inertia. Due to the force capability of pneumatics they can be integrated into a robotic system with little to no gearing required. Without the need for gearing, and the low base inertia, the system does not suffer from the detriments inherent in geared electric robots. Pneumatic actuators also have the benefit of the natural compliance of air. If an impact does occur, the low inertia, and the low friction as well as the compliance of air means that the impact force would be relatively small. Unfortunately pneumatic actuators have several disadvantages for use in a robotic arm. Precise position control is difficult due to nonlinearities influenced by: uncertain friction at seals, valve dynamics, compliance of air and chamber air leakages. The air compliance, while an advantage for impact mitigation, similar to the series elastic actuator, leads to an under damped system with a tendency for oscillation. Pneumatic actuators are also much slower to respond to desired torque changes than electric motors. Additionally pneumatic cylinders require a mechanism to convert linear to rotational motion, where the arrangement and stroke of the cylinder must be considered for overall actuator size.

Pneumatic actuators are capable of generating the necessary torque with a low friction and inertia, yet are difficult to control and respond more slowly. Electric motors are easier to control precisely, and can respond to higher frequency changes, but when acting alone require large ratio gearing leading to large inertia, friction and stiffness. The advantages of each actuator can mitigate the effects of the other's disadvantages so the combination has great potential. As such, prior research has been performed in combining the two actuators together to act as a single hybrid pneumatic-electric actuator (HPEA). By providing the majority of the torque with the pneumatic actuator less inertia and friction are introduced, and an electric motor with low ratio gearing incorporated in series or parallel improves the position tracking performance by correcting higher frequency errors, while introducing minimal friction and inertia. As the majority of the torque typically comes from the pneumatic actuators, HPEAs are typically

capable of being controlled in a purely pneumatic mode, as well as in the hybrid mode, when the electric actuator is also active, in an effort to improve performance. A variety of HPEAs have been investigated in the literature, although their performance was inadequate for use with a robotic arm, and no commercially available robot currently uses a HPEA.

The Robotics and Manufacturing Automation Laboratory (RMAL) at McMaster University has previously developed a HPEA (Chen, 2012) and published two papers on its design and position control: Bone & Chen (2012) and Bone, Xue, & Flett (2015). This HPEA was designed as proof of concept used to develop a variety of purely pneumatic and hybrid control strategies. In this thesis, using this first generation (GEN1) HPEA as a basis, an improved second generation (GEN2) HPEA will be developed.

1.2 Objective and Organization

The primary motivation of this thesis was to design, construct, and validate a HPEA with superior performance compared to the prior GEN1 actuator and other prior HPEAs. The GEN2 will be the next generation of hybrid actuator which can be used for further pneumatic and hybrid control research. Further it is intended that in future work, the GEN2 also be used for direct comparisons to existing geared electric motors, in the context of human safety with collaborative robots. For the aforementioned uses, the following goals were kept in mind when designing the GEN2 HPEA:

1. Increase payload capacity, as compared to the GEN1 actuator, to be similar to that of actuators used in existing collaborative robot arms.
2. Maintain low actuator inertia, and low actuator friction, as in GEN1 actuator.

3. Improve mechanical robustness and reliability, as compared to the GEN1 actuator.
4. Maintain similar, or improve, system performance in terms of position trajectory tracking capability, as compared to the GEN1 actuator.

This thesis is organized into seven chapters including this introduction. Chapter 2 summarizes the most relevant literature in the areas of: HPEA design, pneumatic system modelling and the position control of pneumatic actuators and HPEAs. Chapter 3 presents the mechanical and electrical design of the GEN2 actuator. Chapter 4 presents the mathematical modelling of the system including the overall system dynamics, pneumatic valve/cylinder models, and the electric motor model. Chapter 5 discusses the controller development. Controllers are developed to allow for purely pneumatic actuation as well as hybrid actuation. Two types of controllers are developed for each of the pneumatic and hybrid operation modes, one incorporating on an artificial neural network (ANN) based inverse model of the valves/chambers, and a simpler alternate controller for comparison. Chapter 6 discusses the tuning of the controllers, as well as experiments performed and their results in terms of position tracking capability. The hybrid and pneumatic modes, as well as the ANN-based and alternate controllers are compared and contrasted to one another. The results are compared to the prior art of hybrid actuators (especially the GEN1 system), as well as several purely pneumatic actuators. Finally, in Chapter 7, the content of the thesis is summarized, and suggestions are made for future work for both the direct use of the GEN2 system, and the development of a GEN3 system.

Chapter 2 - Literature Review

2.1 Introduction

The most relevant publications related to HPEA design and control are reviewed in this chapter. Section 2.2 discusses the prior designs of HPEAs. Section 2.3 reviews the valve modeling and pneumatic system dynamics. Section 2.4 presents the relevant control and tracking performance of prior systems in both HPEAs, and the more common purely pneumatic actuators. Finally, Section 2.5 concludes the chapter.

2.2 Design of Hybrid Pneumatic-Electric Actuators

The first appearance of the HPEA concept in the literature was the patent issued to Petrosky in 1988. Since that time a variety of basic system designs have been explored. The common factor between them was the presence of some type of rotary electric motor. In contrast, the pneumatic component varies between designs; pneumatic cylinders, rotary pneumatic motors, and artificial pneumatic muscles have all been used, and in various configurations. Each of these approaches has unique advantages and disadvantages, and could be useful in certain applications.

Petrosky (1988) introduced the basic idea of the HPEA, especially for robotic application in his 1988 issued patent outlining an actuator design. The patent outlines the basic design and expected performance of an actuator which arranged a DC motor in parallel with a vane type rotary pneumatic motor. The justification provided for hybridization centered on the fast response time of electric motor compensating for the comparably slower pneumatic as well as the high continuous torque pneumatic compensating for the lower continuous torque capacity of the electric motor. Petrosky specifically mentioned the usefulness in

the robotic application, where large torques are needed while the actuator is simultaneously stationary. No prototype or further development of the concept by Petrosky was found beyond this patent.

Mills (1990) proposed a hybrid robotic actuator design, as well as relevant system equations of motion and a control law to linearize system dynamics. The system used a DC motor in series with a pneumatic muscle, commonly termed a pneumatic artificial muscle (PAM). Two PAMs, each with a motor in series, were arranged antagonistically around a rotary output shaft (similar to the biological antagonistic muscle arrangement). The arrangement is required for PAMs as they can only exert appreciable force in one direction, contraction with increased pressure. This antagonistic arrangement also allowed for dynamic control of the joint stiffness, as only the net force difference is seen in the output. The primary function of the DC motors was to compensate for muscle length changes, as the muscle force was varied. This allowed for independent control of joint stiffness and joint position, which is not possible with antagonistic PAMs alone due to the PAM coupling of force and length. Simulations were presented to show the closed-loop performance. No practical experiments were performed or discussed.

Later, Takemura *et al.*, (2000) presented a HPEA more similar to Petrosky (1988) than Mills (1990). Takemura intended to more directly make use of the two actuators inherent advantages, whereas Mills included the motors primarily to decouple the PAM force/length relationship. Takemura's design combined, in parallel, a vane type rotary pneumatic motor with a small electric motor. The coupling of the actuators in parallel was achieved by meshing spur gears of various ratios. The electric motor was geared to the pneumatic at a 2:1 ratio, the output link was then geared via a 15:1 ratio of gearing. No justification or analysis of these gearing selections was presented. An apparatus was built and tested.

Shin *et al.* (2009) was a return to the antagonistic PAM approach, though the electric motor was incorporated differently than in Mills (1990). Unlike Mills, only a single electric motor was used, and it was connected in parallel to the antagonistic PAMs' output. This actuator was designed with collaborative robotics and human safety in mind. Due to the parallel arrangement, the stiffness and position control were more coupled than in Mills, though to a degree the stiffness can still be controlled via chamber pressure. The designs of HPEAs for a robot arm with two joints (shoulder and elbow) were presented, with a significant biological inspiration for the link and PAM mounting arrangement.

Bone & Chen (2012) proposed an additional alternate design for a HPEA. The design was comprised of a double acting pneumatic cylinder with an electric motor geared in parallel to a common output shaft. A single, double acting cylinder acted in much the same way as two antagonistic PAMs but could achieve a much better stroke for an equivalent actuator length. Furthermore, pneumatic cylinders do not have the stiffness/length related coupling issue of a PAM. Double acting cylinders do though have the problem of leakage between chambers, and the atmosphere across the cylinder rod. The issue of cylinder friction must be considered, and can be significant, depending on the particular cylinder used. A low friction pneumatic cylinder was coupled via rack and pinion gearing to an output gear. The output gear was rigidly attached to a link. Using a second spur gear, the motor was coupled to the output gear via a 5:1 ratio. The pneumatic cylinder was controlled using two low cost 3-way on/off solenoid valves, as opposed to the more expensive but continuously variable servo proportional valves.

Teramae *et al*., (2013) presented the system modeling and control of a HPEA which combined an electric motor and a single PAM (non-antagonistic arrangement) in parallel. This research was focused less upon HPEAs for robotic use, but on actuators to assist humans in an exoskeleton arrangement. The

actuator arrangement was such that significant amounts of force could only be applied in a single direction.

2.3 System Modeling

The GEN2 system is comprised of the pneumatic subsystem; the electric subsystem; and the mechanical subsystem consisting of the coupling, force/torque transmission, the frame, bearings, and output link. The mechanical and electrical subsystems are fairly standard and well understood; they are discussed in Chapters 3 and 4. One of the advantages of the inclusion of the electrical system was the relatively simple modelling and fast response. The pneumatic system on the other hand, was comprised of a variety of components such as the valves and the cylinders themselves which respond nonlinearly and much more slowly than the electrical systems. The pneumatic system also provides the majority of the torque capacity, which means that the pneumatic system dominates the overall system response. To improve the control of the pneumatic components, and thus of the overall system, extra effort was applied to the pneumatic component modelling. A large body of research addresses the modeling of a variety of pneumatic actuator and valve configurations. The most relevant publications are reviewed in this section.

The most common types of valves used in the literature are solenoid on/off valves and servo proportional valves. One of the design selections for the GEN2 system was, like the GEN1, to control the pneumatic cylinders using solenoid on/off valves as opposed to proportional valves. Proportional valves allow for a continuous variation between 0-100% of opening. On/off valves are only capable of binary state selection, i.e., either open or closed. As such, on/off valves made cylinder pressure more difficult to accurately control, but are much less expensive than proportional valves. If similar system performance can be achieved through

more complex control (implemented through software) using the solenoid valves, they are preferable to proportional valve(s).

Shearer(1956), represents the basis for a majority of the subsequent publications which model pneumatic systems involving a pneumatic cylinder controlled with some sort of valve. Shearer developed a model of a double acting pneumatic cylinder by a combination of the ideal gas law, conservation of mass, and the energy equation. It was assumed that air acts as an ideal gas, the chambers have homogeneous temperatures and pressures, and the kinetic/potential energies of the gas particles were negligible. Variants of these equations with the same assumptions form the basis of much of the modelling in the work that followed this publication. Typically, isothermal or adiabatic assumptions have been made to further simplify the relationship.

Mills (1990), who used proportional valves to control the PAM, used a simplified model of the valve dynamics as presented by Van de Vegte (1986). The rate of pressure change was modelled by a sum of the current chamber pressure multiplied by a valve specific time constant and the control signal sent to the valve multiplied by the time constant and a proportional gain. The relatively simple empirical relationship was sufficient for his application.

In 2000, Richer & Hurmuzlu presented a two part paper addressing 1: the nonlinear model (Richer & Hurmuzlu, 2000a), and 2: the nonlinear force control (Richer & Hurmuzlu, 2000b) of a pneumatic cylinder. The work focused on modeling a double acting, low friction, pneumatic cylinder controlled with proportional valves. Their model accounted for the effects of air compressibility, inter-chamber leakage, dead volume, time delay due to supply line lengths, charging/discharging thermodynamics, valve dynamics and cylinder seal friction. Mass flow rate was mathematically related to the current chamber pressures and piston velocity. The chamber model was based upon the same equation as presented in (Shearer, 1956), although an adiabatic assumption was made for

chamber charging and an isothermal one for chamber discharging. The tube connecting the chamber was modeled to consider the pressure drop, and thus steady state flow rate drop, as well as the time delay seen in the pressure wave between the valve and chambers. A simplified model (as opposed to infinite series solutions) was used due to the computation time concerns for an online controller. Due to the relatively short length of tubing used, the solution was simplified to a one dimensional wave partial differential equation, which was solved with appropriate boundary conditions, depending on the current/prior valve state. A mass flow relationship was the result, with the determination that the time delay for the pressure wave to travel through being related to the length of the tube divided by the speed of sound. The valve was modelled for the specific proportional spool valve used, where the mass flow rate was based upon the mass flow through an orifice equation as derived from those presented in Shearer(1956). Friction was modeled as a sum of Coulomb, static, and dynamic values. The mathematical model was simulated and practically compared against several configurations of cylinder and tube length. Very good results were achieved between the simulated mathematical model, and the observed performance, in terms of both pressure and position tracking. For sine position testing, amplitudes were well matched. From the example plot shown, maximum error was ~1.5 mm (~4%) and less than 1 ms of time shift was seen.

Ahn & Yokota (2005) focused on the behaviour of solenoid on/off valves under a novel modified pulse width modulation (MPWM) scheme in an effort to improve upon standard pulse width modulation (PWM). A rodless, double acting cylinder was used, with four 2-way solenoid valves connected to each chamber. Pairs of valves were connected in parallel to provide a larger maximum mass flow rate. The dynamics and response of the overall system was studied to produce a modified model. The specific dynamics of the valves were not modelled from a physical basis. Traditional PWM dictates the valve open time percentage be proportional to the control signal. The MPWM controller presented accounts for

the nonlinear elements of the valve dynamics, by experimentally determining the dead time, and rise time to open fully. A learning vector quantization neural network was also used to estimate and categorize the magnitude of unknown payloads.

Ning & Bone (2005) presented the development of a nonlinear model which included cylinder dynamics, payload motion, friction, and proportional valve dynamics. The authors pointed out that the valve and cylinder equations of Shearer (1956), McCloy & Martin (1980), and models based upon these publications were often cited and used, but not often verified for specific hardware. Ning & Bone created an alternate valve equation based on observations of the specific proportional valve they investigated. Further they encouraged future researchers to carefully consider the valve model used, and to experimentally characterize them. Model parameters were identified using simple open-loop experiments and curve fitting. The new model fit proved best when the valve/chamber was filling or discharging at its maximum rate, and was slightly worse at lower flow rates. Despite this variation, the quality of the fit was much higher than the Shearer (1956) model. For example, the Shearer model had ~25% error in mass flow rate estimate compared to a measured value at one operating point. For the same point Ning & Bone(2005) had only ~2.1% error.

Shen *et al.*, (2006) discussed the PWM-based control of a double acting single rod pneumatic cylinder controlled with two 3-way solenoid valves. The PWM duty cycle was selected using a sliding mode controller. Due to the discrete nature of solenoid valves/PWM an "averaged model" of the overall cylinder+valves pneumatic system was developed. This model was a time averaged combination of the available modes the system could be in, for the fractions in which they were in each mode. Where a mode referred to the different combinations of the two valve states (open or closed). The pneumatic cylinders were modelled with Shearer's (1956) equation to determine the mass flow rate given the system valve state. A system acceleration model considering

the mass, velocity dependant loading, chamber pressures and cross-sectional areas was described. Only three modes were considered useful and unique. Within a single PWM period the valves could only be in these modes, with each mode occupying a specific fraction of the period. The mode fractions of time then became the duty cycle, where the sum of the fractions of each mode must be equal to the full duty cycle. The mode selection then became a function of a single continuous input, the duty cycle. Thus overall time continuous model was, for each PWM period, the sum of the effects of each mode selected multiplied by their time fraction of the period.

Rao & Bone (2008) modelled proportional 2-way valves as part of their model-based controller development. Experimental data was first collected for each of the individual valves used. Steps throughout the control signal range were input and system pressure was measured and mass flow rate was estimated. A second order bipolynomial surface was fit to the data such that mass flow rate was a function of chamber pressure and control signal. The quality of fit was evaluated by comparing the result to the proportional valve model of Bobrow & McDonell (1998). Evaluated across four individual valves, the bipolynomial had 43% less root mean squared error (RMSE) between the model and experimental data than that of Bobrow & McDonell. Rao & Bone also found the filling portion of the valve flow was more difficult to accurately model than the discharging.

Bone & Chen (2012) described the GEN1 HPEA. It used two 3-way solenoid on/off valves, one per chamber. The charging and discharging mass flow rates were modelled by piecewise equations. The mass flow through the valves had two regimes: choked flow and unchoked flow. When the ratio of downstream over upstream pressures was less than a certain value the mass flow rate becomes choked and was constant for a constant supply pressure. Above this pressure ratio the mass flow rate was variable. The mass flow rate equation developed was a function of the upstream and downstream pressures,

as well as a valve specific constant. The relationship was empirically developed to fit to observed mass flow data. The cylinder pressure model for the cylinders was based upon those presented by Shearer (1956). The model of friction incorporated either a sum of Coulomb and viscous friction, or simply static friction. The values were experimentally determined for the particular cylinder used. They did not provide any information about the accuracy of their models.

Carneiro & de Almeida (2012a), used an Artificial Neural Network (ANN) approach to model the nonlinear nature of the pneumatic components. A double acting pneumatic cylinder with two proportional valves was studied. Three separate ANNs were developed and used. The first, an inverse ANN model, was used for the valves, which given mass flow rate desired and pressure differential between chambers returned an appropriate PWM frequency input for the valves. The second, a direct ANN model, returned a mass flow rate given the valve PWM frequencies, and instantaneous chamber pressure differential. The third, a 2nd direct ANN model, estimated the friction force given the current velocity and acceleration estimates of the system. The ANNs were black box models trained using experimental data to approximate a relationship (three dimensional surfaces in these cases) between the input/output variables. The ANNs had the advantage of not requiring a detailed mathematical model based on the physics of the system, while still capturing the nonlinearities and complexities of the pneumatic systems. The difficulty in the ANNs lie in gathering appropriate data, selecting proper network configuration, and solving the optimization problem required to tune the network. The friction model developed had a fitting error of 1.9% of the maximum range of friction values. The inverse and direct models were previously presented in Carneiro & de Almeida (2006). The direct model had a maximum error in fit of 1.25% when compared to the mass flow rate used for training. When the inverse model was used to control the valve, a maximum 1.3% mass flow error was achieved.

Hodgson *et al.* (2015) presented a nonlinear discontinuous averaging model for use with a PWM based sliding mode controller. A double acting, double rod pneumatic cylinder was controlled with four 3-way solenoid valves. Similarly to Shen *et al.* (2006), the discrete valve state combinations were analyzed. With the increased number of valves nine useful modes existed in the system. Only seven modes were retained for consideration, as two produce a similar effect, although less effectively than the other modes. The overall system acceleration model was written in terms of each mode. As in Shen *et al.* (2006), the PWM duty cycle became the continuous input for the averaged continuous model. Where the output over the period was the sum of the effects of each mode multiplied by their portion of the PWM period. With further restrictions and by selecting the most effective modes, a three mode, a five mode, and a seven mode model were also developed and compared. All three were capable of controlling the system with the modes they contained. More modes allowed for more flexibility in the ways and to the degree the system can be affected. The selection of which modes to use depended on the desired duty cycle and the model (3, 5, or 7) used. For each model using several piecewise linear mappings which were a function of the control action desired (pressurizing, venting, or closed) via duty cycle as well as predetermined transition points between the possible modes. The transition points were selected to reduce the valve switching requirements. The mapping arranged the modes such that only two could be active per duty cycle, as by PWM's nature, only one valve switch (and thus mode change) can occur per PWM period.

2.4 Position Control

Van Varseveld & Bone (1997) controlled a double acting pneumatic cylinder using two 3-way solenoid on/off valves, one per chamber. The actuator moved an inertial load in the horizontal plane. A novel PWM scheme was used to

control the valves and a proportional plus integral plus derivative (PID) plus friction compensation controller and position feedforward was used to control position. Standard PWM was modified by accounting for the valve delays (when turning on and off) and linearizing the nonlinear valve response. The overall control signal to valve PWM duty cycle become a three segment piecewise linear relationship. The two duty cycles were simultaneously solved based on the overall control signal. This led to a much more linear response in the piston velocity vs overall control signal than with standard PWM. Experimental tests were performed with a 0.94 kg payload and a maximum 0.21 mm steady state error was achieved with steps up to 64 mm. RMSE tracking error of less than 2 mm was achieved for an S-curve profile consisting of a ramp with polynomial blends at the start and finish. Robustness was tested by introducing unknown mass to the system, for which stability was maintained up to a 600% increase in payload mass.

Takemura *et al*. (2000) presented the control of the HPEA described in section 2.2. A 1.5 kg payload was position controlled in the horizontal plane. A sliding mode controller was used for trajectory tracking. In lieu of using the acceleration as a state variable in the controller, due to large noise levels, the pressure differential was used. A 200° peak-to-peak (PTP) amplitude sine wave at a frequency of 0.5Hz. was tracked. The maximum absolute error was ~17.5° (8.8%) in purely pneumatic operation, and improved to ~9° (4.5%) in hybrid operation, for the example experiment shown. Using the hybrid system vs. just the pneumatic motor, faster response times and smaller errors were observed in step tests, as was predicted.

Ahn & Yokota (2005) controlled a rodless, double acting cylinder with four 2-way solenoid valves connected to each chambers. Pairs of valves were connected in parallel to provide a larger maximum mass flow rate. A state controller using a MPWM scheme was used. State feedback of position, velocity and acceleration were used for the position tracking portion of control. A payload

estimation scheme was included, and 10 kg, 20 kg and 30 kg payloads were evaluated. The MPWM was compared to an standard PWM (without the dead time/opening time consideration) scheme in a position step move of ~525 mm. Using the MPWM led to a slight increase in the overshoot (PWM=0%,MPWM=0.2%), but a significant reduction in steady state error (SSE) from 3.3% to 0.04%.

Shen *et al.* (2006) discussed the PWM-based control of a double acting single rod pneumatic cylinder controlled with two 3-way solenoid valves. Again the PWM duty cycle was selected using a sliding mode controller with three available modes. The state vector contained position, velocity, acceleration, and each of the chamber pressures. The system was operated in the horizontal plane, with a 10 kg payload mass acting as the inertial load. The PTP amplitude was 40 mm over 0.25, 0.5 and 1 Hz frequencies. Maximum absolute errors (MAE)s of ~2 mm, ~3 mm, and ~4 mm were observed at the three frequencies respectively, for the example experiments shown.

Nguyen *et al.* (2007) addressed the control of a double acting, rodless cylinder using four 3-way solenoid valves. Instead of PWM, a simplified sliding mode controller was used to directly switch the valves. Four solenoid valves were used but with only three modes. These modes were directly controlling the valve state, as opposed to a PWM mode system as in Shen *et al.* (2006). Particular attention was paid to reducing the number of valve switches required in an effort to reduce power usage and extend the operating life of the valve. A second order sliding surface was used, and the controller was shown to be bounded input bounded output (BIBO) stable. To reduce valve switching an error deadband was used, such that the control signal was set to zero if the absolute value of error was under a certain acceptable threshold. Experimental testing, with a 2 kg payload mass moving in the horizontal plane, of a 40 mm PTP sine test at 0.5 Hz resulted in ~2 mm MAE. For 40 mm step testing the controller achieved 0.1 mm SSE.

Rao & Bone (2008) controlled a small double acting, single rod pneumatic cylinder with two proportional 2-way valves. A nonlinear multiple input single output control law was developed. The state variables were: position, velocity, chamber *A* pressure, chamber *B* pressure, mass flow rate through valve *A*, and mass flow rate through valve *B*. The controller was proven to be BIBO stable. Experimental tests were performed in the horizontal plane with a 1.5 kg payload. An S-curve trajectory was followed for a 20 mm move over 1 second, with an MAE of ~0.3 mm and an RMSE of 0.074 mm, for the example shown. Sine testing was also performed with a 35 mm PTP amplitude at 1 Hz, where a 0.5 mm MAE and a 0.136 mm RMSE were observed.

Shin *et al.* (2009) developed a PID based controller for their HPEA, with the gains experimentally tuned. The PAMs were approximated by a first order model. An adaptive PID controller was used to provide closed loop feedback. Their controller divided the torque between the pneumatic and electric actuators by first requesting the full torque from the pneumatic, and assigning the torque error between the pneumatic and desired to the electric. Testing was performed in the vertical plane with a 6 Hz, 10° PTP amplitude sine desired trajectory. The inertia was negligible since the output link was made from hollow plastic and no payload mass was used. Purely pneumatic MAE was <1°, which was improved to <0.25° in the hybrid mode.

Hodgson *et al.* (2012) controlled a double acting, single rod pneumatic cylinder using four 2-way solenoid valves. Again, a sliding mode controller was used. Similar to Nguyen *et al.* (2007), their controller directly switched the valves states instead of using PWM. Seven modes were used as opposed to the 3 used by Nguyen *et al.* (2007).The state variables used were: position, velocity, acceleration, and each of the chamber pressures. The system was proven to be BIBO stable. The system was experimentally tested in the horizontal plane with a base 0.9 kg inertial payload, as well as a constant external gravitational load provided by a payload mass and pulley. Gravitational payloads of 0 N, 4.9 N, and

9.8 N were used with a 0.5 Hz 40 mm PTP sine wave. The RMSEs achieved for these loading conditions were ~0.5 mm, ~0.6mm, and ~0.75mm, respectively.

Carneiro & de Almeida (2012b), presented the trajectory tracking of a double acting single rod pneumatic cylinder controlled with two proportional valves. The system was modelled using ANNs as discussed in Carneiro & de Almeida (2012a). A PID controller was initially designed using the Ziegler Nichols method, and further tuned empirically. A state feedback controller was also developed using a third order linearized model, and designed using experimentally identified parameters. Experimental testing was performed for both controllers for sine trajectories with a 5.9 kg payload. The state feedback controller yielded the best results. For a 300 mm PTP sine wave at 2 Hz, the MAE was ~6 mm for the example presented.

Bone & Chen (2012) presented a controller for the GEN1 HPEA. A discrete valued model predictive controller (DVMPC) was developed for the pneumatic actuator. The cost function to be minimized was the squared sum of position errors of each timestep of the prediction horizon. Like the controllers of Nguyen *et al.* (2007) and Hodgson *et al.* (2012), DVMPC directly switches the valves instead of employing PWM. Due to the limited number of control states (i.e., four per prediction step) an exhaustive search could be used to solve the optimization problem in the real-time controller, subject to the number of prediction steps. A simple PD controller was used for the electric motor. The desired motor contribution desired was set to the current force error between the desired force and the pneumatic contribution. Experiments were run in the vertical plane, with an equivalent linear payload mass of 17 kg, with cycloidal S-curve trajectories, as well as some sine testing. Purely pneumatic testing of a 75 mm (115°) cycloidal move over 4 s resulted in 1.9 mm of (2.9°,2.5%) MAE, and a SSE of <0.1mm. For hybrid operation these values were reduced to 0.3mm (0.43°,0.37%) and <0.1mm, respectively. For an 80mm PTP sine wave at 1 Hz, a

MAE of 0.9mm was observed. Lastly, the DVMPC method resulted in less valve switches than the PWM-based method would.

Teramae *et al.* (2013), as previously discussed, developed a HPEA acting essentially as a controlled pendulum. An iterative linear quadratic Gaussian controller was used to establish appropriate torque distribution between the actuators, based on their capacity and response speed. The state variables were the rotary position, velocity and torque. Practical experiments were performed in vertical, for a suspended payload in a pendulum like arrangement, where sinusoidal "Swing-trajectories" were controlled for over various frequencies. A 2.5 kg payload was used with a link length of 0.4 m. For the 28.6° PTP sine trajectory at 2 Hz, the MAE observed for the given example trial was ~5.7°(~20%).

Bone, Xue, & Flett (2015) improved upon the work of Bone & Chen (2012). They replaced the solenoid valves with two faster switching solenoid valves. Again a DVMPC controller was used, but with the addition of a payload estimation scheme. The electric motor was controlled with an inverse dynamics controller in which the motor model incorporates PID feedback. The payload estimation was introduced to improve the robustness to unknown payloads or mismatch between the modelled and actual payload. This was especially useful as the DVMPC performance relies on the accuracy of the model used. The estimate of expected inertia was used to calculate expected torque. The expected torque was then compared to the actual torque generated to track the desired trajectory. The inertia estimate was then updated assuming the torque error corrected by the controller was due to payload mismatch. The estimate was smoothed by adding a ratio of the current and past estimate. Again vertical cycloidal experimental results were presented with a 0.432 kg link with a length of 0.43 m. The desired position trajectory was a 47.1 mm (90°) cycloidal trajectory with a 2.3 s duration. A RMSE of 0.34 (0.72%) mm and SSE of 0.12 mm (0.25%) were seen for the purely pneumatic mode. For the case of no inertia mismatch, hybrid operation improves these results to 0.06 mm (0.13%) and 0.02 mm

(0.04%), respectively. The payload estimator was evaluated by introducing a positive 90% inertia mismatch (i.e., actual inertia was 90% larger than model's initial estimate). Without the estimator this resulted in an increase in pneumatic mode RMSE of 1564% and hybrid mode RMSE by 369%, as compared to the no mismatch case. When the estimator was used the robustness was greatly improved. With the 90% mismatch, the RMSE in pneumatic mode increased by 200% and in hybrid mode the increase was 8% compared to the no mismatch results.

Hodgson *et al.*,(2015) also presented the control of a double acting, double rod pneumatic cylinder using four 3-way solenoid valves. The valves were controlled using PWM and a discontinuous dynamics averaging scheme, as previously discussed. The closed-loop control was provided by a sliding mode controller. Three, five, and seven mode schemes were investigated. An integral sliding surface was presented and the BIBO stability was proven. The three mode and seven mode controllers were experimentally evaluated. A 0.9 kg payload was controlled in the horizontal plane for step tests of 40 mm. A three mode and a seven mode switching controller (SC) were also compared to the model-based (MB) (sliding mode) results. Several step test magnitudes were investigated. For precision testing 50 trials of a 15 mm step resulted in RMSEs of: SC3 = 0.4 mm (2.4%), SC7 = 0.3 mm (2.0%), MB3 = 0.8 mm (5.4%), MB7 = 0.7 mm (4.4%). The number of valve switches required were: SC3 = 148, SC7 = 57, MB3 = 43, MB7 = 31. Large steps of 70 mm resulted in RMSE values of SC3 = 12.6mm (17.7%), SC7 = 11.9 mm (16.8%), MB3 = 12.0 mm (16.9%), MB7 = 11.8 mm (16.6%). The number of valve switches required were: SC3 = 259, SC7 = 92, MB3 = 42, MB7 = 25. Error values are quite similar for the trials, but the MB7 controller significantly reduces the number of required switches, which would extend valve life. Robustness was also tested by increasing the payload mass by 56% to 1.4 kg and by 111% to 1.9kg. Testing was performed for the three cases with a saw-tooth trajectory of 70 mm over 2 s. For the MC7 controller the RMSE

increased from 1.06 mm (1.49%) for the nominal case to 1.28 mm (1.80%) for the 1.4 kg payload and 1.53 mm (2.16%) for the 1.9kg payload. These were RMSE increases of 21% and 44%, respectively.

Ramhuzaini, He, & Sepehri (2015) presented a dynamical adaptive backstepping sliding mode controller for position tracking. A double acting single rod pneumatic cylinder was controlled in the vertical plane using a proportional valve. The state variables were position, velocity, acceleration, and the chamber pressures. The dynamical adaptive backstepping controller also included a LuGre model-based friction compensator. A variety of configurations, trajectories and payload masses were evaluated experimentally. For the nominal case a 9 kg payload was used for a 200 mm PTP sine trajectory at 0.1 Hz. This resulted in ~5 mm MAE and 1.94 mm RMSE. If the payload mismatch was ~50% (i.e., actual payload was 4.4kg), the errors actually decrease to <5 mm MAE and 1.42 mm RMSE. An S-curve trajectory of 10 mm over 2.5 s was also evaluated. An MAE of ~5 mm, an RMSE of 1.1 mm and an SSE 0.53 mm were observed. For the ~50% mismatch the results were an MAE of ~4 mm, RMSE of 0.96 mm and SSE of 0.70 mm.

2.5 Conclusions

Multiple designs and arrangements of hybrid actuators have been developed throughout the prior art. Various types of pneumatic actuators have been used in combination exclusively with electric motors. Due to the relatively limited number of publications in HPEA specifically, several important publications on purely pneumatic actuator modelling and control were studied. In most cases a model based on, or similar to, the model presented by Shearer (1956) was used for the pneumatic components. In some cases black box models such as ANNs were used to empirically model the nonlinear complexities of the subsystems. For position control, sliding mode controllers were commonly

used due to their robustness to modelling errors and system uncertainty. This type of robustness is especially useful due to the simplifications and assumptions typically made when modelling pneumatic systems.

Chapter 3 - System Design

3.1 Introduction

The impetus for the work presented in this thesis was the desire to produce the next generation of HPEA. As such the lessons from the prior art, especially of Chen (2012) and Bone & Chen (2012) were used as a base upon which to build. Particular attention was paid to increasing the torque output of the actuator to make it competitive with the actuators used in industrial robotic arms in terms of payload capacity. This chapter will, in section 3.2, discuss the motivations and capabilities desired for the system. Section 3.3 presents an overview of the GEN2 system. Section 3.4 presents the mechanical design and system capabilities. Section 3.5 describes the design of some specific electrical elements of the system. Section 3.6 presents the final torque capacity of the system. Finally, section 3.7 summarizes the GEN2 system's improved capabilities and concludes the chapter.

3.2 Motivations and Capabilities

The prior actuator (Chen, 2012; Bone & Chen, 2012; Bone, Xue, Flett, 2015), which was used as a basis for improvement had several undesirable properties which were remedied in the current work, though the primary desire was for an increased torque/payload capacity. The prior system is referred to as the generation 1 hybrid actuator (GEN1), where the improved actuator is referred to as the generation 2 hybrid actuator (GEN2). The GEN1 actuator, shown in Figure 3.1 was comprised of several basic components:

- Double acting pneumatic cylinder
    - The primary torque contributing actuator in the system.
- Linear slide with rack gear

  - Provides a mechanical base for the rack gear to be mounted and convert linear force/motion to rotary. This also provided stability for the extended cylinder rod. Furthermore, this could act as a mounting point for a payload if the hybrid was to operate as a linear actuator.
- Output shaft with driven gear
  - Facilitated the combination of the two actuator torques, and allowed for a payload link and mass to be coupled to the actuators.
- Motor with pinion gear
  - Provided the electric torque, using low ratio gearing to couple to output gear. After gearing, at peak torque, the electric system provided ~10% (Bone & Chen, 2012) compared to that of the pneumatic system.
- Base
  - Allowed for horizontal or vertical operation of actuator.
- Pneumatic circuit (valves, accumulator, etc. Not shown in figure)
  - Distributed and controlled the pneumatic cylinder's energy source.

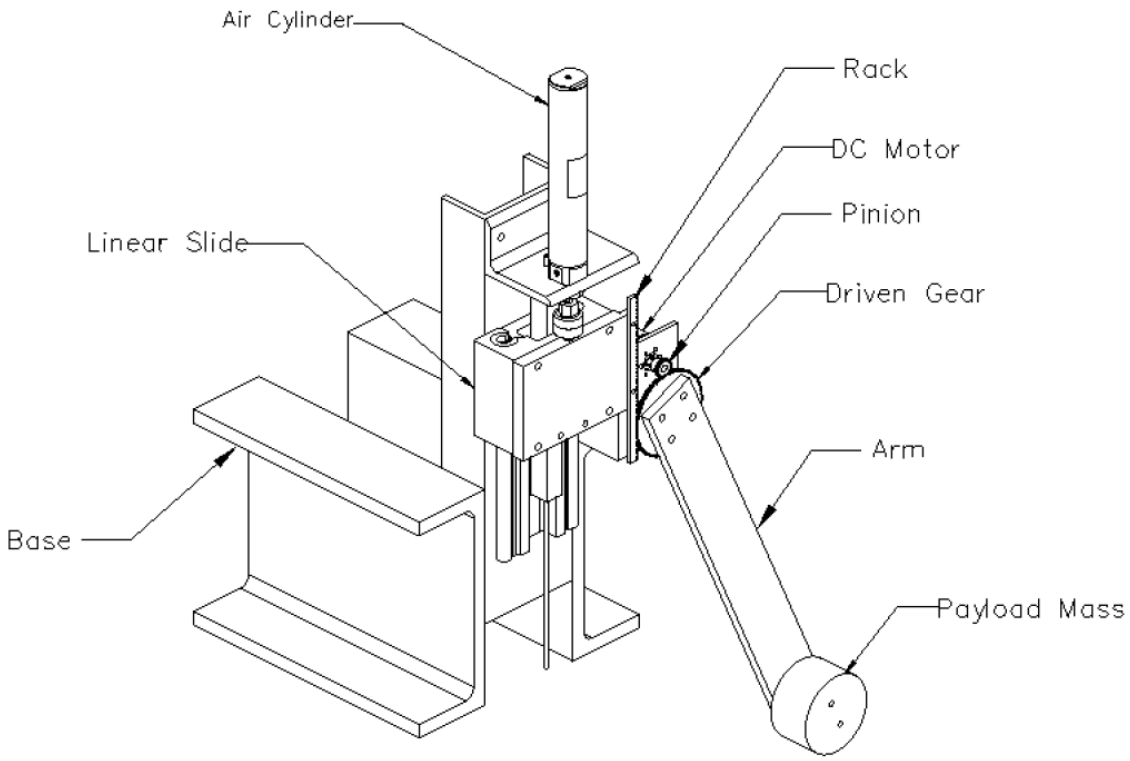

Figure 3.1 GEN1 HPEA assembly drawing, Bone & Chen, (2012).

The maximum torque capacity of the GEN1 actuator was its main limitation, especially in the vertical configuration where gravity introduced a significant load. The linear slide acted as a support and bearing for the pneumatic cylinder and rack gear. The linear slide's mass also acted as a counterweight to partially counterbalance the gravity load of the payload mass. Due to the small size of the rack and motor pinion gears used, they were both difficult to mount properly. The mounting arrangement used made it difficult to avoid either backlash or excessive gear wear due to binding of the teeth.

The main goals for the GEN2 system were: increased torque capacity, low friction/inertia in transmission components, and more reliable/robust mechanical design while maintaining or improving performance. The improved system used more suitable, higher capacity components and a custom mounting for bearing components to negate the need for a large linear slide.

The GEN2 actuator was developed with the intent that it could be used as a component of a six-axis robotic arm of the style commonly used industrially since the advent of the PUMA 560 in 1985. An example of a typical robot arm is shown in Figure 3.2. The hybrid actuator would be most applicable to the highest torque joints, those that actuate the largest loads, due to gravity, namely the shoulder and elbow joints.

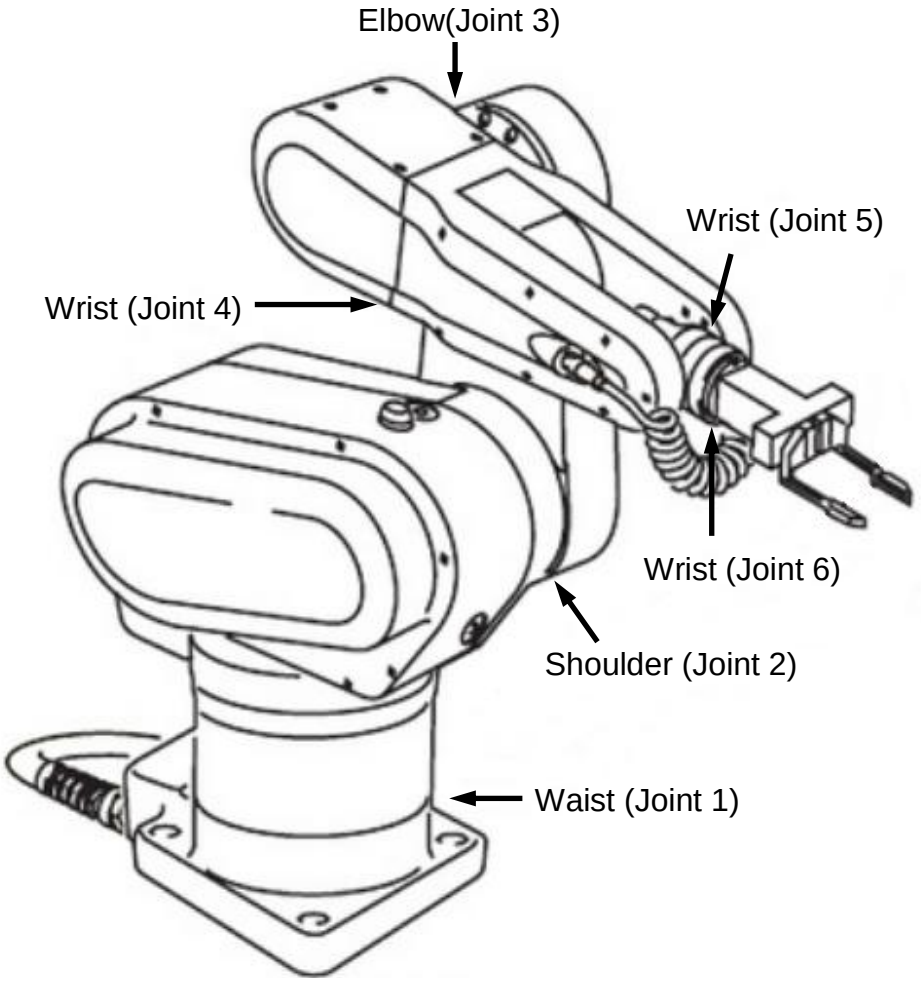

Figure 3.2 Diagram of a CRS F3 robot, a six-axis robot arm of approximately human scale. Adapted from Thermo-CRS (2002).

The actuator was developed keeping in mind the desired application being for robot arms operating in collaborative settings with humans. The comparable purely electric systems currently being commercially sold for collaborative applications are of approximately human scale, in terms of geometric dimension. This is as opposed to larger robot arms, such as those used for automotive body assembly. Those robot arms produce very large torques and carry heavy payloads that make them unsafe for collaborative operation. A survey of some commercially available arms designed for collaborative operation is summarized in Table 3.1. The table lists relevant specifications for the shoulder joint which typically has the most intensive torque requirements of any actuator in the arm, as it needs to move the distal robotic arm components and payload against gravity.

Table 3.1 Summary of some commercially available collaborative, human-scale robots. (Rethink Robotics (2015a), Rethink Robotics (2015b), Universal Robots (2015), Kuka (2015), Kawada Industries (2015)).

Robot	**Joint 2 ROM (°)**	**Max Joint Speed (°/s)**	**Rated Payload (kg)**	**Max. Shoulder Torque (Nm)**
Rethink Robotics Baxter	180	unknown	2.2	50
Universal Robots UR3/UR5/UR10	720/720/720	180/180/120	3/5/10	>14.7/41.7/128*****
KUKA IIWA	240/240	98/85	7/14	176/320
Kawada Industries NEXTAGE	200	130	1.5	unknown

*Calculated assuming robot is at maximum reach, with maximum payload, at highest gravity position. True capacity must be larger to support mass of additional joints and links, but was not available in the literature.

The table gives context as to what a reasonable torque capacity and range of motion should be selected when designing an arm of similar capacity. The current Canadian Standards Association standard for industrial robots, CAN/CSA-Z434-14 (CAN/CSA, (2014)), which is based on the ISO standard 10218-1 (ISO, (2011)), specifically addresses collaborative robotics. The most relevant limitation being that in collaborative operation the robot's tool must be limited to a maximum velocity of 0.25 m/s. Assuming that this actuator would be used as the shoulder joint of a robot arm, with other links fully extended, with 0.25 m/s velocity at the end of the 0.6 m arm, the maximum angular velocity would be 0.42 rad/s or 24 °/s. In non-collaborative operations the robot should be capable of higher velocity operation, and only be software limited for the collaborative operation.

The GEN1 hybrid actuator was designed as an initial investigation into this type of actuator and as such was only designed as a trial of the underlying hybrid concept, and to develop relevant control schemes. It was not designed with the capabilities as mentioned in Table 3.1, because it was not meant to be directly comparable. The relevant specifications of the GEN1 actuator are summarized in Table 3.2. The GEN 2 actuator was designed to extend upon the GEN1 and be of a scale more comparable to that of the commercially available electric robotic actuators used in collaborative robotics. The development of the GEN2 design is discussed in the remainder of this chapter.

Table 3.2 GEN1 System specifications of GEN1 (Chen, 2012)

Specification	**Generation 1 Actuator**
Design Nominal Payload	0.5 kg at 0.5 m
Max. Holding Payload	1.3 kg at 0.5 m
Design Joint Speed	45 deg/s
Joint Range of Motion	180
Arm Length	0.5 m

3.3 System Overview

The design of the GEN2 actuator was done iteratively, with the aforementioned performance goals in mind. A basic design was envisioned, and was refined as the specific subcomponents were designed or selected, and revised where different components affected the design or selection of others.

Since the pneumatics provided force and motion in a linear sense, and the desired output is rotary, this force and motion needed to be converted using mechanical means. A mechanical linkage; pulley with belt or cable; or gearing are common methods to convert linear actuation to rotary. Gearing was selected for the simpler assembly and maintenance required, as compared to other systems. As in GEN1, the simplest arrangement of cylinders and gearing to convert linear to rotary actuation while maintaining backdrivability was the use of rack and pinion gearing. The use of rack and pinion gearing was also a convenient way of coupling the pneumatic actuators and electric actuator to a common output shaft.

The improved actuator was comprised of four double acting pneumatic cylinders operating in parallel with an ungeared electric motor, both connected to a common rotary output shaft. Figures 3.3 and 3.4 show the mechanical drawings of the final GEN2 actuator design, the specifics of which are discussed in the remainder of this chapter. The basic design configuration was of the type similar to Bone & Chen (2012), as opposed to the PAM type, or vane motor type seen in Mills (2000), or Takemura, *et al* (2000) respectfully. Several features are notable to this design, as contrasted to the design of Bone & Chen (2012) shown in Figure 3.1.

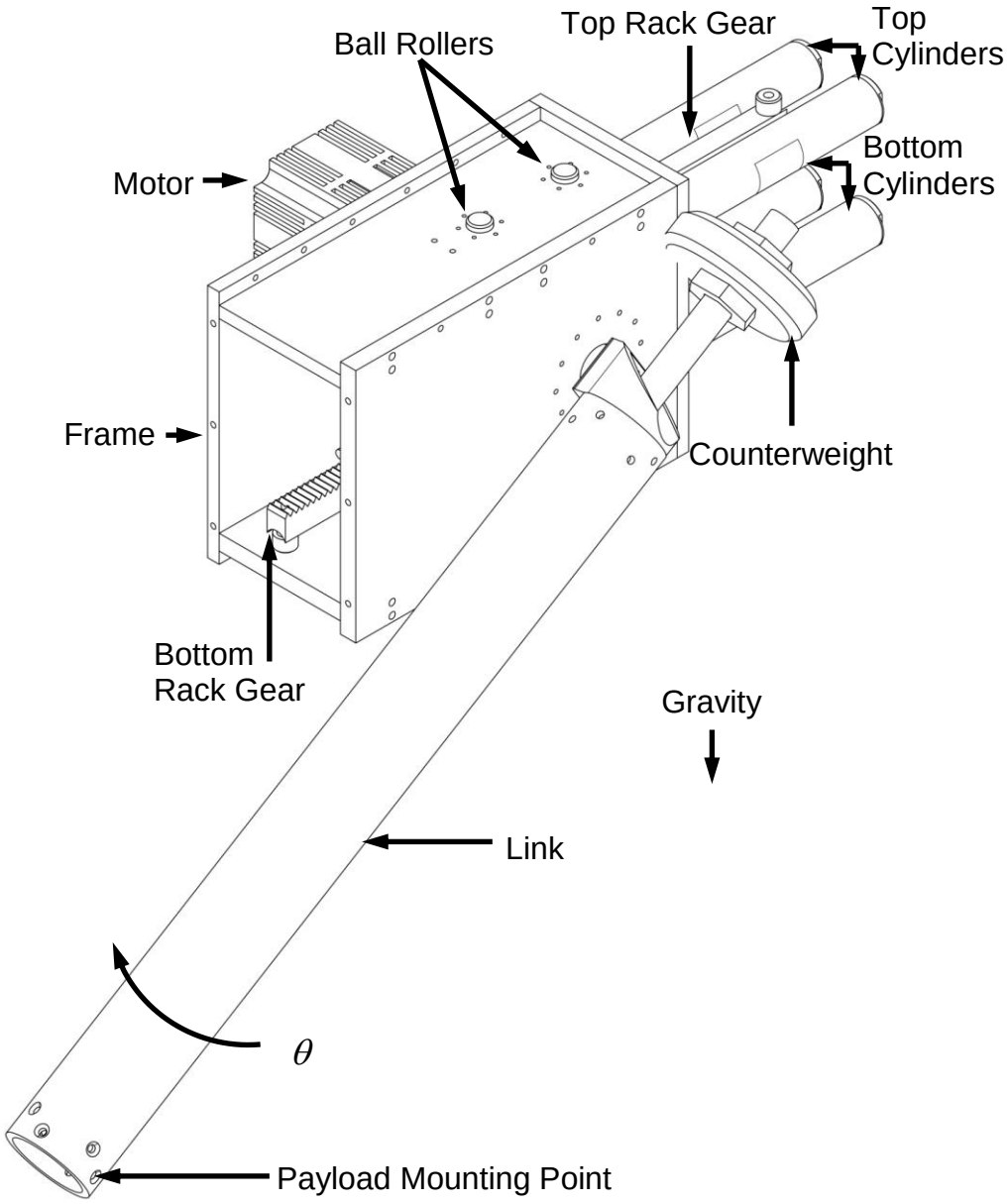

Figure 3.3 Assembly drawing of GEN2 actuator.

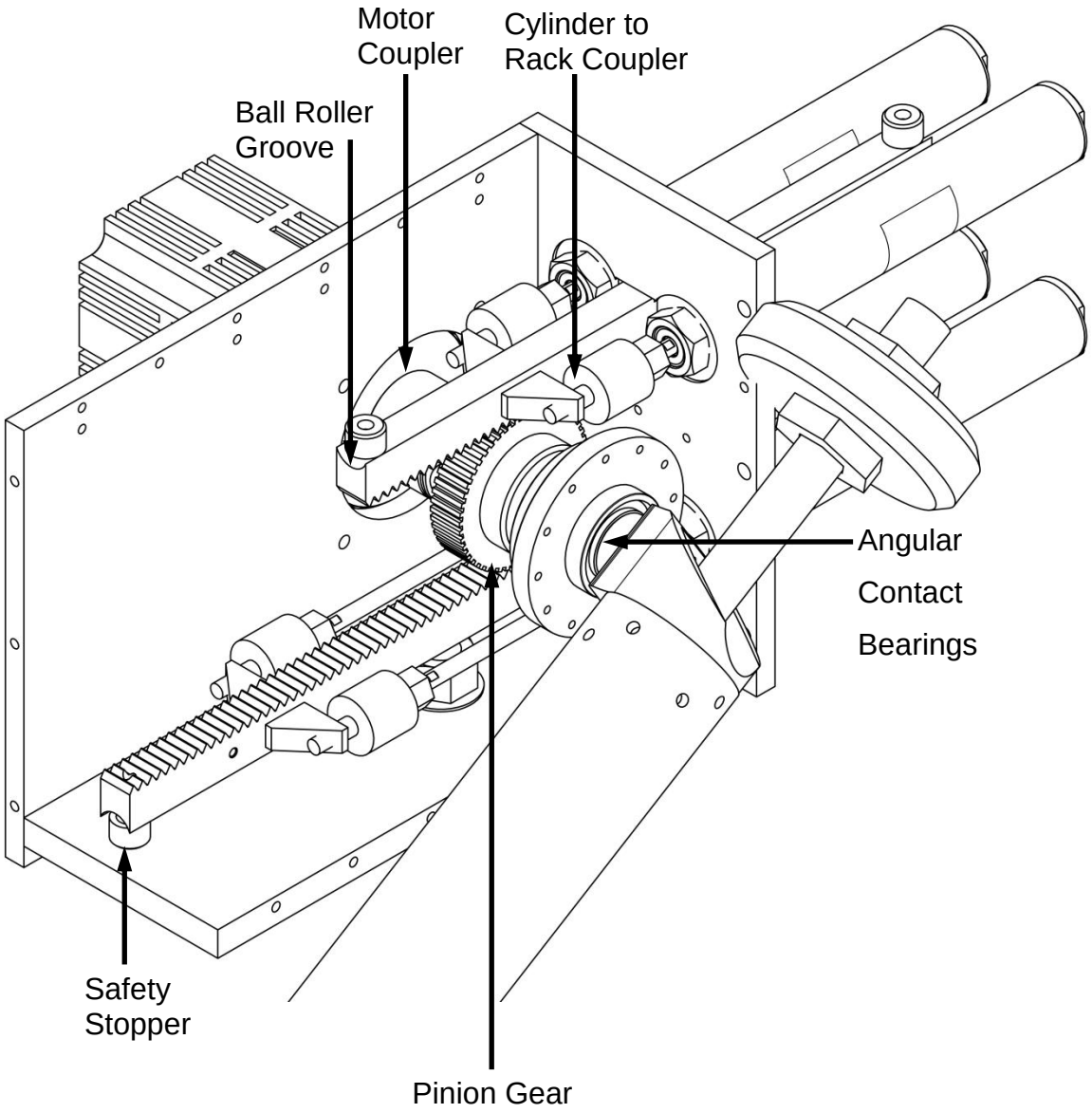

Figure 3.4 Detail view of GEN2 System. Front and top frame components, as well as top gear ball rollers not shown for clarity.

The same type of pneumatic cylinders, as used in the GEN1 actuator were selected due to their low friction properties. The relevant specifications of an individual cylinder are listed in Table 3.3. Since a significantly larger torque was desired, multiple actuators were used. They were arranged on both the top and

bottom of a pinion gear, similar to the antagonistic arrangement commonly used with PAMs, such as in Shin *et al.* (2010). Since the PAM can only apply force in a single direction, the antagonistic arrangement is required to provide force in both angular directions. The double acting cylinder has no such limitation, and allows for cooperative actuation where one side of the gear is "pushed" upon and the other "pulled" upon.

Due to the torque capacity desired, a single top and single bottom cylinder were also insufficient, thus two more were included, in parallel, for a total of four. Using four actuators allowed for one cylinder to be placed on each side (left and right) of each of the two rack gears (top and bottom). This symmetry meant that each rack gear only needed minimal support in its transverse direction. If only a single cylinder was used, the overall system would need to be much longer to allow the rack to be pushed from the center-rear, or the rack would need to support a moment due to the eccentric loading. The "antagonistic-like" arrangement also means that the system could be in future, with minimal modification, accommodate other types of pneumatic actuators such as PAMs. The use of pneumatic cylinders as compared to a rotary pneumatic actuator (as in Takemura *et al.* (2000)) has the advantage of much lower friction. The use of cylinders as compared to PAMs (as in Mills (1990), Shin *et al.* (2010), Song *et al*. (2015)) has the advantage of built in dual action, less stroke limitations, and no force-to-length coupling.

Table 3.3 Pneumatic cylinder specifications.

Specification	Value
Max. Operating Pressure	689.5 kPa (100 PSIG)
Rodless Side Pressure Area	$4.523 \times 10^{-4}\ m^2$
Rod Side Pressure Area	$4.206 \times 10^{-4}\ m^2$
Rodless Side Max. Force	311.8 N
Rod Side Max. Force	290.0 N
Rod Stroke	0.127 m

Four individual double acting cylinders were used in the design, but are pneumatically coupled such that the eight chambers worked together as two chamber groups. Figure 3.5 indicates the nomenclature used to refer to the cylinder and chamber groups. The individual cylinders can be referred to by their respective quadrant of a Top/Bottom-Left/Right arrangement. The only arrangement differences were between the top cylinders and bottom cylinders. The left/right cylinders matched their neighbour, and were effectively just two top/bottom sets in parallel.

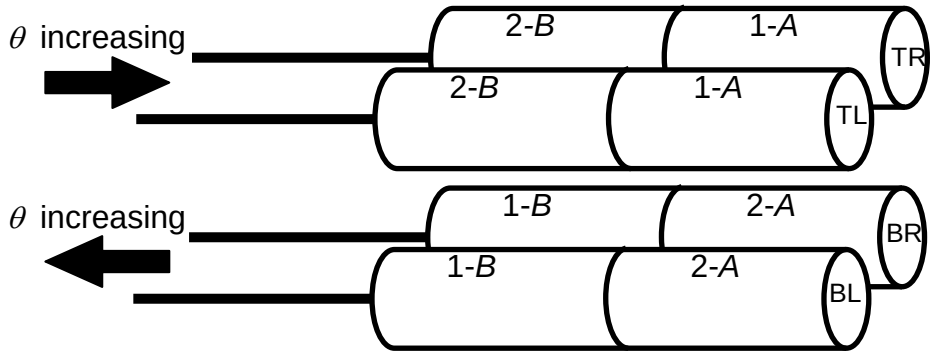

Figure 3.5 Cylinder and chamber grouping. Left and right sets are matched in function. Groups 1 & 2 imparted torque in opposing directions. *A* chambers were the non-rod side chambers. *B* chambers were rod side chambers

The top/bottom cylinders applied force on opposite sides of the rack gear to impart torque/angular motion on the output shaft. As the top cylinders retract, the bottom cylinders extend and vice-versa. The chambers of any cylinder were either chamber *A* or *B*. Chamber *A* is the non-rod side, which has slightly larger pressure area, and does not leak to the atmosphere, only across the inter-chamber piston seal. Chamber *B* is the rod side chamber, with a slightly smaller pressure area, and leakage across both the piston and rod seals. The groups 1 and 2 are used to refer to the total collection of chambers across top, bottom, left, and right, which are provided with the same pressure and act to impart torque in the same direction. Group 1 is comprised of the top two *A* chambers, and the bottom two *B* chambers. The remaining chambers belong to group 2.

The equivalent effective area could have been produced using a single, larger, double acting cylinder, instead of four. The four cylinder arrangement was chosen for the purposes of the mechanical design, and cylinder availability. The arrangement used had an advantage over a single cylinder arrangement in terms of loading symmetry. First, if a single cylinder was used the maximum force in extension would be larger than in contraction due to the cylinder rod occupying area on the piston. In the top/bottom arrangement each collected group was comprised of the same number of *A* and *B* chamber sides, meaning that the force capacity was symmetric. Secondly, the normal (to gear transmission direction) loads due to gear meshing, and the pre-loading of the rack supports were symmetric, meaning that the rotary bearing did not need to support their loads. Figure 3.7, in the bearing selection 3.4.2, illustrates the force balance seen in this arrangement. In a single rack arrangement the bearing would support the normal load of the gear meshing, as well as the preload which ensured the gears remained meshed.

The electric motor selected was arranged such that it could be directly coupled to the output shaft, with no change in mechanical advantage. This allowed for the torque to be directly applied to the output shaft, with no change in

the motor's contributing inertia. Directly coupling the motor also simplified the mechanical design, and did introduce the added issues associated with extra gears, belts or chains, which include: backlash, extra friction, inertia, and maintenance. This arrangement also allows for easy modification of the system in the future, as the motor could be easily taken out and replaced with another.

3.4 Mechanical Design

After the pneumatic cylinders were selected, and their general arrangement chosen, the coupling between the linear pneumatic system and the radial output arm was considered. A common output shaft, supported by bearings was used to connect the rotary electric motor, convert the linear pneumatic force to radial, and connect to the output link which introduces the payload.

3.4.1 Gear Selection

The primary consideration when selecting the gear radius was the trade-off between input-force-to-output-torque and rotary range of motion. The pinion size was selected by considering: commercially available gearing; gear strength; relation between pinion radius and force-to-torque conversion, as well as cylinder stroke-to-rotary range of motion. With the pinion gear radius, number of teeth, and tooth face width selected, the appropriate matching rack was selected. One of the limitations of pneumatic cylinders, as compared to rotary electric or pneumatic motors, is that they have a maximum range of motion where motors typically do not. Yet in practice, the joints in a robot arm have limited ranges of motion (see Table 3.1), even in the electric case. This limitation is due the inevitability of self collision of the arm and/or the requirement for wiring to travel through the arm, and having limited available slack.

As indicated in Figure 3.6, with a linear increase in pinion radius, the torque output capacity increases proportionally, and the range of motion decreases inverse proportionally. The intersection of these two curves is not the ideal solution, as there is not an explicit one to one trade-off between the two variables. Instead a minimum range of motion was selected, and provided that the torque was reasonable, and the next closest commercially available gear was selected.

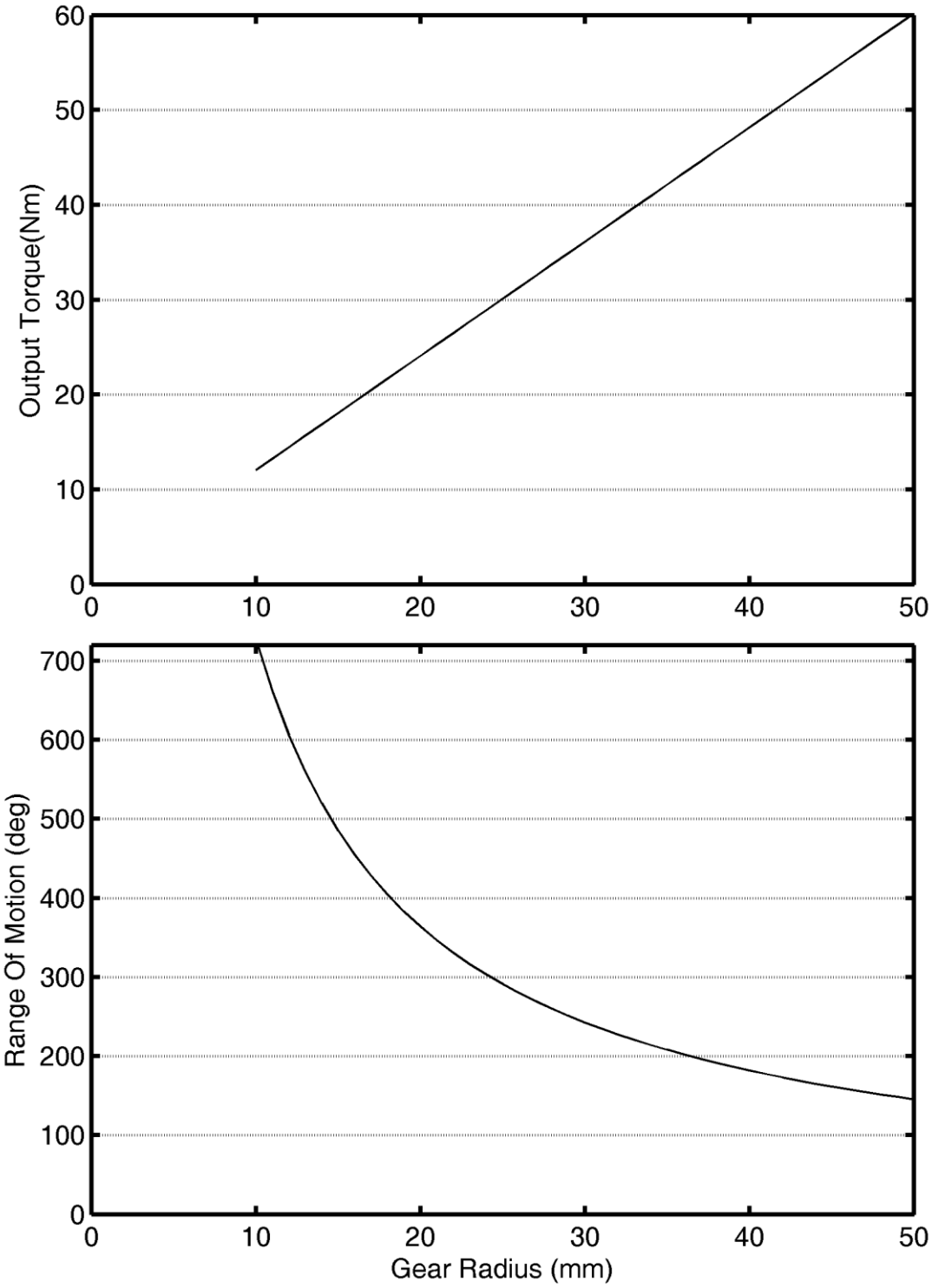

Figure 3.6 Torque capacity to range of motion trade-off for rack and pinion gearing.

A range of at least 180 functional degrees was desirable for a prototype actuator, as it allows for the full range of loading for the arm. It was practically beneficial to have a larger physical range than the desired operating range so that a buffer existed on either side of the operating range. This allowed for limit switches and rubber stoppers to be installed to ensure that the cylinders were not damaged from the piston impacting a cylinder end. If a larger range of motion was desired, longer alternate or custom cylinders could be used with the same rack gear. From Figure 3.6, a gear of less than 40 mm in radius is desired, based on the 180°+buffer goal.

The final consideration was the strength and availability of gears. A gear must exist which is of approximately the desired radius, but also be wide enough, and of a material strong enough to withstand the tooth loading conditions expected. Considering the desired operating range, and torque capacity using four cylinders arranged in two pairs of two, a variety of commercially available gears were investigated. Ultimately a suitable set of matched rack and pinion gearing were selected, as summarized in Table 3.4.

Table 3.4 Rack and pinion gear specifications

Specification	**Pinion Gear**	**Rack Gear**
Pitch Radius	0.0315 m	-
Gear Length	-	0.297 m
Gear Module	1.5	1.5
Tooth Face Width	0.015 m	0.015 m
Rated Load (JGMA 401-01 standard) Factor of Safety: 1.2	51.4 Nm	51.4 Nm
Pressure Angle	20°	20°

The radius of the selected gear provided a 231° range of motion at maximum, and would allow the cylinders to provide a 37.9 Nm maximum continuous torque (at a supply pressure of 100 psia (689.5 kPa)), if four cylinders are used in two parallel pairs. This torque capacity was suitable for supporting a variety of payloads depending on the arm length. At 0.6 m (the link length used) a 6.9 kg mass could be supported in the worst case gravity loading. A smaller mass could be supported and accelerated allowing for reasonable tracking control. If in the future larger mass was desired, the arm length could be reduced.

3.4.2 Bearing Selection

Two bearing systems were required for the system: one set for the rotary shaft components, and a second for the linear cylinders and racks. The rotary bearings were selected to act as the main support system. The supports for the racks and cylinders were selected to support the mass of the racks, so as not to load the cylinder pistons. As the pistons are not designed to support a load in non-longitudinal directions, the constant mass of the gears would lead to leakage and possibly permanent damage.

The linear bearing solution was a particular concern and required some more creative mechanical design than the fairly standard radial bearings. One of the major advantages of the hybrid actuator is the low inertia of the pneumatic actuator; it is desirable to maintain this low inertia through the support/gearing system for said actuators. The GEN1 actuator (see Figure 3.1) used a linear slide to support the cylinder rod and gearing, which had a significant mass and thus inertia. For the GEN2 system a functional low inertia, low friction support system was conceived to take advantage of the four cylinder arrangement, as can be seen partially in Figure 3.3/3.4. Figure 3.7 shows the rack and pinion gears, as well as the ball rollers schematically.

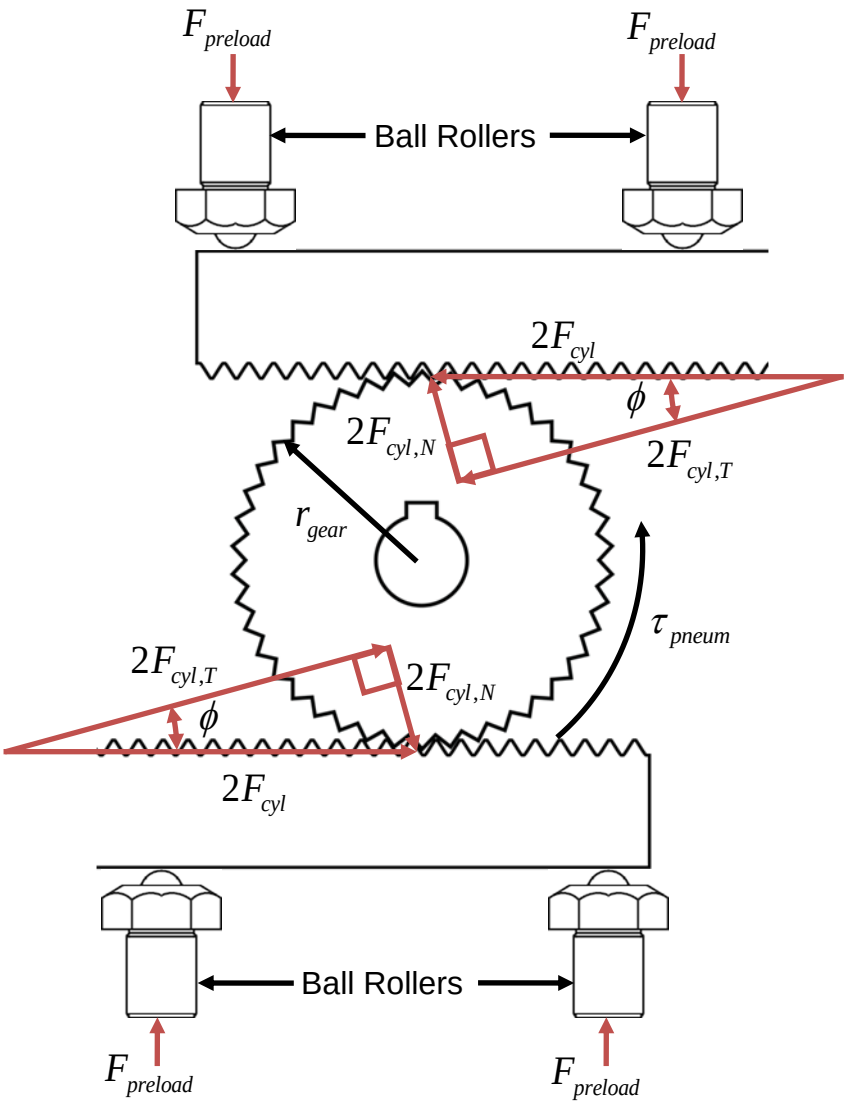

Figure 3.7 Schematic of gear loading and ball roller arrangement. Note that the rack gear groove is not shown for clarity. Only the external forces and their components are shown for clarity as the net load on the gear (save for the torque) and thus shaft/bearing reaction force is zero.

Rather than using a conventional linear bearing the design used several encapsulated ball rollers. An example of a ball roller partial cross section is shown in Figure 3.8. Each rack gear was machined down along its (non-tooth) length with a groove of depth and radius to match the encapsulated ball roller.

The grooves in combination with the gear meshing kept the rack gears aligned with the pneumatic cylinder rods. Two rollers per gear were arranged, as in Figure 3.7 to form a 3 point contact system, with a ball roller on either side (in the rack stroke direction) of the pinion gear. This ensured stable contact and support was maintained. The ball rollers were forced into the back of the rack gears by preloading a compliant material. The preload force on the rollers and rack was adjustable using external screws. This ensured that the rack and pinion gear contact is maintained, as well as supporting the rack gear masses against gravity. This method introduced minimal inertia to the system as no additional moving mass is added to the gears or coupled to the output shaft/link. Furthermore, this arrangement and the compliant preload allowed the gears some flexibility of movement which allowed for self-alignment, and prevents increased friction due to binding of the gears or pneumatic cylinders. This binding could occur if a more rigid linear slide was used and not perfectly aligned parallel to the pneumatic cylinder and pinion gear. The ball rollers were selected to support the worst case load: the relatively minor preload force, gravitational load of the rack gears, and the component of the force transverse to the gear transmission, due to the pressure angle of the gearing. For a single rack gear set, each ball roller must support:

$$F_{roller} = F_{prelaod} + \frac{F_{g,gear} + 2F_{N,cyl}}{2} \tag{3.1}$$

$$F_{roller} = F_{preload} + \frac{\left(gm_{gear}\right) + \left(2F_{cyl}\cos(\phi)\sin(\phi)\right)}{2} \tag{3.2}$$

where $F_{preload}$ =~10N is the preload on the ball roller to ensure the rack gears to maintain contact with the pinion; $F_{g,gear}$ is the gravitational load of the gear, the product of the gravitational constant, g =9.81 m/s^2 and the gear mass, m_{gear} =0.63 kg; $F_{N,cyl}$ is the force of each cylinder normal to the gear; F_{cyl} =312 N is the

maximum force output by each cylinder; ϕ =20° is the gear pressure angle. Thus, F_{roller} =113 N Is the worst case load on each roller. The ball rollers selected each are rated for 343 N. This rating is more than sufficient with a significant factor of safety. These rollers were selected as opposed to smaller capacity rollers, due to their diameter providing a good groove based on the rack gear width.

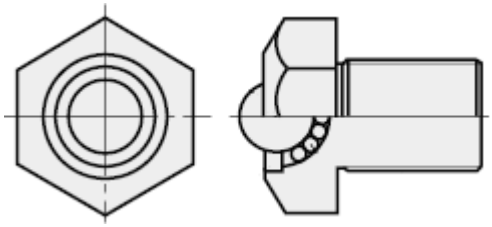

Figure 3.8 Schematic diagram of a ball roller (Misumi USA, 2015). Note the encapsulated ball bearings in the lower, cutaway half of the figure.

For the radial bearings a more complex loading case had to be analyzed. The schematic of the output shaft loading is shown in Figure 3.9. The shaft was supported at two points, **B** and **D**. Point **B** is where the center of the pinion gear was. Any loading perpendicular to the shaft would be partially supported as the load would be transmitted through the pinion gear, through the rack gears and onto the ball rollers. Point **D** is the main shaft support, two back to back mounted angular contract bearings. These bearings support the moment, thrust and normal loads on the shaft. The loads on the shaft at the various points were as follows: **A** where the motor transmits torque; **B** where the pneumatic cylinder torque is transmitted through a shaft key in the pinion gear; **F** where the gravitational load of the arm either in vertical (normal to shaft) or horizontal (longitudinal to shaft) was applied as well as the torque load due to gravity and the inertia of the payload.

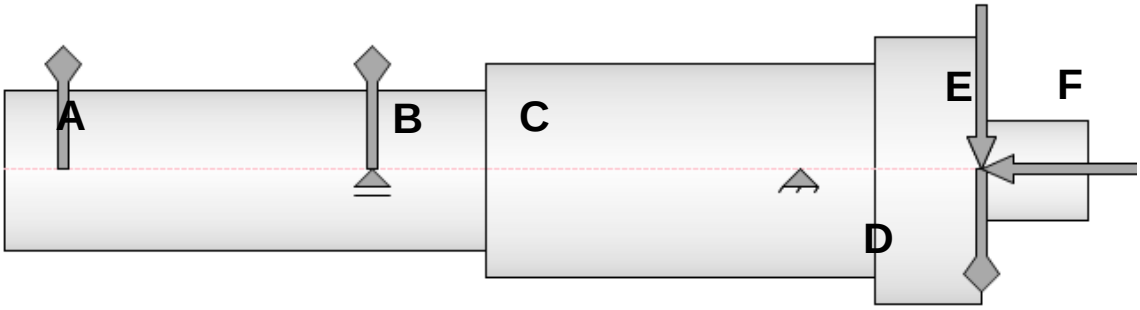

Figure 3.9 Schematic of shaft loading conditions. The arrows indicate applied forces and the diamond symbols indicate applied torques.

The main considerations for the selection of the bearings were to support the radial load caused by the maximum payload, as well as support the moment created by said payload. Loads introduced by the preloading of the ball rollers as well as the normal force component of the gear meshing, equate to close to a net zero value, due to the symmetric arrangement (see Figure 3.7). To be conservative, the bearing was selected so that they could support these additional transverse loads (*i.e.* no balance of forces between the cylinder groups), in the case of pressure loss in one chamber group, or any other mechanical failure or misalignment which might imbalance these loads. The four cylinder arrangement did not provide exactly symmetric loading on the bearings, due to the difference in force direction in the top/bottom cylinder and the effect of the rod area. For example, if one chamber group was at maximum pressure (5 Bar) and the other was at atmospheric pressure (1 Bar), the force difference between the top and bottom groups would be 38 N, 5.4% of the sum total (699 N) produced by all four cylinders. Thus the bearing loading is non-symmetric by at least this value, and could be larger if there is misalignment or unexpected loading. Though the loads are not perfectly counteracted, the cylinder arrangement does balance the bulk of the loading, reducing the force on the bearing support required. This disparity is ignored for the analysis, as the system

was conservatively designed to support the entirely of the bearing load (from each the top/bottom independently) in case of pressure loss or other mechanical failure led to 100% force difference between chamber groups.

It can be seen in Figure 3.7 that a portion of the linear cylinder force (transmitted through the rack gears) was transmitted radially into the gear, due to the gear angle. Notice that the normal forces from each of the two racks are equal and opposite, due to the symmetric top/bottom loading. A preload also exists on the ball rollers that is provided by compressing an elastic washer material. This minor load simply ensures that the rack gears remain in contact with the pinion gears. The loading due to these ball rollers, due to symmetry introduced a net zero radial load. Thus, provided the pneumatic system was operating normally, and misalignment was not excessive, the symmetric arrangement introduces minimal gear/pneumatic load on the radial bearings. Note that in the unusual event that pressure is lost in one of the chamber groups the symmetric loading would also be lost. As such, to be conservative the radial bearings were selected with this atypical load considered.

The electric motor contains internal radial bearings, but has no significant rating in the thrust direction, and to be conservative these bearing contributions were not considered. Since the gravitational load is the most significant load and the actuator could be operated in the vertical or horizontal, the bearing type for the output shaft was selected such that it can support the load in both the radial and thrust directions. The two angular contact bearings were selected and could support radial loads, thrust loads in both directions, and moment loads when arranged appropriately/back-to-back. The ability to support a moment allowed for the two radial/thrust bearings to be placed at a single position (**D**, in Figure 3.9) in the middle of the output shaft as opposed to the more typical arrangement where the loading is near the middle of the shaft, with a bearing on either end. The single location bearing arrangement allowed for easier mechanical assembly. If the loads with this bearing placement result in angular deflection, the ball rollers

supporting the rack gears would help support the shaft, thus reducing risk of excessive deflection due to the "cantilevered" radial bearing arrangement.

The maximum torque of which the actuators were capable (to be discussed below) was 37.9 Nm for the pneumatic cylinders and 3.93 Nm for the electric motor. This was the maximum torque which the actuators can provide, and thus the maximum that the shaft must transmit. This load, considering the conditions/arrangement previous discussed, determined the maximum load the radial bearings needed to support. The radial load on the bearing was calculated as:

$$F_{bearing} = F_{v,payload} + F_{M,payload} + F_{N,cyl} \tag{3.3}$$

$$F_{bearing} = \left(gm_{payload,\max}\right) + \left(\frac{d_v g m_{payload,\max}}{\frac{w_{bearing}}{2}}\right) + 2F_{cyl}\sin\left(\phi\right) \tag{3.4}$$

where $F_{v,payload}$ is the force due to gravity, the product of the gravitational constant and the payload mass, $m_{payload}$=7 kg, transmitted in shear from the output shaft; $F_{M,payload}$ is the force due to the moment created by the distance between the center of the bearing set and the load, d_v=0.06 m, as well as $\frac{w_{bearing}}{2}$ the distance between the center of the two bearings, and each bearings center, where $w_{bearing}$ =0.012 m; finally $F_{N,cyl}$ is the maximum normal component of a single rack gear force transmission, the sum of two maximum cylinder forces F_{cyl}=312 N. Again, note that $F_{N,cyl}$, is only included to be conservative in case of component failure, during typical operation this value will be zero due to the symmetric loading. Thus the conservative maximum radial bearing load is: $F_{bearing}$ = 969 N.

The bearings selected have a rated load of 13,000 N, more than sufficient for the loading condition, with a significant factor of safety. This load rating is larger than needed, but the bearing was also selected based on its diameter, to match the minimum shaft diameter requirement. The mechanical design of shaft was considered concurrently when selecting the bearings to ensure that the bearing size led to a shaft which could withstand the stresses transmitted.

3.4.3 Output Shaft Design

The shaft was designed to accommodate the selected components (gears, couplings, bearings, *etc*) diameters as well as transmitting the worst case combination of loading, that is to say: maximum motor torque and maximum cylinder torque acting against a matched load torque. The gear shaft also supports the shear and moment loads introduced by the gravitational force on the payload. The worst case loading, as discussed in 3.4.2, was used to analyze the shaft for the worst case combinations due to the torsional, shear and bending loads stresses, as well as the stress concentration points. Using Autodesk Inventor's shaft analysis tool, the loading was evaluated, with figures shown in Appendix A. The output shaft was designed to support the worst case loads, with a factory of safety while also considering the assembly and geometric requirements of the various rotational components selected.

The output shaft to motor coupling only needed to be able to transmit torque up to the motor's peak torque capacity (3.93 Nm), as past this value the motor would not resist additional torque. A helical coupling was selected with a torque rating of 9 Nm, and convenient dimensions based on the motor shaft radius.

The final shaft design consideration was the bolt circle which was used to attach the 90° coupler which connects the output shaft to the link. Six grade 12.9 M3 screws were used to mount the coupler to the output shaft. The arrangement

of the screws is indicated in Figure 3.10. Assuming a 7 kg payload (see section 3.4.2), the loading on the bolt circle was analyzed, assuming the worst case, where the load imparts a shear load due to gravity and secondary shear due to gravity torque. The primary shear is always in the direction of the gravitational load, whereas the secondary is perpendicular to the line of action. In this figure the asterisk indicates the screw with the highest combination of stresses, the full sum of the two.

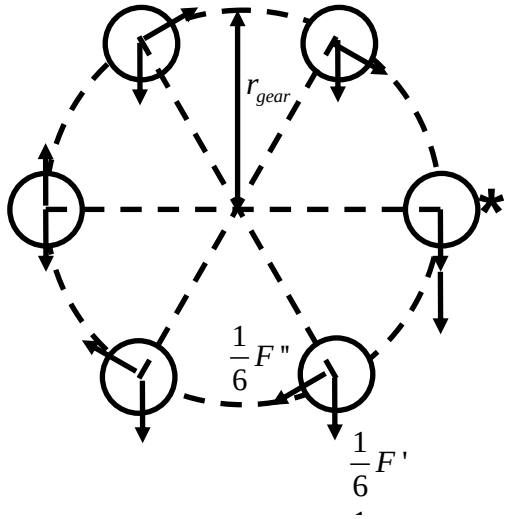

Figure 3.10 Distribution of loading on mounting screws of the link coupler to output shaft.

The shear stress on the screw with the highest stress is then:

$$\tau_* = \frac{F' + F''}{A_{screw}} = \frac{\frac{V}{n_{screw}} + \frac{M}{n_{screw} r_{circ}}}{A_{screw}} = \frac{\frac{(gm_{payload})}{n_{screw}} + \frac{L_{link}(gm_{payload})}{n_{screw} r_{circ}}}{A_{screw}} \tag{3.5}$$

where τ_* is the stress on the screw; A_{screw} = 0.00000448 m^2 is the smallest cross-sectional area of the screw; F' is the primary shear stress and F'' is the secondary shear stress; n_{screw} =6 is the number of screws; V is the shear force and M is the moment; and r_{circ} =0.01125 m is the radius of the screw circle.

Knowing the tensile yield stress for the material, $\sigma_{\text{yeild, tension}}$ =1100 Mpa, using (3.6) the factor of safety FOS = 4.6. This factor of safety is reasonable as stresses could be reversible, and shock loading is possible, if impact testing is performed.

$$\text{FOS}=\frac{\sigma_{\text{yeild, shear}}}{\tau_*}=\frac{\sigma_{\text{yeild, tension}}\,0.577}{\tau_*} \tag{3.6}$$

3.4.4 Pneumatic Circuit Design

The pneumatic circuit was comprised of the pneumatic components as well as the pneumatic lines/fittings which connect them. The connections were designed with the primary concern of minimizing extraneous length between components. This is done to minimize unnecessary pressure losses, as well as minimize the delay between pressure sensors and the chambers themselves. Figure 3.11 shows the pneumatic circuit, schematically; the components will be discussed in detail in the remainder of the section. The pneumatic relevant components are: two cylinders, representing the top two cylinders and the bottom two cylinders; the group 1 pressure shown in red, the group 2 shown in blue, and the supply shown in green; the speed valve, two 3-way solenoid valves, and the pressure sensor for each group of chambers; the supply, supply regulator and supply accumulator. The remaining components represent the electrical, data acquisition, control, and relevant mechanical components.

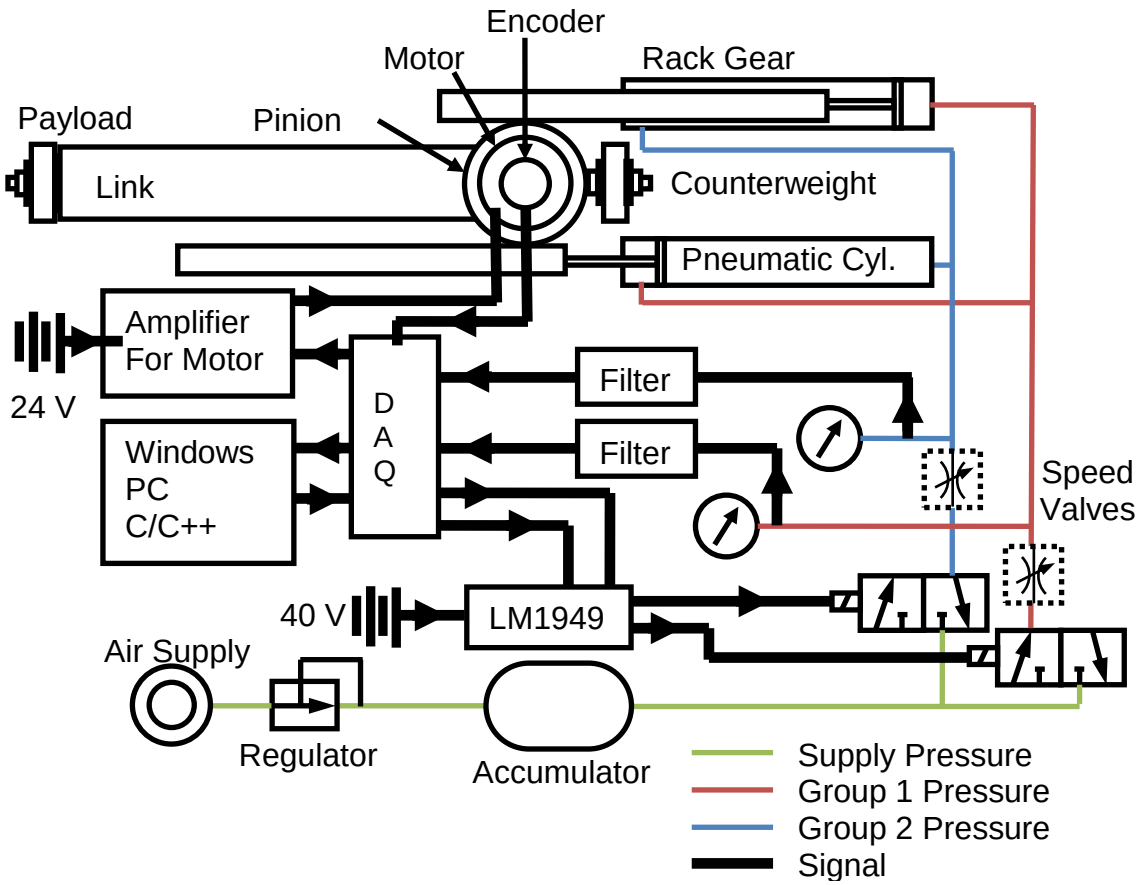

Figure 3.11 Schematic diagram for the pneumatic electrical and mechanical components of the system.

The maximum pressure available was a ~100 psia building pressurized air supply line, as is commonly available in industry. The pneumatic components were selected to meet or exceed this limit. The system is capable of making full use of available pressure, but could be operated at a lower supply pressure if desired. To measure the chamber and supply pressures three pressure sensors were selected with a 0-100 psia range and an accuracy of ±0.5 psia (0.5% full scale).

The pneumatic circuit includes a manually adjustable regulator to allow it to operate at lower supply pressures. During control tuning and system validation (Chapter 6) the system was operated below the maximum operating conditions

for several reasons. First being that the building pressure supply is not tightly regulated itself and operating below maximum is necessary for the regulator to function properly. Secondly to avoid saturation of the sensors in the case of impulses. For example, if the output link was to be suddenly externally loaded, as in an impact or payload increase. This could cause compression in the system faster than air could be vented, possibly exceeding the pressure sensors' effective range, leading to the loss of useful data and risk of damage to pneumatic components. Finally at a lower operating pressure the relative contribution of the motor is larger, or said contribution would have flexibility to be modified by changing the operating pressure. 5 Bar absolute (500 kPa absolute) was selected as a reasonable, even, metric value close to 75 % (72.5 psi) of the sensor's maximum 100 psi rating.

The pneumatic lines were selected to match the valves, and the inner diameter of the ¼ inch tubing is of significantly larger diameter than the valve orifices, which becomes the limiting mass flow point. The length of pneumatic tubing between the cylinder side of the valve, and the respective chambers is considered in the dead zone volume calculation of the chamber in question and is further discussed in Chapter 4.

3.4.5 Solenoid Valve Selection

Two MAC 3-way solenoid on/off valves were selected for this design. Alternatively servo proportional valves could have been used. Yet those such as the commonly used Festo MPYE series cost ~$1000, about 2000% of the cost of a MAC solenoid valve (~$50). Using advanced control to approximate the performance of servo valves but at a fraction of the cost is a desirable element of the research. These on/off valves are the same type used in van Varseveld & Bone (1997), and Bone & Chen (2012), were readily available, and known to perform well.

Recalling Figure 3.11, the speed valves were placed after the solenoid valves to mitigate the pressure oscillations due to the valve switching. Since both the solenoid and speed valves can behave slightly differently from one individual to the other individual, the tuning of the speed valves was done using observed system data. This allowed each to be set to achieve similar performance for both group 1 and group 2, in terms of mass flow rate. Figure 3.12 illustrates the effect of the speed valve on the system, where 3.12 Top shows a pressure tracking experiment with the speed valve fully opened, and 3.12 Bottom shows the same controller/trajectory when the speed valve has been partially closed, limiting flow. It can be seen from the figure, that the oscillation amplitude was reduced by introducing these valves.

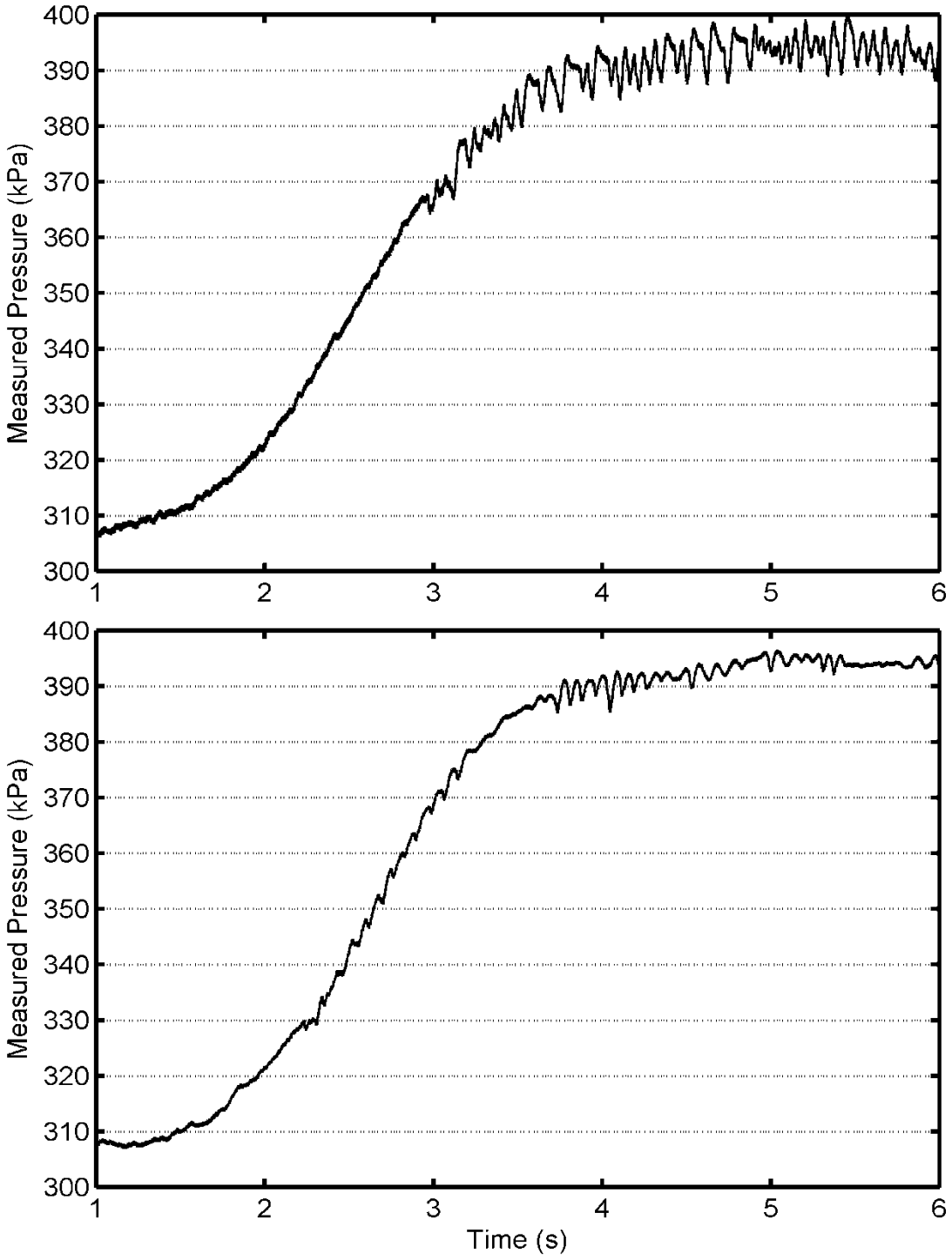

Figure 3.12 Top: Pressure tracking with speed valve fully opened, *i.e.* maximum flow. Bottom: Pressure tracking with the speed valve partially closed.

3.5 Electrical System Designs

Recalling Figure 3.11, the system was controlled using a C console application running on a 64-Bit Windows PC with an Intel i5 2400 3.1 GHz processor. The computer to hardware interfacing was achieved with a National Instruments data acquisition system (DAQ). The supply, group 1 and group 2 pressures were logged via analog input channels, while the motor control signal was sent via an analog output channel. Five high speed digital channels were used for the encoder input and valve control signals. Two are used for outputting the PWM signal to the driving circuit for the two on/off valves. Three were used to capture the A, B and index channels of the encoder. The encoder was a high resolution optical encoder, capable of 80,000 pulses per revolution using quadrature counting. It was coupled to the back-shaft of the motor which was coupled in turn directly to the output shaft of the actuator, and was used to measure the joint's angular position. The high resolution allows for minimal quantization error when using the encoder to estimate current system velocity for the purposes of control. Since the encoder was installed on the back shaft of the electric motor, which was directly coupled to the output shaft, this equated to a joint angular resolution of 0.0045°. This arrangement eliminated the backlash and flexion problems encountered in typical geared electric motors where the encoder is coupled to the motor back shaft, with gearing between the motor shaft and the output shaft (of the gearhead).

3.5.1 Pressure Sensor Signal Conditioning

Batteries were used to power the sensors, as they are superior to low cost transformers in terms of the level of high frequency noise they add to the signal. A relay allowed for computer controlled switching on and off of these sensors to conserve battery life. The pressure sensors being powered by batteries required a special pre-experiment test to ensure that they were operating correctly and the

battery was not too drained. As the sensors were absolute, the values could be compared to one another and the expected atmospheric value. If the sensors varied from one another, then the battery should be replaced. If the value was not reporting atmospheric, then the battery should be replaced. If a gauge sensor was used (instead of absolute) this verification would be more difficult as a measurement of 0 could correspond to atmospheric pressure, or a failure in the sensor due to battery drain. In an alternate implementation, the pressure sensors could be powered by a high quality power supply instead of battery power. Further, the voltage of the pressure sensor power line could also be measured to ensure that the value did not deviate from nominal. During system characterization, the noise levels observed with the pressure sensors were deemed too large and hardware RC low pass filters were introduced. A 95 Hz low pass filter was implemented on each pressure signal line and proved effective in noise reduction, as is clear from Figure 3.13.

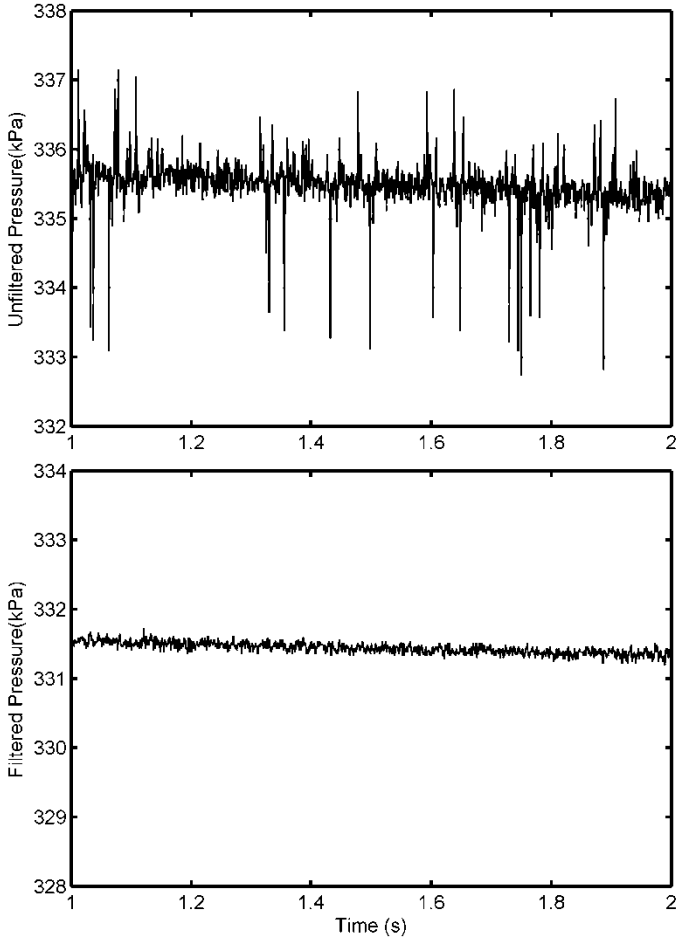

Figure 3.13 Top: Pressure data collected before filter introduction. Bottom: Pressure data collected after implementing an 95 Hz RC low pass filter.

3.5.2 Valve Driving Circuit

PWM allows the approximation of an analog output by switching a digital (on/off) device on for a certain percentage over a short time period, and off for the remainder of the period. This period is repeated and the fraction of on time varied, to achieve an average effect over a longer time period. In general, a shorter PWM period provides a more accurate approximation of an analog output. The dynamics of the particular device determine the minimum PWM time period. In this application, the PWM period had to be long enough that the valve

has time to physically switch over a range of duty cycles, ideally continuously from 0%-100%. The shorter the period, the more rapidly the control signal can be changed to account for desired changes in the control signal. This means that the faster the valve can physically switch from open to closed, and vice-versa, the shorter the PWM period can be set while still maintaining a reasonable duty cycle range.

The standard 3-way solenoid valve functions by being held in its default position by a spring, and when the solenoid is sufficiently energized, the spring force is overpowered by the magnetic force and the valve physically switches. When the solenoid is de-energized, the now compressed spring pushes the valve back into its default position. Valves typically have different response times for the different directions, given the non-symmetric switching forces. The valve opening has three major time regions: switching delay, the transient period, and the open period. The switching delay is the time between the valve command signal being set on and the beginning of the valve physically opening. This delay is introduced as the valve solenoid must energize to a point at which the magnetic force exceeds the spring force plus valve friction force which hold the valve in the default position. The transient period is the time in which the valve has begun to switch, allowing air to flow, but where the valve is not fully open allowing maximum air flow (given the up and down stream pressure conditions). The final period is where the valve has fully physically switched and is fully open. Similar regions exist for valve closing, where the coil must first de-energize to the point at which the spring force exceeds the latent magnetic force and friction.

Due to the aforementioned nature of PWM it is desirable to attempt to reduce the times required for any of these regions. One such way is operate the valves at a higher voltage, which tends to produce a stronger magnetic field, thus accelerating the ferrous valve plunger and reducing transient times. This is often avoided as an increased voltage comes with an increased valve temperature which can reduce valve life. Another method, which can be used in conjunction,

is the use of a more advanced charging circuit which is capable of energizing and de-energizing the solenoid faster than a simple relay. To this end, two circuits (one for each solenoid valve) were constructed based around the LM1949 chip (Texas Instruments (2013)) and a 40 V power supply (in place of the valve rated 24V). The use of transistors in this chip allows the low voltage digital signal from the PC to control the higher voltage required by the valves, as opposed to needing to use relays or optocouplers as is typical. The single valve circuit is shown schematically in Figure 3.14:

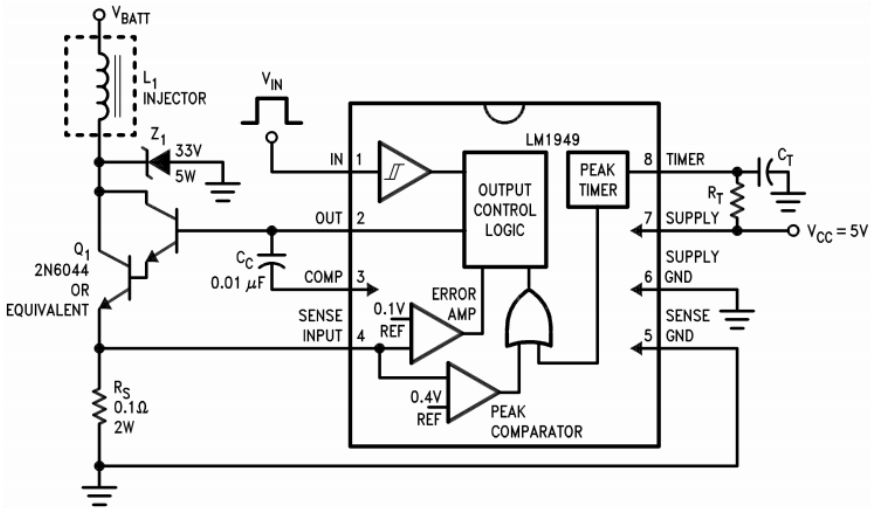

Figure 1. Typical Application and Test Circuit

Figure 3.14 LM1949 valve driving circuit. Texas Instruments (2013).

The components of this circuit were manually tuned for the specific valve in an effort to decrease the switching time, as well as holding current. Maximum current was required, as quickly as possible to charge the solenoid and attract the valve plunger, but after friction is overcome it is desirable to drop the current slightly. This is because less force was required to simply hold the valve in a position, and the reduced current will allow the solenoid to de-energize more quickly when the control signal is set to LOW, thus allowing for quicker closing

time. Furthermore this reduces the energy required to hold the valve open and will result in lower waste heat. Figure 3.15 illustrates a typical current profile in the solenoid when using the LM1949 circuit.

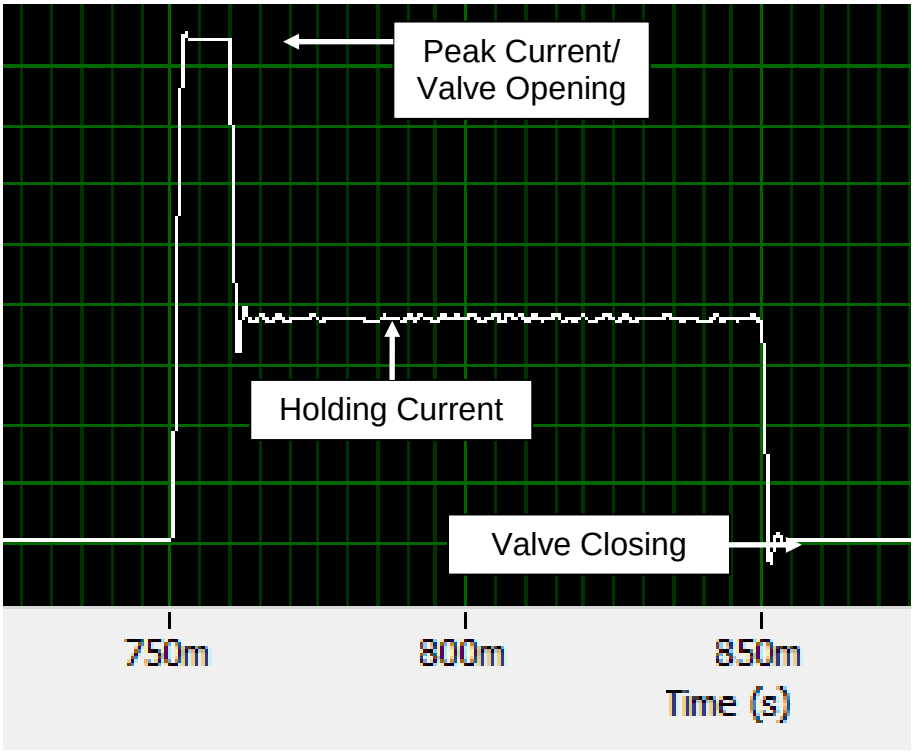

Figure 3.15 Typical solenoid current profile with LM1949.

The supply and atmospheric pressures, valve dynamics and PWM period all play a role in the actual functional duty cycle range that elicits a pressure change in the system. The duty cycle range is more than a simple product of the valve delays and PWM period. This is because the valve open-to-close response depends on the previous action and thus the current state (opening, closing, holding, *etc*). For very low duty cycles, where the portion of the PWM period where the valve should be closed is large, the valve might still be attempting to open from the previous period, and vice-versa for very high duty cycles. Due to

the complexities of behaviour, the PWM period for control was selected via experimental observations.

The same type of valve was PWM controlled in van Varseveld & Bone (1997), where a PWM period of 16 ms was used. As they did not use the LM1949 circuit, and were controlling the system with a slower computer, the 16 ms PWM period was appropriate. For the GEN2 actuator it was desirable to attempt to decrease the PWM period. The shorter the PWM period can be made, the more rapidly the control signal can be updated to respond to the system state and errors. The trade off being that decreasing the PWM period decreases the range of duty cycle range at which the system can be effectively controlled. Figure 3.16 shows the plotting of several PWM periods which were considered. The link was clamped in place, and valve duty cycle was step increased until appreciable pressure change was seen in the system. When the filling step increases, the duty cycle was returned to 0% between steps. Then the valve was step decreased in duty cycle until a pressure drop was observed. For discharging, the duty cycle was returned to 100% between steps. The specific dynamics of the pressure were not important at this stage, only the points in duty cycle at which a macroscopic pressure change occurs. The specific relation between air mass flow rate (and thus pressure change) and the PWM duty cycle is further discussed in Chapter 4. This plot simply allows for the PWM period to be selected knowing the general response of the system, before modelling. The 8 ms period was selected for its effective range, as well as being a significant improvement over the 16 ms period previously used. It can be observed that for filling (increasing stairs in the plot) the minimum duty cycle which effects a change increases with increasing PWM period. For the discharging (decreasing stairs in the plot), the maximum duty cycle at which pressure change occurs becomes larger with increasing PWM period. It can be seen that 8 ms is the shortest period at which there is not a significant deadzone seen for discharging. Choosing the shortest period with a reasonable effective duty cycle range was desirable, as the

shorter the PWM period, the more often the control signal can be changed to respond to system conditions. Throughout further modelling development, control design, and system validation, this 8 ms value did not prove to be unsuitable.

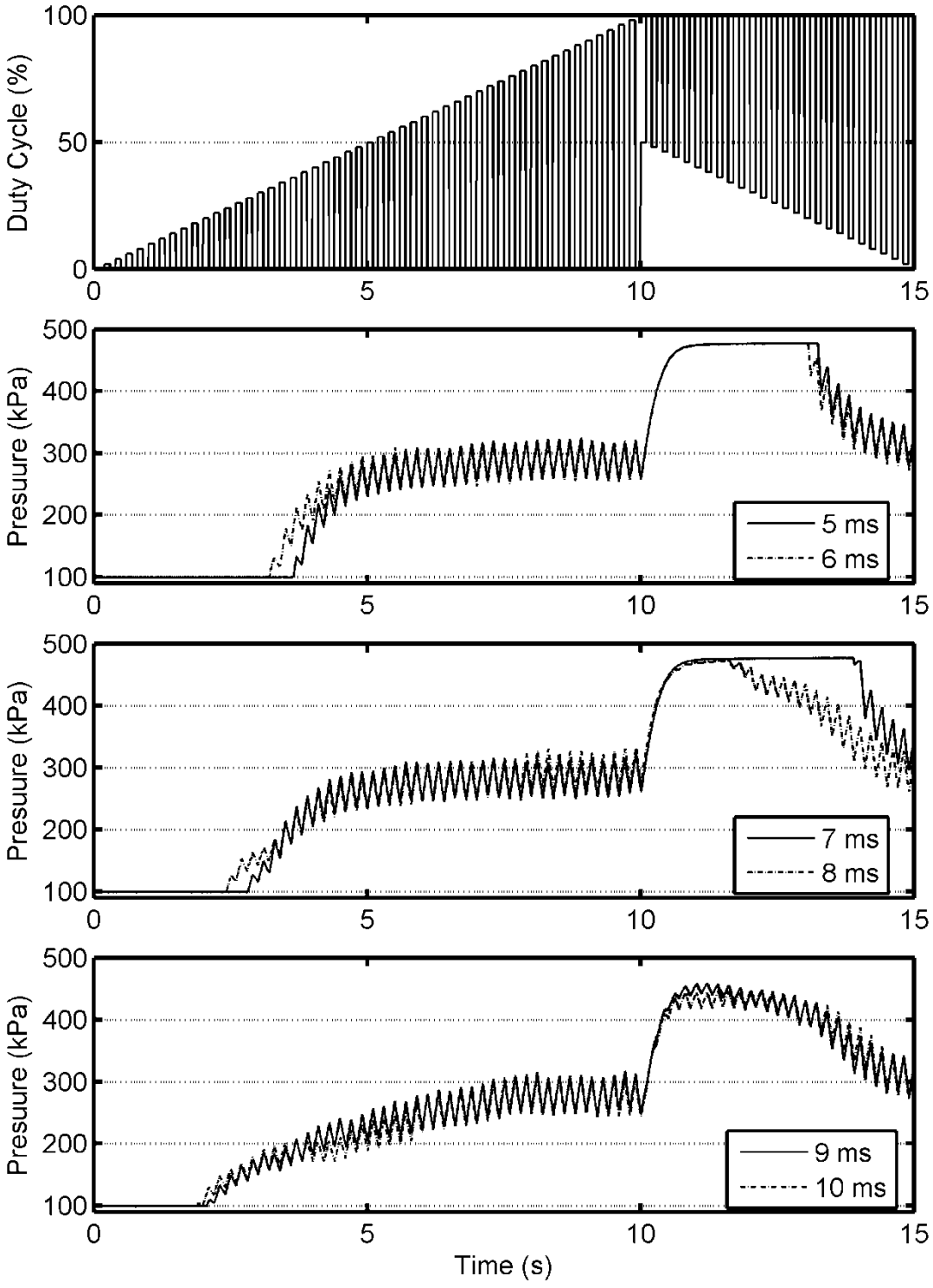

Figure 3.16 Examples of pressure change across duty cycles for PWM periods between 5-10 ms.

3.5.3 Electric Motor Selection

The major goals of the hybrid actuator design, when considering human safety were: low inertia, low joint stiffness, and low friction. The electric actuator is included in the overall HPEA with the goal of compensating for the slow response and poor accuracy of the pneumatic actuator by providing additional torque. Simultaneously, the electric motor and any required gearing should be selected for minimum inertia and friction increases in the overall system. These two factors are in opposition, and both must be considered simultaneously. With this in mind, it was decided to directly drive the output shaft with the electric motor to avoid adding the friction and reflected inertia that is caused by gearing. The final consideration is the ability for the motor to provide the torque to compensate for the deficiencies of the pneumatic actuator. Too large of a motor would be impractical in terms of size/weight/cost as a robot actuator, and would negate the need for the large torque capacity of the pneumatic actuator. Too small of a motor would not have the ability to affect the hybrid output, especially in the vertical configuration where the external load is high due to gravity. Bone & Chen (2012), suggest that the electric motor should be capable of providing approximately 10% the torque that the pneumatic system can provide. This ratio worked well for the GEN1 system, and was retained for this system. Several electric motors were conveniently available, the most suitable of which was brushless DC servomotor with a peak torque rating of 3.93 Nm (see Table 3.5), 10.4% of the pneumatic actuator's maximum of 37.9 Nm. If the GEN2 was operated in the pneumatic mode, or in the hybrid mode when the pneumatic torque dominated, the motor would act as a generator. The generated voltage is termed back-EMF. If too much back-EMF is generated the motor controller/amplifier circuits could be damaged either directly electrically or thermally. The back-EMF is proportional to the speed at which a motor is backdriven. For the motor used the voltage constant was 12.1 V/kRPM (Table 3.5) when driving the motor, as such a similar value would be apply when

backdriving it. Since the motor is directly coupled to the output shaft the maximum motor speed is fairly low when it was backdriven. If the motor was coupled through gearing the motor velocity and back-EMF would have been much larger. From Table 3.6 it can be seen that the maximum motor velocity estimated for the GEN2 is expected to be 181°/s = 0.03 kRPM. This corresponds to a back-EMF of 0.36 V which is negligible compared to the 48 V used to drive the motor.

Table 3.5 Electric motor specifications.

Specification	**Electric Motor**
Operating Voltage (V)	24
Peak Torque (Nm)	3.93
Max. Continuous Torque (Nm)	1.23
Voltage Constant (V/kRPM)	12.1

3.6 Torque Capacity

With the selection and arrangement of the components completed, the HPEA output torque (neglecting losses) can be defined by:

$$\tau_{pneum} + \tau_{motor} = 2r_{gear}\left(F_{Cyl,push} + F_{Cyl,pull}\right) + \tau_{motor} \tag{3.7}$$

where τ_{motor} is the motor torque; τ_{pneum} is the pneumatic cylinder array torque; r_{gear} is the radius of the pinion gear; $F_{cyl,push}$ is for force of the pair of cylinders helping to push the pinion gear, and $F_{cyl,pull}$ is the force of the pair of cylinders on the other side of the pinion gear, acting to "pull" on the pinion gear. The detailed definitions of these forces are presented in Chapter 4.

Given the maximum operating pressure of 689 kPa, and the cylinder/rod areas, the pinion gear radius, as well as the peak motor force, the system peak torque was 41.8 Nm. The payload mass, and the maximum acceleration of said mass, varies with the selected link length. At 0.5 m, as in the GEN1 arm, the maximum payload statically held against gravity (ignoring the friction and acceleration contributions which would be required for position control, and assuming the mass of the arm was balanced by the counterweight) would be 8.5 kg. At the length of 1 m this payload would be half at 4.26 kg. At 0.6 m the payload would be 7 kg. If the payload was reduced to allow for an estimated 30% of the torque to be used for inertial loads, frictional loads and disturbance rejection, the payload could be rated at 5kg in the vertical. This payload still falls within the desired capacity (see Table 3.1), as compared to the commercially available robots. Thus the 0.6 m arm was used a solution to generate both large inertial loads and gravitational loads. The torque, 41.8 Nm is smaller than those listed in Table 3.1. The commercial actuators needed to have larger shoulder torques as they must support the payload as well as the mass of the heavy electric motors/gearings of the additional joints. If the GEN2 actuator was used in

combination with additional actuated joints the payload capacity would be reduced, or a shorter link could be used. Further, some of the additional joints could be wire driven, for example, to reduce the mass increase introduced by additional actuators. For the best system design, the actuator (e.g. GEN2) would need to be selected or designed knowing the number of additional joints, and the specifications/masses of the actuators. As indicated by the torque/payload trend in Table 3.1, if multiple joints were used in the next, GEN3 ,system the shoulder joint would likely need a larger torque capacity to support the payload and additional actuators. The specific increase in torque requirement would be dependent on the number and type of actuators used.

Compared to a purely electric system, the relative inertia of the GEN2 hybrid system can be evaluated. If the electric motor used for this hybrid system was used by itself, to produce the same continuous torque (39.1 Nm, see Table 3.6) at least 32:1 gearing would be required. This could be accomplished by a stack of five 2:1 planetary gearheads, for example. The inertia of the motor alone (not including the gearing inertia) would be reflected 1024 times larger to the output side, as 0.1374 kgm^2. Whereas the GEN2's motor plus cylinder plus rack gear (see Table 4.1) inertia is only 0.0018 kgm^2. Thus the purely electric solution's actuator inertia would be at least 76 times larger than that of the GEN2 HPEA.

3.7 Conclusions

In addition to the major mechanical and electrical design features described above, additional features such as a mounting frame, hard stops, limit switches, encoder indexing, etc were implemented. These were implemented in standard fashion and did not warrant discussion. This chapter presented the motivation and desired capabilities of the system based on the desired application and the prior art. Furthermore this section presents the relevant

design, calculation, and component specifications of the selected or built system components. Table 3.6 summarizes the specifications of the GEN1 actuator, and the improved GEN2 actuator's maximum and validation specifications. The capabilities of the system are well within the desired range shown in Table 3.1. It can also be seen that this actuator is capable of producing 511% more continuous torque than the GEN1 actuator, with an increase of system inertia (without payload) of only 292%. The next chapter presents the modelling of the GEN 2 actuator.

Table 3.6 GEN 1 system specifications compared to GEN 2 maximum specifications, and the GEN 2 specifications at the pressure used for system validation (in Chapter 6).

Specification	**GEN1 Actuator (Max) Chen (2012)**	**GEN2 Actuator (Max)**	**GEN2 Actuator (Validation Pressure)**
Operating Pressure	345 kPa	689 kPa	500 kPa
Max. Pneumatic Torque	5.85 Nm	37.9 Nm	27.5 Nm
Peak Electric Torque	2.47* Nm	3.93 Nm	3.93 Nm
Continuous Electric Torque	0.55* Nm	1.23 Nm	1.23 Nm
System Friction Estimate	0.11 Nm**	0.23 Nm††	0.23 Nm††
Range of Motion	0° to 180°	231°	-10° to 200°
Actuator Arrangement	Parallel	Parallel	Parallel
Encoder Position	On motor, geared to output shaft	On motor, coupled to output shaft	On motor, coupled to output shaft
System Inertia (without Payload)	0.022 kgm^2	0.0862 $kgm^{2\dagger}$	0.0862 $kgm^{2\dagger}$
Max. Payload (0.6 m arm length)	1.0 kg***	5.0 kg***	3.7 kg***
Max. Speed	184°/s†††	185°/s†††	185°/s†††

*at 5:1 gear ratio.
**Static friction.
***Allows for 30% of max. torque capacity to be used for non-gravitational loads (*e.g.* acceleration, friction, and disturbance rejection)
†See chapter 4 for inertia calculation.
††See Table 6.6 "Zero Gravity" Loading condition, *i.e.* the friction compensation used with no payload.
†††Assumes the half of the 30% torque not allocated for gravity is used to accelerate at maximum for 0°-90° of the range, and decelerate at maximum for the remaining 90°-180° of the move, with the max payload at 0.6 m arm length.

Chapter 4: System Modeling

4.1 Introduction

A mathematical model of the physical system was required for model-based control design. This chapter presents the development of the overall system dynamic model and its constituent components. Particular attention was paid to development of the cylinder and chamber group pressure dynamics model. A black-box ANN was developed to create an inverse model for the solenoid valves. A simple inverse model of the electric motor was also experimentally determined. The models allowed for the development of closed-loop torque and position control algorithms in the proceeding chapter.

4.2 System Acceleration Model

The hybrid system was composed of two actuator types: the pneumatic cylinders, and the electric motor, which output force and torque respectively. The system output was the radial position of, and/or the torque applied to, the output link and payload. Due to the dual linear and rotational nature of the system, and the coupling between them, each could have been expressed in terms of the other. Due to the rotational nature of the output, the overall system was expressed in rotational terms where possible and linear terms were only used where appropriate.

Recall Figure 3.3 the mechanical assembly drawing of the GEN2 actuator. This figure illustrates the mechanical components in the system and the coupling between them. If the linear components are written as their rotational equivalent then the lumped system can be summarized by the single free body diagram, Figure 4.1. The free-body diagram is expressed mathematically in (4.1)-(4.4). The lumped system's mass/inertia was written as an equivalent rotational inertia seen at the common output shaft.

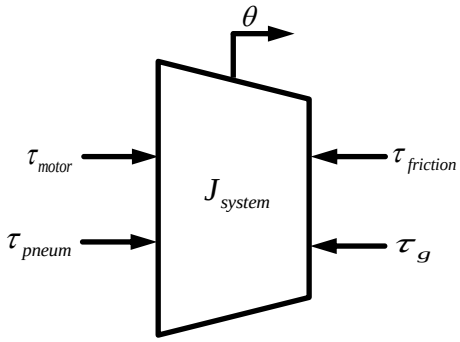

Figure 4.1 GEN2 free body diagram expressed as a lumped rotational inertia at the common output shaft. Recall the direction of positive motion from Figures 3.3 and 3.5.

$$J_{system}\ddot{\theta} = \tau_{net,system} \tag{4.1}$$

$$\tau_{net,system} = \tau_{motor} + \tau_{pneum} - \tau_g - \tau_f \tag{4.2}$$

$$\tau_g = \tau_{g,link} + \tau_{g,payload} \tag{4.3}$$

$$J_{system} = J_{motor} + J_{link+CW} + J_{cyls+racks} + J_{shaft} + J_{payload} \tag{4.4}$$

where J_{system} is the total system inertia, as seen at the common output shaft; $J_{link+CW}$ is the inertia of the link, link coupler, and counterweight; J_{motor} is the inertia of the motor shafts, internal bearings, and rotor; $J_{cyls+racks}$ is the inertia of the rack gears, cylinder rods/pistons, and cylinder to rack couplers, transmitted across the pinion gear with respect to the output shaft; J_{shaft} is the inertia of the output shaft, pinion gear, motor coupler, and inner bearing races; $J_{payload}$ is the inertia of the payload mass, with respect to its rotation about the output shaft; $\ddot{\theta}$ is the output shaft and link common angular acceleration; $\tau_{g,link}$ is the gravitational torque load due to the link and counterweight; $\tau_{g,payload}$ is the gravitational torque due to the payload mass; τ_{motor} is torque output from the motor; τ_f is the torque due to

friction; τ_{pneum} is the total torque contribution of all four cylinders; and $\tau_{net,system}$ is the net sum of torques acting on J_{system}. Torque $\tau_{g,link}$ is balanced and results in net 0 Nm gravitational load if the counterweight is in place, otherwise it is the gravitational effect of the link. Torque τ_{pneum} is defined by:

$$\tau_{pneum} = r_{gear}\left(F_{group2} - F_{group1}\right) \tag{4.5}$$

where r_{gear} is the pitch radius of the pinion gear. F_{group1} and F_{group2} are the total forces generated by each of cylinder groups respectively.

4.2.1 System Rotational Inertia

The rotational inertia of the system was the sum of the individual inertias of the basic system components. Every moving part of the system contributed to the inertial load, which was considered in five separate groups:

- link coupler, link, and counterweight;
- cylinder rods/pistons, and rack gears;
- motor coupler output shaft, pinion gear, and inner bearing races;
- motor shaft and rotor;
- payload

The individual group inertias, and sum total system inertias, depending on loading condition are summarized in Table 4.1, at the end of 4.2.1.

As shown in Figure 4.2 the link, L_{link}, was a long foam core ABS cylindrical tube. Its value of L_{link} =0.56 m was designed to allow for a payload to be placed at 0.6 m from the rotation point. The length provided the moment arm necessary to generate a reasonable gravitational and inertial load while not being too large for the available lab space. An aluminum coupler was machined to accommodate coupling the output shaft to the link at a 90 degree angle. The coupler is used to mount both the link, and the backshaft used to mount the counterweight. (4.6)

describes how d_{CW} =0.11m, the distance between the counterweight and center of rotation, was selected to balance the unloaded link's gravitational load.

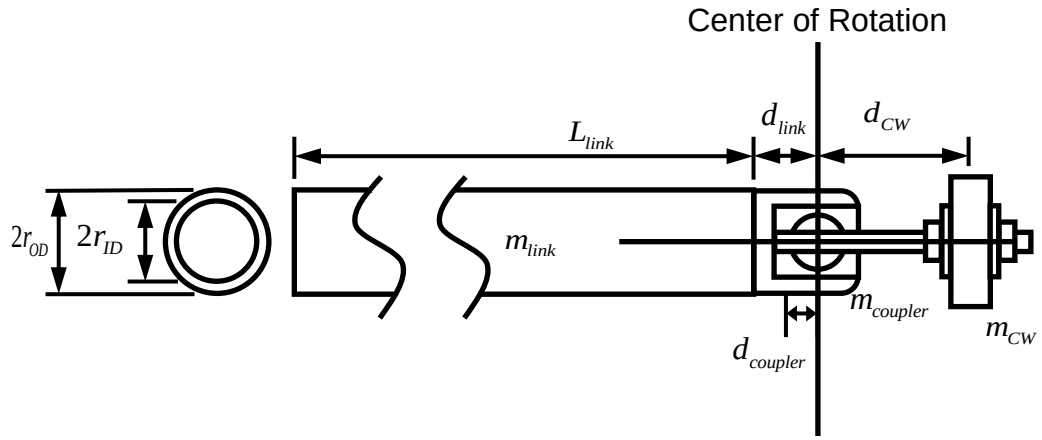

Figure 4.2 Diagram of link and counterweight.

$$d_{CW} = \frac{m_{link}\left(\frac{1}{2}L_{link} + d_{link}\right) + m_{coupler}d_{coupler}}{m_{CW}} \tag{4.6}$$

where m_{link} =0.43 kg is the mass of the link; d_{link} =0.03 m is the distance between the start of the link and the center of rotation; m_{CW} =1.228 kg is the mass of the counterweight; $m_{coupler}$ =0.1kg is the mass of the link coupler; and $d_{coupler}$ =0.04 m is the distance between the rotation point and the center of mass of the link coupler.

The inertia of the link+counterweight assembly was then calculated as:

$$J_{link+CW} = \left(m_{link}\left(\frac{1}{2}L_{arm} + d_{link}\right)^2 + \frac{1}{12}m_{link}\left(3\left(r_{OD}{}^2 + r_{ID}{}^2\right) + L_{arm}{}^2\right)\right) + m_{coupler}d_{coupler}{}^2 + m_{CW}d_{CW}{}^2 \tag{4.7}$$

where r_{ID} and r_{OD} are the inside and outside diameters of the link, respectively.

The masses of the four cylinder pistons/rods, the coupling brackets, and the two rack gears had linear inertia, but were coupled to the rotational system

via the pinion gears. These masses were modeled as a single point mass acting at the gear pitch radius, and then included in the total system rotational inertia as:

$$J_{cyl+racks} = (2m_{gear} + 4m_{cyl})r_{gear}^{\ 2} \tag{4.8}$$

where m_{gear} and m_{cyl} are the rack gear mass and cylinder piston/rod assembly masses, respectively.

The payload's inertia $J_{payload}$ is modeled as simple point mass $m_{payload}$, at distance $d_{payload}$ from the rotational center of the output shaft.

$$J_{payload} = m_{payload}\left(d_{payload}\right)^2 \tag{4.9}$$

The motor's inertia was obtained via the manufacturer's specifications. The subgroup inertias and sum total system inertias (as in (4.1)) for the three masses used for system validation are presented in Table 4.1.

Table 4.1 Summary of rotational inertias for components and sum total system inertias in a variety of configurations

Component/Configuration	**Inertia (kgm^2)**
Linear Components	0.00170
Motor	0.00013
Rotary Components	0.00022
Backshaft + Counterweight	0.0162
Unloaded Link	0.0679
System Total: No payload, "Zero Gravity"	0.0862
System Total: (+1.354 kg payload) "Nominal Payload"	0.5692(+0.4830†)
System Total: (+0.820 kg payload)	0.3770(+0.2908†)
System Total: (+1.840 kg payload)	0.7652(+0.6790†)

† the portion of inertia due to the specified mass increase, mounted at the end of the link.

4.2.2 Inertial Torque

Any moving component has mass, and depending on geometry and arrangement from the rotation point, that mass will have a rotational inertia. To accelerate this inertia, a torque is required, and thus becomes a load on the system. From (4.1) it can be seen that the inertial torque was defined as:

$$\tau_{inertia} = J_{system}\ddot{\theta} \tag{4.10}$$

where $\tau_{inertia}$ is the torque required to accelerate the total base system plus payload inertia at the rate of acceleration desired.

The magnitude of torque required was then dependent and proportional to the particular trajectory desired. As is further discussed in Chapter 6, the system was controlled and validated with trajectories which are smooth in position, velocity and acceleration. Specifically a cycloidal position trajectory (further discussed in Chapter 6) was selected, as it was representative of a trajectory used for point to point moves in a practically implemented robot actuator. From the magnitude and move time duration desired, the position, velocity, and acceleration trajectories were generated. For the validation testing of Chapter 6, the cycloidal move generating the largest desired acceleration was a 0° to 90° move over 4 seconds. A maximum acceleration of 35.3°/s^2 (0.6 rad/s^2), which for the example of the 1.35 kg payload loaded system ("Nominal Payload" in Table 3.1) corresponds to a maximum of 0.29 Nm required to accelerate the inertial load. Also used in Chapter 6 was a position trajectory of a 0.5Hz, 40° amplitude sine wave. For this trajectory the maximum acceleration was 197°/s^2 (3.44 rad/s^2), which for the same payload requires 1.66 Nm torque at maximum. Due to the trajectories' acceleration torque requirements, the specific trajectory the system is capable of achieving is dependent on the torque available from the actuators, and the other loads on the system, such as gravity and friction.

4.2.3 Friction Torque

The system friction is a complex combination of the frictions from the variety of subcomponents. The pneumatic cylinders were selected for their low friction properties, though it is possible that the friction can vary with piston position and loading condition. If the pneumatic cylinder mount and the rack gear are not well aligned then at the extreme extension or contraction the cylinder piston and rod could bind against the cylinder housing. For this reason the cylinder to rack gear coupling was a ball in socket design allowing for some flexibility. Furthermore the rack support bearings were preloaded against the gear groove via a compliant elastic material. This allowed some play in the rack gear, while still maintaining contact with the pinion gear. This flexibility lowered the cylinder damage risks due to binding, though also makes the frictional loading less repeatable.

A system friction model, such as in the one used in the GEN1 actuator (Chen, 2012) considered the friction components of: static, dynamic, and viscous friction:

$$F_{cyl} = \begin{cases} F_{cf}\, sign(\dot{y}) + C_{vf}\dot{y} & |\dot{y}| > 0 \\ F_{static} & \dot{y} = 0 \end{cases} \tag{4.11}$$

where F_{cyl} is the friction force estimate for the system; F_{cf} is the Coulomb (dynamic) friction; C_{vf} is the viscous friction coefficient; and $\dot{y}$ is the linear velocity of the cylinder.

Regardless of vertical or horizontal configuration of the GEN2 actuator the friction was a function of the payload and link mass, and as such the values used were developed for the a specific, nominal mass, as well as for the "zero gravity" loading condition (Table 6.1). To characterize the static friction, the link/payload was supported from below. The torque desired was increased until the link began to move upward. The gravitational torque of the payload/link was subtracted, and

the static friction value remained. The dynamic friction component was more difficult to measure due to its dependence on velocity, as well as variation with position/torque (due to the cylinder seals, cylinder-to-rack alignment, flexibility in the rack gear supports, *etc*).

Practical implementation of friction compensation based on (4.11) can also be difficult due to quantization and noise in sensors. The real friction load direction is dependent on the sign of angular velocity, and the friction regime changes from static to dynamic near zero velocity. Compensation for these behaviours is made difficult by the influence of sensor noise where the sign of the estimated velocity can rapidly switch. This in turn leads to the friction compensation torque rapidly changing signs, and possibly causing the sign of $\tau_{net,system}$, the net system torque (as in 4.2) to change. The closer the desired velocity is to zero, the more of a chance that the same magnitude of error could create a sign change in velocity and thus friction load. During the control development (Chapter 5/6) the friction parameters and implementation of the friction compensation was explored. As the friction compensation regime changes from a larger static value, to a suddenly lower dynamic friction level, or when the friction sign changes, a step is added or subtracted from the desired torque. This led to a step change in the pressure desired, and ultimately mass flow requested from the ANN. This step change was not well handled by the inverse valve models and relatively slow to respond pneumatic system, and led to decreased position tracking accuracy.

It was found that by using a constant friction value, between that of the average dynamic and static friction values, though less physically representative, led to better control. This is because the constant value did not introduce major oscillation, as the multiple step changes of a more complex friction model would. Furthermore, the desired velocity was used in place of the sensor calculated

velocity, to avoid frequent sign changes (and torque steps) due to sensor noise. The model on which the friction compensation is based is defined by:

$$\tau_f = \begin{cases} \tau_{f+} & \dot{\theta} > 0 \\ 0 & \dot{\theta} = 0 \\ \tau_{f-} & \dot{\theta} < 0 \end{cases} \tag{4.12}$$

where the estimated friction load τ_f is velocity dependent; τ_{f+} is the positive friction compensation constant, and τ_{f-} the negative friction compensation constant. The friction compensation is further discussed in Chapter 5. The values in (4.11) were initially estimated by first commanding the link to move over a position trajectory. The torque output of the pneumatic actuators was estimated using the pressure sensors. The difference between this calculated torque and the desired torque (based on gravity and acceleration requirements) was the torque error, assumed to be primarily composed of the friction load torque. This value is only an estimate of the friction load. Ten trials were performed, and the friction estimate was averaged across all ten trials. The positive torque mismatch average and maximum was 0.46 N and 1.2 N respectively. The negative torque mismatch average and maximum was 0.65 N and 1.3 N respectively. Figure 4.3 shows the plotting of the maximum and minimum torque mismatch for every sample, plotted at the matching velocity value. This figure illustrates the large variation in friction across the datasets. The data was collected from a 0° to 90° to 0° move over ~21 seconds. This slow move was used simply to establish a baseline value to be used. For the nominal payload, and faster trajectories used, the value was higher due to the dynamic friction effects. Using the aforementioned values as a basis, the constant friction compensation values were then tuned for best position tracking performance. This tuning of the best value for the friction compensation constants was done concurrently with the other model/controller parameters, as described in Chapter 6, section 6.4.

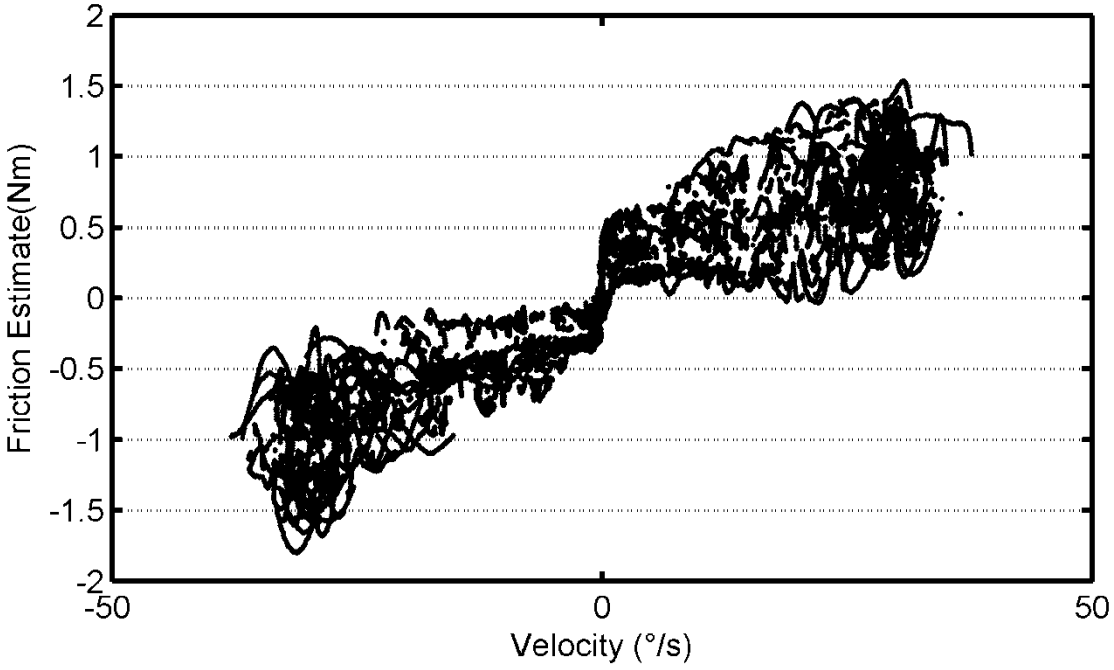

Figure 4.3 Maximum and minimum torque mismatch (friction estimate) of each sample from 10 positive/negative moves from 0°-to-90°-to-0°.

4.2.4 Payload Gravity Torque

When the GEN2 actuator was operating in the vertical (as in Figure 3.3), the payloads' gravitational load affects the system in the direction of the plane of motion. The actuator could also have been operated in the horizontal, rotated 90 degrees from the vertical orientation such that the gravitational load would be perpendicular to the plane of motion, and would not need to be considered in the acceleration model. In the vertical arrangement the gravitational load was a function of the link angular position, being maximum when the link was perpendicular to the direction of gravity and zero when the link is aligned in the direction of gravity.

The payloads used for evaluation were small, dense masses which could effectively be considered as point masses collected at their center of mass for inertial and gravitational considerations. The gravitational load then became:

$$\tau_{g,payload} = d_{payload}\left(m_{payload}g\right)\sin\left(\theta\right) \tag{4.13}$$

The mass of the link itself and counterweight were not considered for gravity loading. The gravitational loads of each acted in opposing directions, and the counterweight was positioned to make these values equal, leading to a net zero gravitational contribution. If no payload as present, then the gravitational loading total became zero and loading on the system as only inertial and frictional. This is the payload configuration which was analogous to the entire system operating in the horizontal plane, instead of the vertical.

4.2.5 Pneumatic Cylinder Torque

Recalling Figure 3.5 the chamber grouping, and (4.5) the net torque output of the cylinder groups can be expressed as:

$$\begin{aligned}\tau_{pneum} &= \left(F_{group2} - F_{group1}\right)r_{gear} \\ &= \left(2\left(P_2A_A + P_2A_B\right) - 2\left(P_1A_A + P_1A_B\right)\right)r_{gear} \\ &= 2r_{gear}\left(A_A + A_B\right)\left(P_2 - P_1\right) \\ &= r_{gear}A_{pneum}\left(P_2 - P_1\right)\end{aligned} \tag{4.14}$$

where P_1 and P_2 are the pressures in the group 1 and group 2 chambers, respectively; A_A is the piston area on an *A* chamber side; and A_B is the piston area on a *B* chamber side. Since the groups are comprised of two *A* and two *B* chambers each, their total pressure areas, A_{pneum}, are equal. A_{pneum} can be expressed in terms of the piston and rod radii as follows:

$$\begin{aligned} A_{pneum} &= 2\left(A_A + A_B\right) \\ &= 2\left(\pi\left(r_{piston}\right)^2 + \pi\left(\left(r_{piston}\right)^2 - \left(r_{rod}\right)^2\right)\right) \\ &= 2\pi\left(2\left(r_{piston}\right)^2 - \left(r_{rod}\right)^2\right) \end{aligned} \tag{4.15}$$

where r_{piston} is the radius of the piston and r_{rod} is the radius of the rod.

4.2.6 Electric Motor Torque

The electric motor has the advantage of a relatively fast response and a relatively simple model compared to the pneumatic system. The amplifier used with the motor accepted an analog voltage as a command signal, and then applied the appropriate current to the motor. The manufacturer did not describe the command signal to torque relationship of the amplifier and motor, therefore it had to be characterized experimentally.

To characterize the electric motor a 0-5kg shear strain gauge-based load cell was used with an analog strain gauge amplifier. The amplifier provides an adjustable sensitivity and 500 Hz hardware low pass filtering to reduce noise. A series of known masses were used to calibrate the sensor (i.e., load cell and amplifier) over a 0-5 kg range. The loading and response data is available in Appendix B. From this data, the sensor could be well described by:

$$V_{loadcell} = 9.928F_{loadcell} - 2.424 \tag{4.16}$$

with a fit of $R^2 = 0.999998$. $V_{loadcell}$ is the voltage output of the sensor and $F_{loadcell}$ is the loading force on the sensor.

After calibration, the sensor was arranged to contact the link perpendicularly, a range of command signal voltages was stepped through, and the corresponding force value from the sensor was recorded. Knowing the

moment arm of the contact point of the sensor, the motor torque was calculated. The relationship between the command signal and the calculated motor torque (i.e., the inverse motor model) was fit with $R^2 = 0.9998$ by the 3rd order polynomial:

$$u_{motor} = 0.917\tau^3_{motor,measured} + 0.0747\tau^2_{motor,measured} + 0.5083\tau_{motor,measured} + 1.973 \text{ Volts} \quad (4.17)$$

where u_{motor} is the motor command signal, and $\tau_{motor,measured}$ is the measured motor torque. The data was plotted along with the fitted polynomial in Figure 4.4.

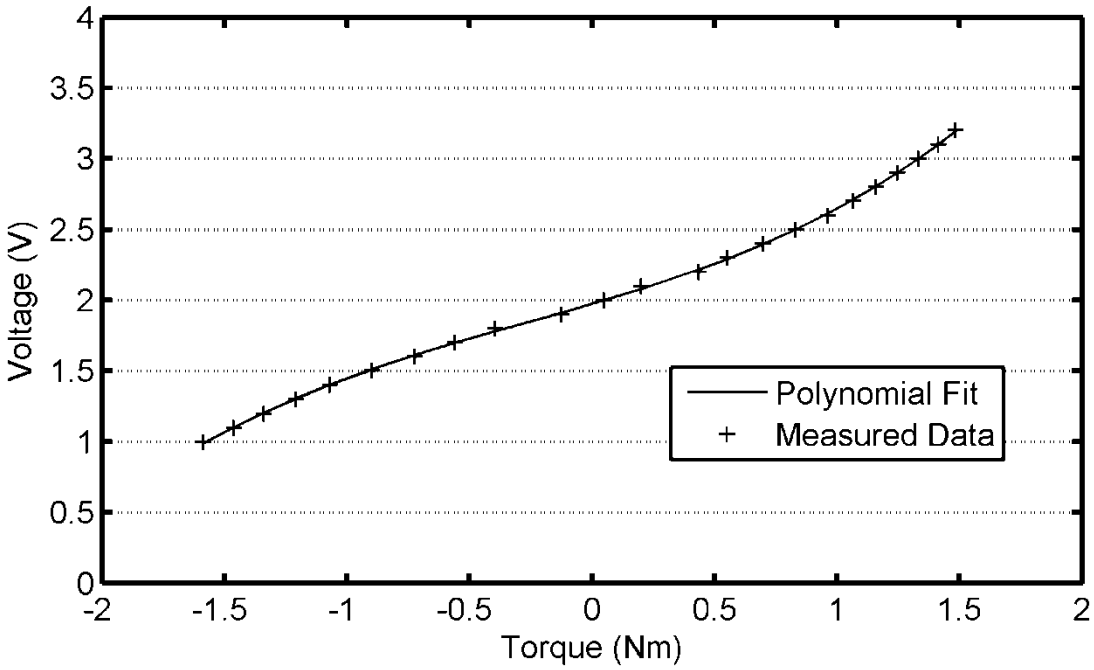

Figure 4.4 Motor torque to command signal voltage relationship and 3rd order polynomial fit. Data available in Appendix B.

4.2.7 Pneumatic Transmission Efficiency

During controller development it was observed that the actual torque produced by the pneumatic actuator was significantly less than the predicted value. A percentage of the generated torque was lost between the pneumatic

actuators and the payload/output link. The torque loss was due to transmission inefficiency from sources such as the gears, flexion in components, modeling error and misalignment. It was found that this loss was consistent enough to be modelled using (4.18) and compensated for in the controllers presented in Chapter 5.

$$\tau_{pneum}(t_i) = \eta_{transmission} r_{gear} A_{pneum} \left(P_2(t_i) - P_1(t_i) \right) \tag{4.18}$$

where $\eta_{transmission}$ is the transmission efficiency.

To estimate the efficiency, a similar process to the motor characterization was performed. The force sensor was used, and a force was applied by the link, from below the sensor, using only the torque from the pneumatic actuator. The link was position controlled until it contacted the sensor at ~90°. Then by setting a desired torque directly (instead of allowing the position controller to set the desired torque) a series of step torque set-points were made. The pneumatic torque, τ_{pneum} was estimated via the pressure sensors and (4.14) and was plotted against the force sensor data in Figure 4.5. As is apparent in the figure, the pneumatic actuators were outputting a larger torque than the sensor was reporting. The average value of this mismatch gave $\eta_{transmission} = 92\%$, which was reasonable as gear efficiencies are typically near 90%.

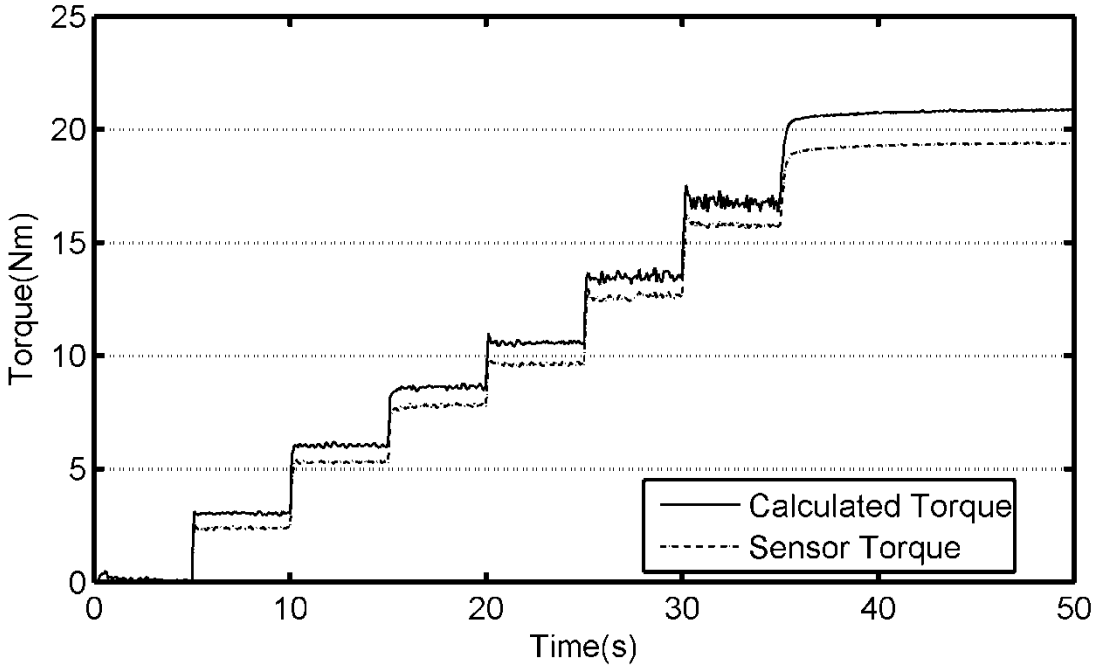

Figure 4.5 Plot of calculated torque and force sensor measured torque. 8% discrepancy, i.e. 92% torque transmission efficiency.

4.3 Pneumatic System Model

4.3.1 Pneumatic Cylinder Pressure Model

The pneumatic system modelling was more involved than that of the electric motor. Due to the pneumatic network configuration (recall Figure 3.11), and the choice of using only two, 3-way valves the chamber groups were either "open" or "closed". If "open", they were connected to the supply pressure via the accumulator. If "closed" they were connected to the atmosphere through a muffler. Using PWM these states can be rapidly changed to achieve different mass flow rates, positive and negative, on average over the longer PWM period.

It was assumed that the air temperature variation within the chambers is minimal. Further it was assumed that the air behaves as an ideal gas, and that the kinetic and gravitational effects on the air molecules are negligible in the

overall chamber. The basic equation which describes the behavior of each set of chambers was derived from that oft cited from Shearer (1956), and commonly used in the literature ever since (see Chapter 2). The relation (4.19) was derived from a combination of the ideal gas law, conservation of mass, and an energy balance of the system.

$$\dot{m}kRT = kP\dot{v} + v\dot{P} \tag{4.19}$$

where $\dot{m}$ is the mass flow rate through the chamber group's valve, k is the ratio of specific heats for air (1.4), R is the universal gas constant (287 Pa m^3 K^{-1}), T is the air temperature (293 K), v is the chamber group volume, and P is the chamber group pressure.

Since the chamber is of a fixed diameter, the volume change can only be facilitated by motion of the cylinder piston. Thus, for the example of any generic pneumatic cylinder chamber (non-rod side):

$$v = y\pi\left(r_{piston}\right)^2 + v_{deadzone} \tag{4.20}$$

where y is current chamber length, depending on piston position, and $v_{deadzone}$ is the deadzone volume. For the purposes of the hybrid, this can be expressed in the rotary sense. The conversion from angular position 0° (as in Figure 4.6) to cylinder's physical 0 volume point must be accounted for by an offset, θ_{offset}. Furthermore, a certain baseline volume, $v_{deadzone}$, always exists (due to fittings, seal, *etc*) in the chamber group and must be considered. This deadzone volume is a sum of the volume in the pneumatic lines between the cylinders and the valves, as well as the volume of the chamber that remains even when the position is at "0".

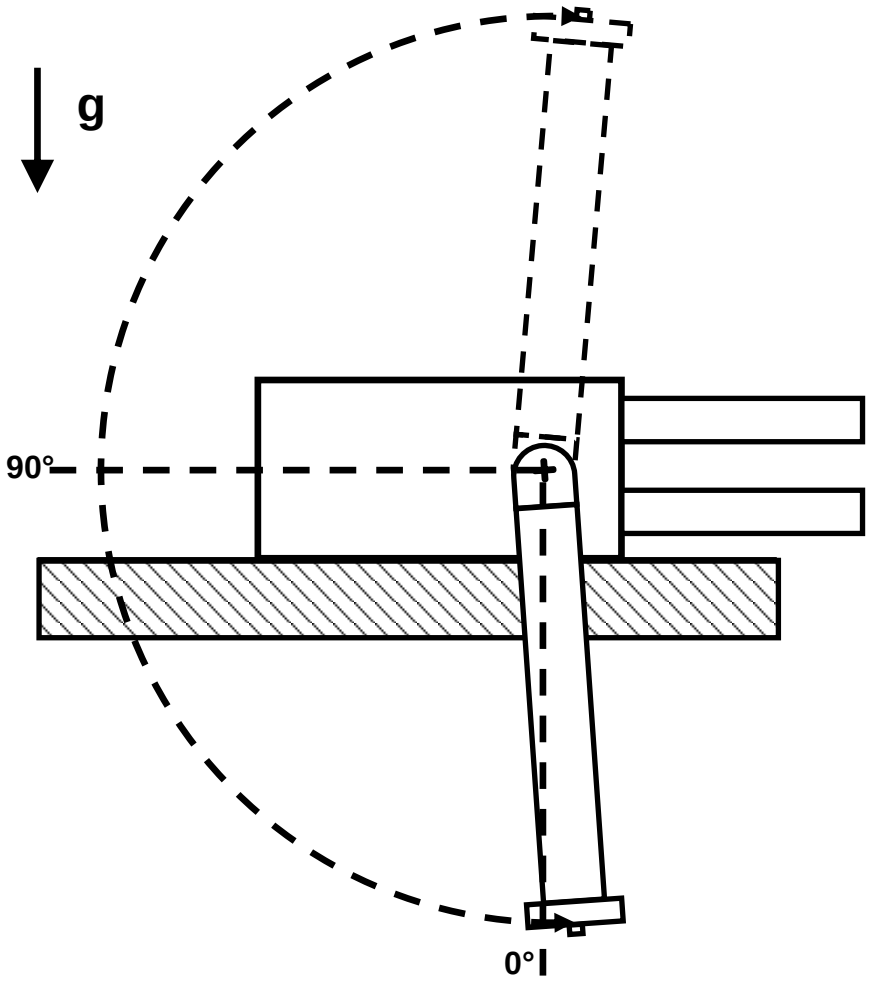

Figure 4.6 Range of motion of the link.

The relation between the linear positions (current chamber lengths): $y_{A,1}$, $y_{B,1}$, $y_{A,2}$, $y_{B,2}$ in each chamber and the system output angular position are defined by:

$$y_{A,1} = r_{gear}\left(\theta_{A,1offset} - \theta\right) \tag{4.21}$$

$$y_{B,1} = r_{gear}\left(\theta_{B,1offset} - \theta\right) \tag{4.22}$$

$$y_{A,2} = r_{gear}\left(\theta_{A,2offset} + \theta\right) \tag{4.23}$$

$$y_{B,2} = r_{gear}\left(\theta_{B,2offset} + \theta\right) \tag{4.24}$$

Thus the volumes expressed for the chambers and deadzone becomes:

$$v_{A,1} = \left(\theta_{A,1offset} - \theta\right) r_{gear} \pi \left(r_{piston}\right)^2 \tag{4.25}$$

$$v_{B,1} = \left(\theta_{B,1offset} - \theta\right) r_{gear} \pi \left(\left(r_{piston}\right)^2 - \left(r_{rod}\right)^2\right) \tag{4.26}$$

$$v_{1,deadzone} = 2v_{1,Adeadzone} + 2v_{1,Bdeadzone} + v_{1,tubing} \tag{4.27}$$

Collected for group 1's total volume as:

$$v_1 = 2v_{A,1} + 2v_{B,1} + v_{1,deadzone} \tag{4.28}$$

Similarly for group 2's elements:

$$v_{A,2} = \left(\theta_{A,2offset} + \theta\right) r_{gear} \pi \left(r_{piston}\right)^2 \tag{4.29}$$

$$v_{B,2} = \left(\theta_{B,2offset} + \theta\right) r_{gear} \pi \left(\left(r_{piston}\right)^2 - \left(r_{rod}\right)^2\right) \tag{4.30}$$

$$v_{2,deadzone} = 2v_{2,Adeadzone} + 2v_{2,Bdeadzone} + v_{2,tubing} \tag{4.31}$$

Collected for group 2's total volume as:

$$v_2 = 2v_{A,2} + 2v_{B,2} + v_{2,deadzone} \tag{4.32}$$

The collected group volumes were slightly different due to minor differences in deadzone volumes. The cylinder strokes were coupled to the pinion gear such that each cylinder is at approximately the middle of its stroke at about 50% of the rotary range of motion, 90°. The top and bottom cylinders could not be placed exactly evenly, due to the nature of the gearing's discrete meshing points. The cross section of the cylinder interior is shown in Figure 4.7, with the interior deadzone shown. The deadzones and offsets are summarized in Table 4.2.

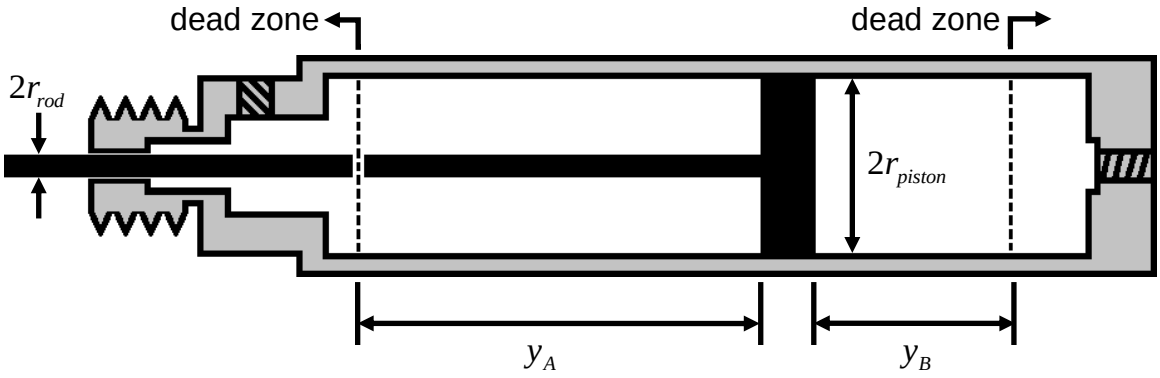

Figure 4.7 Diagrammatic cross-section of the pneumatic cylinders used.

Table 4.2 Chamber deadzones and offsets.

Group: Chamber/Component	Deadzone (m^3)	Offset (m)
1:A	1.131×10^{-6}	0.1175
1:B	2.100×10^{-6}	0.0916
1:Tubing	9.425×10^{-6}	-
1:Total	1.589×10^{-5}	-
2:A	2.262×10^{-6}	0.0290
2:B	1.490×10^{-6}	0.0070
2:Tubing	9.048×10^{-6}	-
2:Total	1.655×10^{-5}	-

Similarly the rates of change in volume, $\dot{v}_1$ and $\dot{v}_2$, can be expressed as:

$$\begin{aligned}\dot{v}_1 &= 2\dot{v}_{A,1} + 2\dot{v}_{B,1} \\ &= 2\left(-\dot{\theta} r_{gear} \pi \left(r_{piston}\right)^2\right) + 2\left(-\dot{\theta} r_{gear} \pi \left(\left(r_{piston}\right)^2 - \left(r_{rod}\right)^2\right)\right) \\ &= -2\dot{\theta} r_{gear} \pi \left(2\left(r_{piston}\right)^2 - \left(r_{rod}\right)^2\right)\end{aligned} \tag{4.33}$$

$$\begin{aligned}\dot{v}_2 &= 2\dot{v}_{A,2} + 2\dot{v}_{B,2} \\ &= 2\dot{\theta} r_{gear} \pi \left(r_{piston}\right)^2 + 2\left(\dot{\theta} r_{gear} \pi \left(\left(r_{piston}\right)^2 - \left(r_{rod}\right)^2\right)\right) \\ &= 2\dot{\theta} r_{gear} \pi \left(2\left(r_{piston}\right)^2 - \left(r_{rod}\right)^2\right)\end{aligned} \tag{4.34}$$

Combining (4.19), (4.28)/(4.32), and (4.33)/(4.34), the final mass flow rate equations can be expressed as:

$$\dot{m}_1 = \frac{-2P_1\dot{\theta}r_{gear}\pi\left(2\left(r_{piston}\right)^2-\left(r_{rod}\right)^2\right)}{RT}+ \frac{\left(2\pi r_{gear}\left(\left(\theta_{A,1offset}-\theta\right)\left(r_{piston}\right)^2+\left(\theta_{B,1offset}-\theta\right)\left(\left(r_{piston}\right)^2-\left(r_{rod}\right)^2\right)\right)+v_{2,deadzone}\right)\dot{P}_1}{kRT} \quad (4.35)$$

and

$$\dot{m}_2 = \frac{2P_2\dot{\theta}r_{gear}\pi\left(2\left(r_{piston}\right)^2-\left(r_{rod}\right)^2\right)}{RT}+ \frac{\left(2\pi r_{gear}\left(\left(\theta_{A,2offset}+\theta\right)\left(r_{piston}\right)^2+\left(\theta_{B,2offset}+\theta\right)\left(\left(r_{piston}\right)^2-\left(r_{rod}\right)^2\right)\right)+v_{2,deadzone}\right)\dot{P}_2}{kRT} \quad (4.36)$$

where $\dot{m}_1$ is the mass flow rate for chamber group 1 and $\dot{m}_2$ is the mass flow rate for chamber group 2.

4.3.2 Valve Modelling

Due to the complexities and nonlinear dynamics of the solenoid valves, especially under the small time scales which must be considered for PWM control, a black box approach was taken. The black box model was implemented through the use of a multi-layer perceptron ANN. The ANN is an inverse model of the solenoid valve, where the output of the ANN is the input of the actual valve. The desired ANN output, for a single valve, was the appropriate PWM control signal which will achieve the desired mass flow rate, given current system pressures.

Non-blackbox valve models based upon the orifice flow equation relate the pressures on either side of the valve, and empirical/geometric coefficients to a mass flow rate through said valve (ee Chapter 2 for details). For example, Shearer (1956) developed the following relation:

$$\dot{m} = \frac{1.08 C_{ds} \omega_s U P_s}{\sqrt{T_c}} \left[\left(1 + \frac{X}{U} \right) f_1 \left(\frac{P_a}{P_s} \right) - \left(1 - \frac{X}{U} \right) \frac{C_{dc} \omega_c P_a}{C_{ds} \omega_s P_s} \sqrt{\frac{T_s}{T_c}} f_1 \left(\frac{P_s}{P_a} \right) \right] \tag{4.37}$$

where U , X , ω_s , and ω_c are valve specific geometric constants or variables; C_{dc} , and C_{ds} are empirical flow coefficients; T_s and T_c are the supply and chamber temperatures; f_1 indicates a function of pressure ratio; P_a and P_s are the chamber and supply pressures respectively. If it is assumed the temperature does not change significantly between the supply and chamber, then the only remaining, variables are the chamber (valve upstream) and supply (valve downstream) pressures. Since Shearer was modelling a proportional valve, the geometric U/X ratio was related to the control signal, to vary the valve. In the case of the solenoid valves controlled with PWM, the control input becomes the PWM duty cycle, and any specific geometric effects are internalized to the ANN parameters.

The primary determining factors for calculating mass flow rate were: the pressure difference across the valve and one or more empirical constants. These values are all used in multiple valve models including: Shearer(1956), McDonell and Bowbrow (1993), Bone & Chen (2012), *etc*. As such the inputs selected for the ANN are the pressure state of the system and the mass flow rate. No empirical geometric coefficient is required, as any constants can simply be internalized to the black box model. Though this also means that the ANN applies specifically to the valve used, and would not behave the same if used with any randomly selected solenoid valve. Where separate equations are used for filling and discharging in the aforementioned models, the single ANN can characterize both cases.

The supply and atmospheric pressures, as well as the specific chamber pressure, and the desired mass flow rate would be the obvious choice for the ANN inputs. Yet this would require extensive training across a wide variation in

these all of these inputs and input combinations for the ANN to be effective. Since the model's development, validation and application are all performed at the same, constant, atmospheric and supply pressures, these values become a constant. As constants, their effects become intrinsic to the ANN, which then must be operated at the same supply and atmospheric pressure to maintain a good fit to the data. If a more flexible ANN was desired more extensive data collection would need to be performed, using a variety of supply pressures.

An additional set of pressure differences, besides the valve upstream/downstream pressures were important to the filling/discharging mass flow rate model. Filling refers to air flowing from supply, through the valve, and into a chamber, increasing the pressure in that chamber. Discharging refers to air leaving a chamber (and thus the pressure decreasing) through the valve, and to the atmosphere. To account for leakage across the piston seal and leakage across the rod seal, the additional set were the pressure difference between the *A* and *B* chambers, and the difference between the *B* chamber and the atmosphere. The chamber leakage could have been modeled separately from the valve, with an additional ANN, or alternate model. For this implementation all the leakage which affects a single valve/chamber group was lumped into a single ANN. As such, the additional input of the alternate chamber group pressure was included as an input to each valve's ANN model. Overall, the ANN used accounts for: the valve, the multiple grouped chamber volume pressure change, and the leakage of that chamber group. The ANN for valve 1 was the inverse valve model (IVM1) for valve 1 which characterized its behaviour. Likewise valve 2's ANN was its inverse valve model (IVM2). Figure 4.8 shows the ANN as it fits into the overall control system structure, as will be further discussed in Chapter 5.

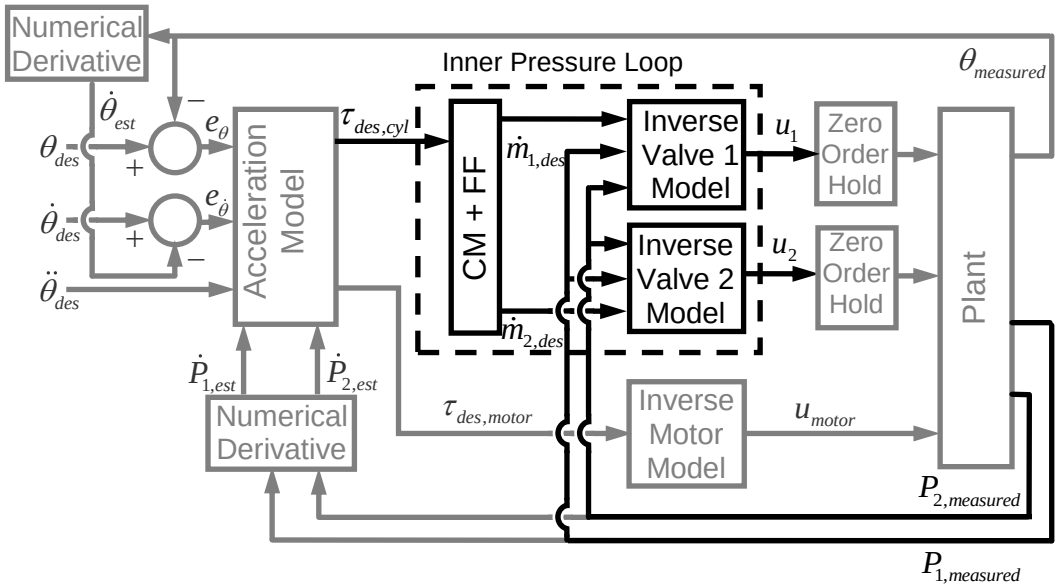

Figure 4.8 Inverse valve models (IVM1 and IVM2), containing the ANNs of each valve, and their incorporation into the overall controller. CM+FL refers to the combination of the cylinder model and feedback linearization as discussed in Chapter 5 along with the remainder of the figure.

The basic structure of the ANN is shown in Figure 4.9. Three types of layers of neurons exist, the input layer, two hidden layers, and an output layer. For the inverse valve model the input layer had 3 input neurons each of which correspond to one of: mass flow rate desired for that valve/chamber group, pressure in chamber group 1, pressure in chamber group 2. The number of neurons in each of the hidden layers, and the number of hidden layers used were solved during the ANN training which is further explained later in this subsection. The final layer has a single neuron which represents the output, the valve PWM duty cycle appropriate to achieve the desired mass flow rate.

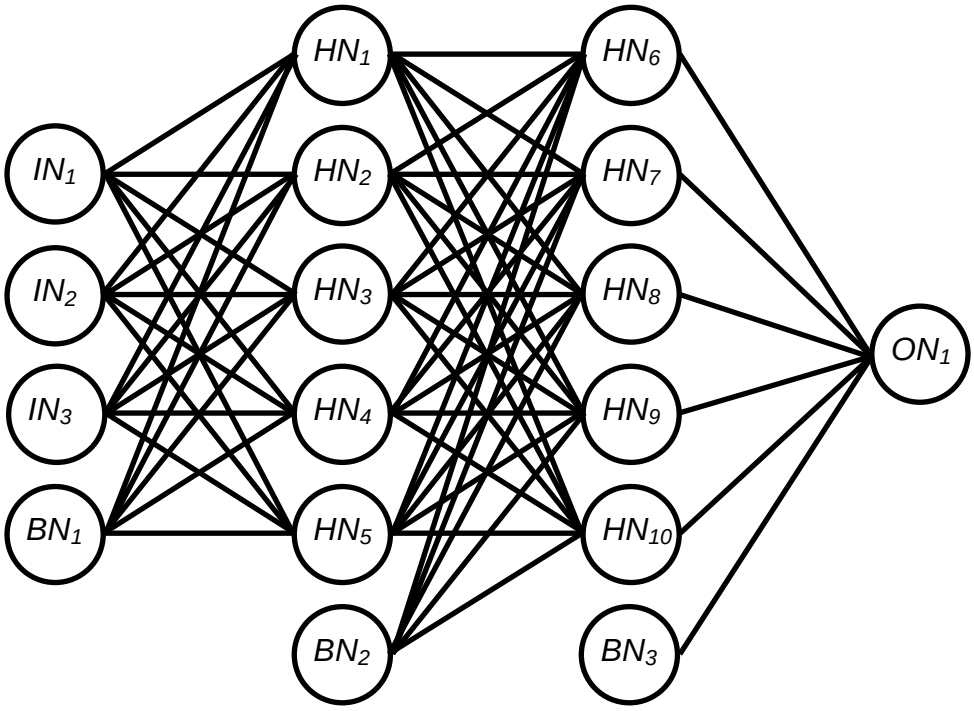

Figure 4.9 An example of an ANN structure for the inverse valve model. Input layer contains 3 input neurons and 1 bias neuron. The two hidden layers each contain 5 hidden neurons and 1 bias neuron. The output layer contains 1 output neuron.

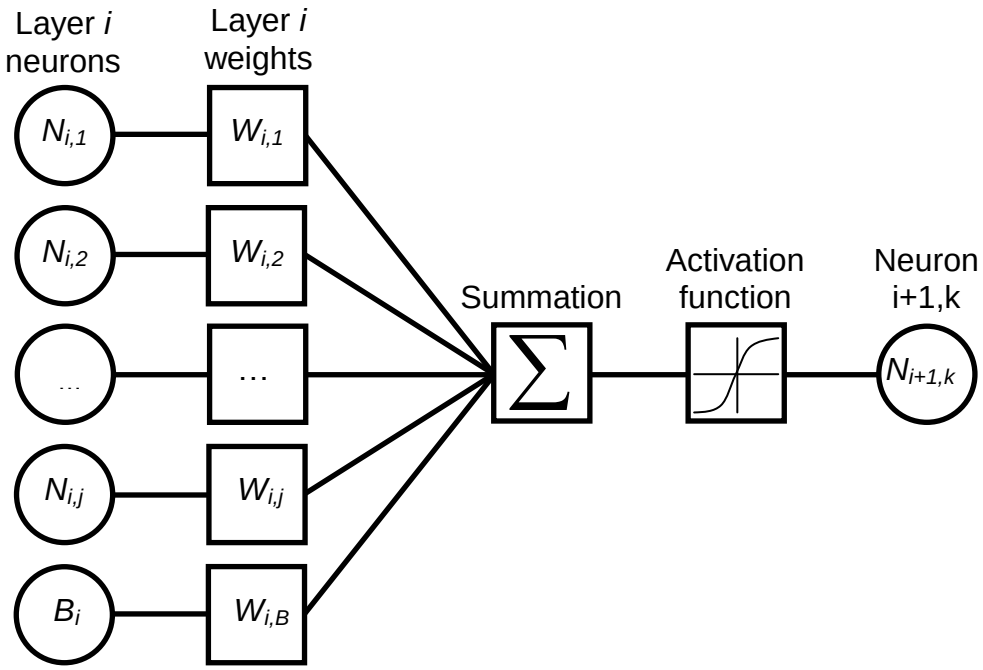

Figure 4.10 Example of a single neuron, number *k* in layer *i*+1, and its value derivation. The previous layer *i* has *j* neurons (with values, input or calculated from layer *i*-1), and one bias neuron. Neuron values are multiplied by their weights and summed. This summation is the input to the activation function and the output is the value of the neuron in question, neuron *k* of layer *i*+1.

Each neuron (save for bias neurons) is connected to every other neuron in the next, adjacent layer, as can be seen in Figure 4.10. A neuron value in the input layer is simply the input value of the variable assigned. The value of a neuron in the hidden or output layer is determined by the combination of values of all the connected neurons on the previous layers, their connection weights, and that neuron's activation function. Figure 4.10 illustrates how the value of an arbitrary neuron number *k* in an arbitrary layer *i+1* is determined, based on the values of the previous layer *i* and the neurons therein. The value of every neuron in the previous layer that is connected to $N_{i,k}$ is multiplied by the weight of that neuron to neuron connection. The values multiplied by the weights of every connected neuron are summed. This summed value is then passed as the input into an "activation function" which outputs a modified value of the input sum. The

output of the activation function then becomes the value of the neuron $N_{i,k}$ which is then used to calculate values of neurons in subsequent layers. The standard, nonlinear, sigmoid-symmetric activation function is used for this ANN. Thus every neuron has a value calculated from previous neurons, and a different weight for every neuron to which it connects. The neuron values change with every input, and in this way calculate the output value. For the specific type of ANN used (non-learning) the weights and biases remain constant after they are determined. The specific values of these weights were determined when the ANN is "trained", that is to say fit to a representative data set. Each layer also contained a bias neuron. Bias neurons are typically included in all layers that connect forward to additional layer; they do not connect to any neurons in the previous layer. The bias neuron always has the value of 1, and the weight of each connection is tuned like any other neuron connection weight during training. This allows the bias to effectively "shift" the activation function of any forward neuron it is connected to, where the non-bias neurons can only scale along the activation function. The number of neurons, and layers were determined during training, when the weights and biases are established.

To establish the relationship between the inputs and output the ANN must be trained by attempting to optimize the neuron connection weights and biases to produces minimal error in estimation of the dataset. Typically the more complete the training data is, in terms of the total possible input/output ranges and combinations possible in the actual system, the better the ANN will perform in practice. Capturing a large and complete amount of data can be difficult and time consuming. Furthermore a larger dataset would also require longer training times. Therefore a representative, though not exhaustive, cross section of the data was collected and evaluated. Depending on the number of inputs and degree of coupling between the variables, the amount of unique test combinations could still quickly become extremely large.

In order to collect and characterize appropriate data for each valve, the PWM duty cycle was stepped through its full 0-100% range at a fixed interval for the valve being modelled, while the valve for the other group was simultaneously given a pseudo-random duty-cycle. The pseudo-random input was generated by creating random noise in a fixed range, low-pass filtering it to lower the frequency of variation, and finally scaling it to the appropriate expected range, *i.e.* 0-100% duty cycle. The filtering is required as the cylinder model contains time dependent variables, as such the rate in change of cylinder pressure has physical rate of change limitations and would not respond as rapidly as the random noise originally generated. The filtering provided a slower, more continuous random duty cycle. The chamber group pressures and encoder position sensor data was monitored throughout the training data collection. The rate of change in position and pressure was calculated by backwards differencing, and filtered (further discussed in Chapter 5.). Finally using (4.35) and (4.36), the mass flow rates into or out of each chamber group can be calculated. The combination of stepped through duty cycle for the valve being characterized, and pseudo-random for the other, ensures that the full range of duty cycles are represented, with a good variation in pressures, and mass flow rate. The position was monitored despite the system being clamped during the data collection, in case deflections in the link cause small changes in chamber volume. The motion/change in volume observed was minimal, and likely had little appreciable influence on the ANN model.

The data was collected from the fully assembled GEN2 actuator, not an isolated sub-component, and as such, some limitations were imposed. The output link of the system was clamped at ~90°, effectively preventing any gross motion of the system or volume change in the cylinders. ~90° corresponds to ~50% of the cylinder strokes, such that the chambers are all of approximately equal volume. Without clamping the link, the random inputs could have easily caused damage in the system via high speed/torque impact at a joint limit.

Furthermore if the link moved, or was not supported by the clamp, the particular loads (*i.e.* gravity) introduced could skew the tuning towards a particular loading condition of the system.

The same data collection experiment was repeated five times for each valve to generate a large number of input/output pairs over the range of the data. The ten trials were merged into two training datasets, one for each valve. The remainder of the ANN development will focus on the modelling of only Valve 1, for brevity. The same procedures were followed for valve/group 2, simply with the u_1 and u_2 roles reversed. Figure 4.11 shows typical data collected for a single data collection experiment. Note that the third ANN input, $\dot{m}$, is not plotted. Valve 1 is given a stair input to evenly cover the possible input range of 0-100%. Valve 2 is given the pseudo-random input, in an attempt to capture a wide range of P_2 as possible while P_1 more smoothly varies from atmospheric to supply each step. The pressures are plotted to show the range and variation in the random valve 2/group 2, as well as the response of the valve 1/group 1. Two regions can be observed, the first being ~0 to ~130 seconds where the duty cycle stairs are rising, and the second where the stairs are falling.

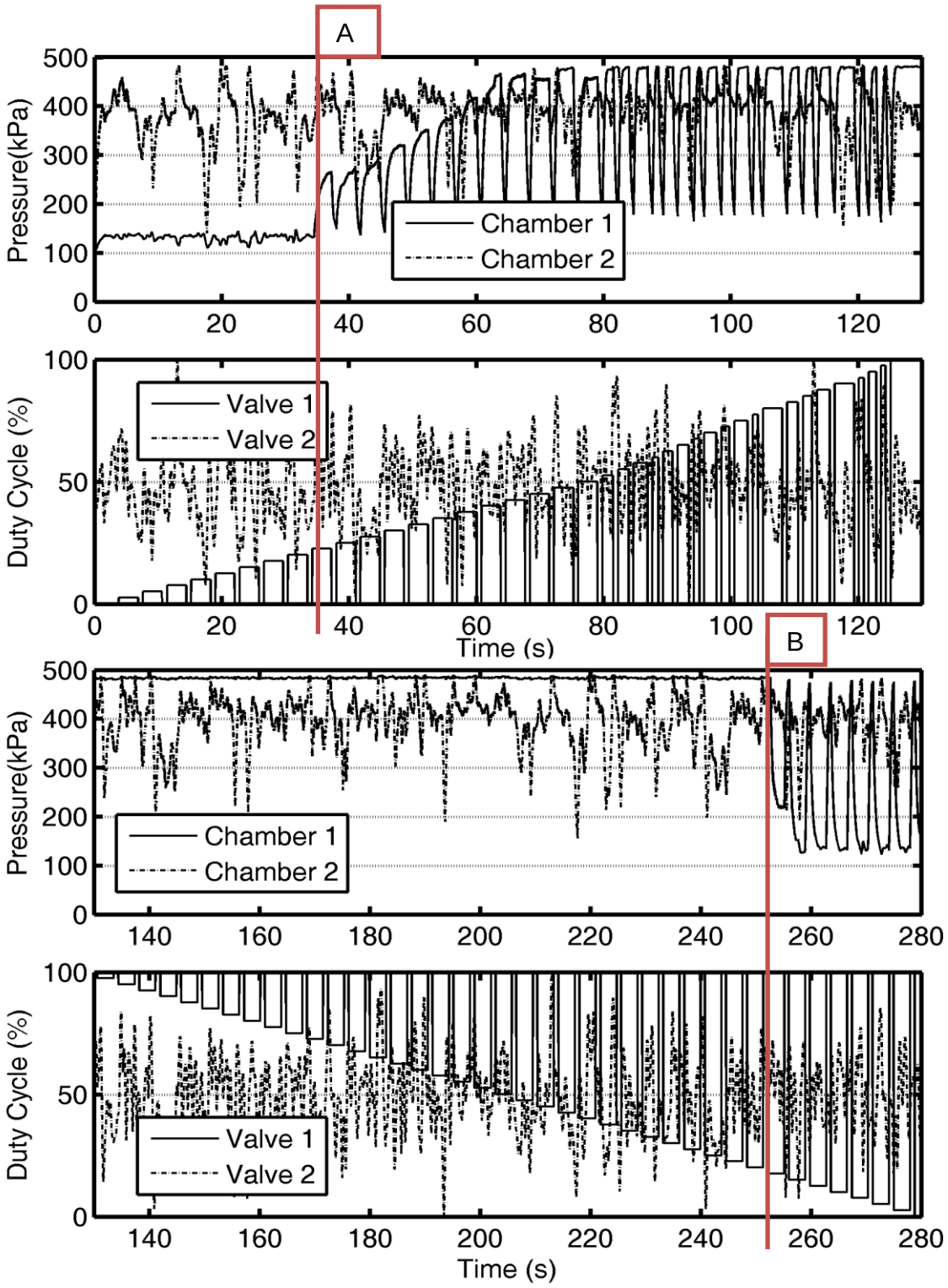

Figure 4.11 Example of training data collection. A: Minimum valve DC% for positive mass flow. B: Minimum valve DC% for negative mass flow.

In the first region the desired step increase of the duty cycle was applied for either a set maximum time period, or until the supply pressure is reached in that chamber group. Between each step increase, the duty cycle was returned to 0% for a set time period. This allowed the chamber group to discharge back to a lower pressure, before applying the next step where the pressure would rise. The intent was to collect a variety of data across the range of P_1, (with P_2 randomly varying). If this condition was not included, the chamber would sit at a large pressure for most of the test, thus missing valuable characterization data and skewing the ANN. The steps were not necessarily the same width, as once the chamber group reaches maximum pressure, it would be collecting redundant data, which might skew the network. The maximum pressure check is added so that the varying pressure data is given equal effect on the training, by merit of its percentage of the dataset. The duration of each step decreases as the duty cycle increases, since the filling speed and thus pressure rate of change speed increases.

In the second region, a similar process occurs, but between each step the duty cycle is set to 100%, to allow the chamber group to be fully pressurized to supply before each decrease in duty cycle. The first region primarily represents the chamber filling data and the second primarily represents the discharging data.

It can be observed from Figure 4.11 (A marker) that to cause a positive change in the chamber pressurize a certain minimum duty cycle must be exceeded, and the duty cycle drop below a maximum before discharging of the chamber occurs (Figure 4.11, B marker). Recall section 3.5.2 where the valve dynamics are discussed. The selection of the PWM period, as well as the valve/cylinder dynamics, influences at which duty cycle percentages the valve response limits occur. The shorter the PWM period, the smaller the effective duty cycle range, but the quicker the duty cycle can be changed to respond to system conditions. Figure 4.11 does not immediately indicate if the mass flow rate is

saturated for filling after a certain duty cycle, though the macroscopic pressure change is some indication for the minimum for positive mass flow, and the maximum for negative mass flow.

After data collection, the data is pre-processed before training. In the data collection, values were measured every 1 ms (1 kHz), but recall that the PWM period of the valves is 8 ms, meaning that the duty cycle could only be changed at a rate of 125 Hz. The faster data collection rate allows for less $\dot{P}$ and $\dot{\theta}$ phase lag, and in turn more current $\dot{m}$ estimation. As such the mass flow rate was calculated at the full 1 kHz, but the training data was the subset that uses only every 8th point. Once the ANN was implemented, the sensor data available at the start of a PWM period was used to select the duty cycle appropriate to produce the desired mass flow rate, on average over the 8 ms PWM period. For this reason, the training input/output data pairs were parsed as follows:

- P_1, P_2: Current sensor value at start of a PWM period
- $\dot{m}_1$ (or $\dot{m}_2$): average $\dot{m}$ over the full 8 ms period, *i.e.* average of 8 $\dot{m}$'s collected over the 8 data points of the PWM period.
- u_1 (or u_2): Duty cycle constant over entire period

The second stage of pre-processing was to eliminate large groups of data that fall in regions not useful for control. The training data was plotted as a 3D ($P_1, \dot{m}_1, u_1$) scatter plot and viewed on the mass flow/duty cycle plane as in Figure 4.12. Note that since the ANN actually has 3 inputs and 1 output, the 3D plot includes values across all P_2 pressures, as representing 4D in print is difficult. It can be seen that in general, the mass flow rates achieved do not change above 60%. This means that operating the valve above 60% has no change in the mass flow rate, as the maximum is achieved. Since operating about 60% is not useful for affecting control, the data collected in that region is redundant and will skew the fit of the ANN, by merit of more data points falling

within that region. As such, data where duty cycle exceeded 60% was trimmed from the dataset.

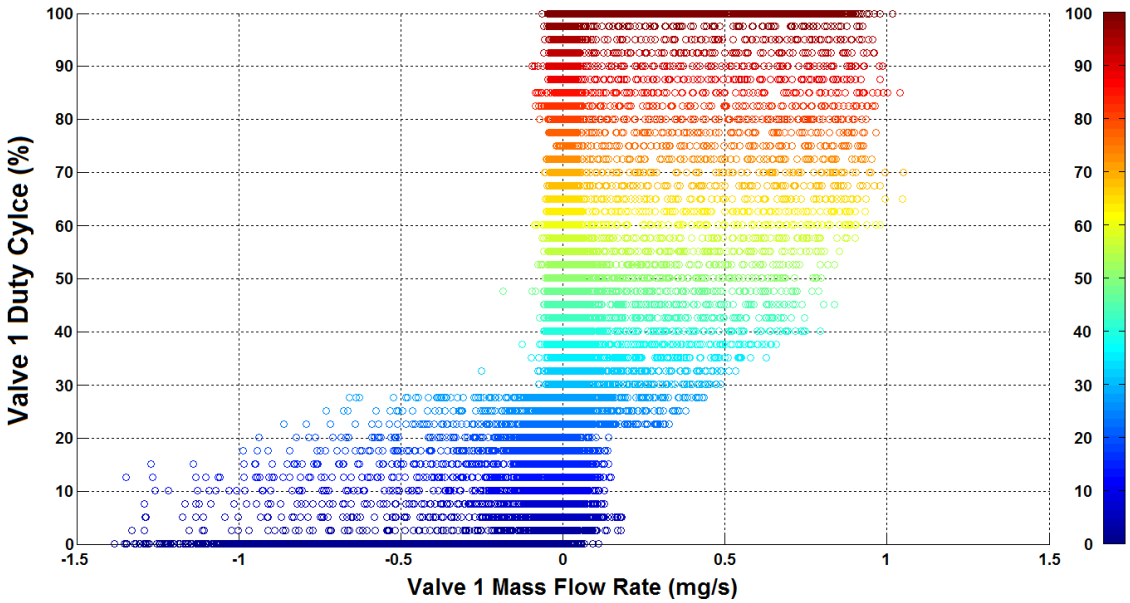

Figure 4.12 Duty cycle/mass flow rate relation, across all P_1 and P_2 pressures.

The next pre-processing stage was to remove large clusters of data that were observed at the minimum and maximum pressures, clustered at 0 mass flow rate, but distributed across the duty cycle range. This data was the redundant data that repeated across almost all duty cycles once the chambers reached atmospheric or supply pressure in discharging and filling respectively (as seen in Figure 4.12). These were deadzones in the system, where significant variation in the duty cycle led to ~0 mass flow rate. These deadzones were functions of both the dynamics of the valves, and the supply/atmospheric pressures. Though this data was representative of the behaviour of the system, it was a non-linearization which is not within a useful region of inputs in terms of controlling of the system. Due to the relative quantity of this repeated data, it would also skew the training of the overall ANN. It is desirable to have an ANN that fits better to the region which duty cycle can affect a mass flow response in the system. As opposed to an ANN which simply fits all of the collected dataset

as a whole. Data within these non-affecting regions is trimmed from the overall dataset before the ANN is trained.

In addition, a final layer of pre-processing was performed to normalize the data. Since the pressure data was on the order of 10^5 Pa, the mass flow rate was on the order of 10^{-5} kg/s, and the duty cycle in 10^1 %, all three types of data were normalized using their minimum/maximum values to a range of -1 to 1 or 0 to 1, as appropriate, so the inputs and outputs to the ANN were of the same magnitude. This ensures that the neuron values which interact with one another in the first layers have more even weighting at the beginning of the optimization of the connection weights. The variables have been rescaled for the purposes of plotting/interpretation, as in Figure 4.13. After trimming the data appropriately, the 3D scatter plot (again with all P_2 values plotted simultaneously) represents the data. This represents a 3D visualization of the data from all five trials of valve 1's training data. The training data was represented as points, whereas the ANN can be visualized of a series of 3D surfaces which vary with P_2. The four dimensional nature of the ANN input/output makes its representation by static 2D images very difficult.

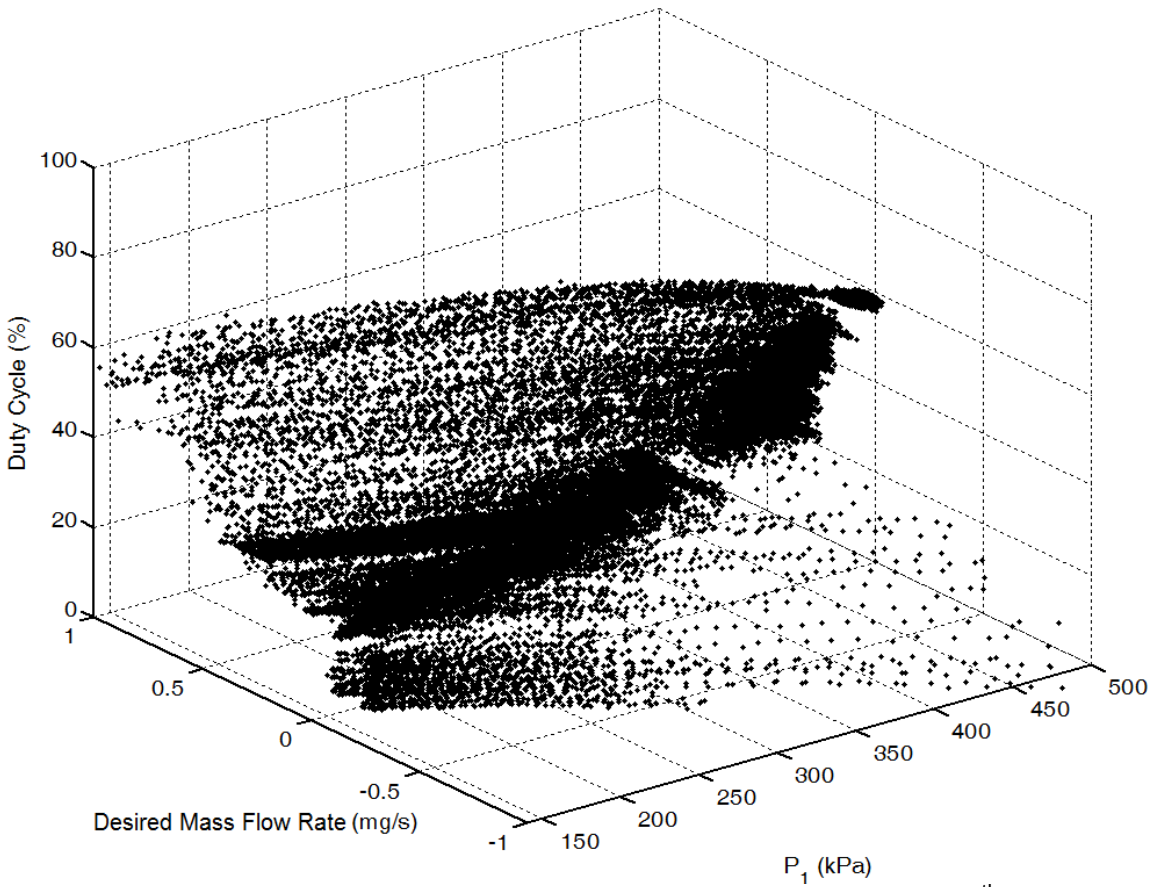

Figure 4.13 Pre-processed data for valve 1 training. Only every 5th point was plotted, for clarity.

The open source "Fast Artificial Neural Network" (FANN) library was used to build, train and implement the ANN within the C control code. A wide variety of ANN training algorithms exist, and can be implemented in the FANN framework. ANN training was essentially a standard optimization problem, and could be solved by a variety of algorithms. The optimization problem attempts to minimize the objective function L, the mean squared error between the output calculated by the ANN and from the original data as in:

$$L = \frac{\sum_{i=0}^{N_{points}} \left(u_1(t_i) - u_{1,INV}(t_i) \right)^2}{N_{points}} \tag{4.38}$$

$$u_{1,INV}(t_i) = INV_1\left(P_1(t_i), P_2(t_i), \dot{m}_1(t_i)\right) \tag{4.39}$$

where $u_1(t_i)$ is the duty cycle used at each sample (t_i) of the data collection, $u_{1,INV}(t_i)$ is the result of the ANN inverse model for each timestep, and INV_1 is the function of the ANN for the valve 1 inverse valve model. During training the ANN model was changed by varying the neuron weights and biases. The goal being to select the weights and biases which minimize this sum across the entire dataset. This was why trimming redundant data was important; the more points around one region, the more the final ANN would skew towards fitting that area.

A standard backpropagation method was used in FANN to attempt to minimize the objective function. Since this method can be susceptible to local minima, the training search was repeated 30 times to allow the search to proceed from different randomly generated starting points. This method has no guarantee of finding the global optimal solution, but multiple training attempts does provide more confidence in the solution that is found, than if only a single attempt was made. Each of the 30 optimization attempts was given maximum 2000 epochs (variations in weights/biases), and an error gradient cutoff of minimum 0.00001. The ANN weights were updated between epochs, and the entirety of the training data input/output pairs are evaluated within each epoch. This means that a specific ANN is given 2000 maximum attempts at parameter variation/optimization, but ends early if the change in error between epochs drops below a specified value.

During development a variety of network configurations were explored by varying the number of layers, neurons and the activation function type. Though by increasing layers, even a small number of neurons can increase the training time by a large time, due to the number of new connections introduced, and thus parameters to optimize. The parameters listed in Table 4.3 yielded good results at reasonable training times (approximately 5 minutes per training attempt on a

64-Bit Windows PC with an Intel i5 2400 3.1 GHz processor), and as such was selected as the final configuration. Using this structure, the entire training process was repeated 30 times, and the network which produced the lowest objective function result was the final ANN weights/biases selected.

Table 4.3 Training configuration for the ANNs of both inverse valve models.

Parameter	Value
Epochs Per ANN structure Training Attempt	2000
Activation Function	Sigmoid Symmetric
Convergence Cut off	0.00001
Overall ANN Training Attempts	30
Input Neurons(+Biases)	3+1
Hidden Neurons, Layer 1 (+Biases)	5+1
Hidden Neurons, Layer 2 (+Biases)	5+1
Output Neurons (+Biases)	1+0
Neuron Connections, Fully Connected	56
Number of Training Pairs (Valve 1/Group 1)	178,108
Number of Training Pairs (Valve 2/Group 2)	178,964

Separate data collection, pre-processing, and training was performed, in the same manner, to produce two separate ANNs, one for each of the valves/chamber groups. The training parameters used for both valves are listed in Tables 4.3. The network configuration is shown diagrammatically in Figure 4.9. Appendix B contains the final values of the weights and biases for both ANNs. The resulting ANNs, as previously mentioned, can be expressed for valve 1 as a series of 3D surfaces in (P_1, m_1, u_1) which vary with P_2 and for valve 2 as a series of 3D surfaces in (P_2, m_1, u_1) which vary with P_1. An example of a surface representing the ANN for Valve 1 at $P_2 = 310000kPa$ is shown in Figure 4.14 which can be compared to the raw data of Figure 4.13. The figure illustrates the

variability in mass flow rate across different chamber pressures and duty cycles. Particularly, with the middle range of duty cycle has the most varied topology. As the pressure and duty cycle reach the limits of their ranges the mass flow rate limits are reached and a flatter, less variable regions are seen at the extremes. The best trained networks that were retained had mean squared errors (see (4.38)) of: 0.0001017 % and 0.00000281 % for valve 1 and valve 2 duty cycle respectively.

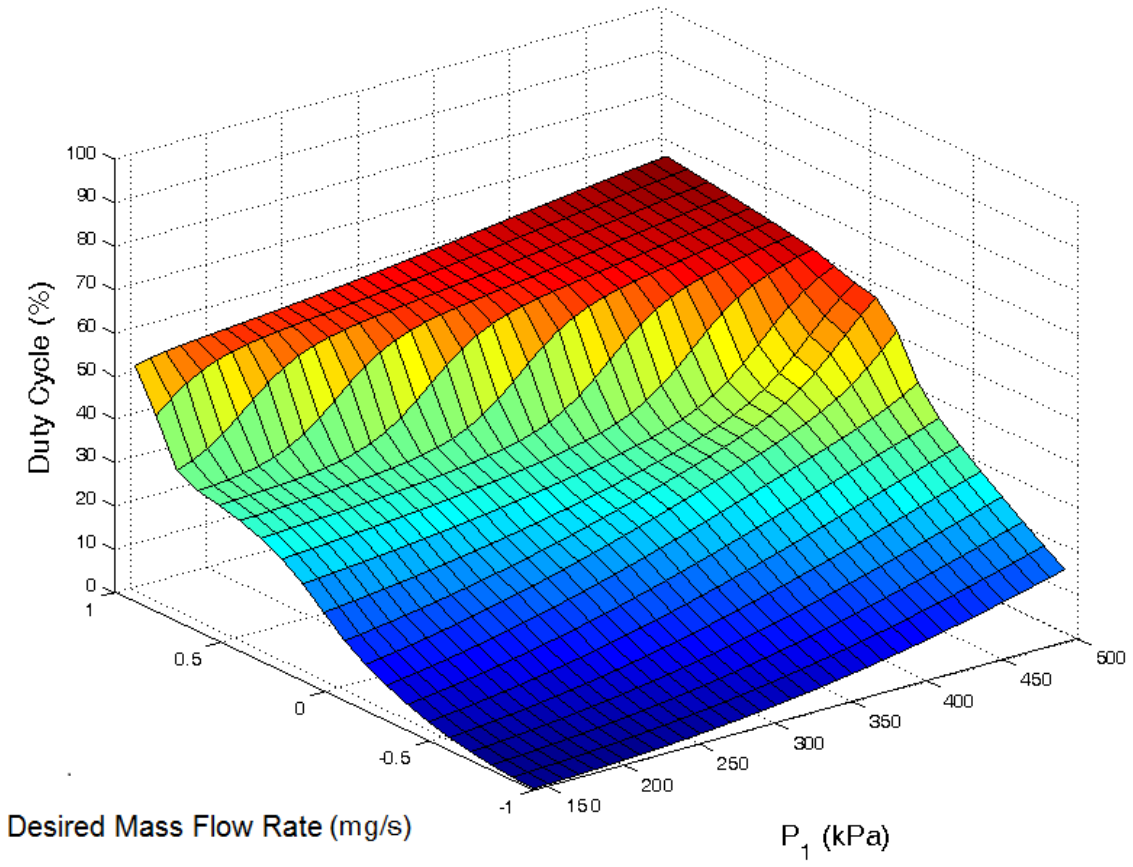

Figure 4.14 Example of the ANN surface for valve 1 at P_2=310 kPa.

4.4 Conclusions

The system was modeled as a single rotary inertia, lumped at the output shaft, and acted upon by a sum of torques as seen by the output shaft. The linear masses/forces from the cylinders and racks were converted to equivalent rotary inertias/torques as a function of the pinion gearing. The response of the motor was experimentally characterized to develop an appropriate input torque relationship. The cylinder model was presented and extended to the sum total of the two chamber groups, and related to the system rotary position. Finally black-box ANNs were developed as inverse models of the solenoid valves. The next chapter discusses the closed-loop control law developed for pressure, and ultimately position control.

Chapter 5 – Control Design

5.1 Introduction

This chapter presents the design of the controllers used with the GEN2 hybrid actuator. Each controller combined an inner pressure control loop with an outer position control loop. The outer position controller was based on the system acceleration model plus position and velocity feedback terms. Two pressure controllers were designed. The first was based on the cylinder model, the ANN-based inverse valve model (IVM) and pressure feedback. The second, alternate controller used pressure feedback, but did not make use of the IVM. The two controller types are tuned and their performance compared and further discussed in Chapter 6.

5.2 Control Overview

The overall system model and controller is shown diagrammatically in Figure 5.1. The mathematical models (blackbox or otherwise) of the system were the basis of the overall controller, with the addition of feedback from the encoder and pressure sensors.

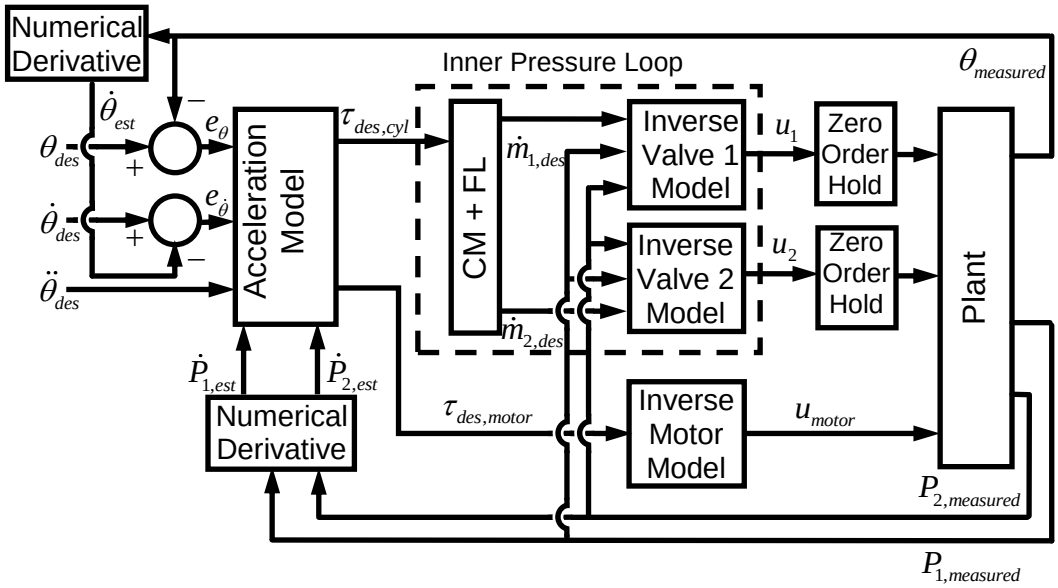

Figure 5.1: Overall control system block diagram. CM+FL refers to the combination of the cylinder model and feedback linearization.

The controller could only affect change in the pneumatics every 8 ms PWM period, as represented in Figure 5.1 by the zero-order hold (ZOH) blocks. The period was selected as described in Chapter 3. This means the pneumatic part of the controller effectively operated at 125 Hz. Yet, since portions of the model relied on time derivatives of sensor measured variables, high speed sensor sampling was desirable. Faster sampling allowed the numerical estimates of the time derivatives position and pressure to be computed with less phase lag. For this reason the controller was operated at 1 kHz and was limited to 125 Hz for the valve control signals using an 8 ms ZOH. The electric motor had no such limitation, and as such the motor control signal was updated every 1 ms sampling period.

5.3 ANN-Based Pressure Controller

Pneumatic actuators can be difficult to position control due to the magnitude of friction and its uncertainty; the compliance of air which underdamps the system with a tendency for oscillation; and the leakage of air at cylinder seals. The desired acceleration of cylinder piston/rod, and thus link position, may be achieved by imparting the appropriate net force on the piston. The force of each cylinder is a difference of the opposing pressures of the two chamber groups multiplied by the piston total area. Therefore maintaining appropriate pressures was fundamental in controlling the cylinder, and the hybrid actuator as a whole.

The pressure was primarily controlled through the combination of the IVM and the cylinder model. To account for modeling errors and to reject disturbances, feedback was added to the controller. Specifically, proportional and integral feedback terms were added to the desired mass flow rate calculation. The standard feedback linearization approach (Slotine & Li, 1991) was applied to linearize the pressure dynamics of each of the chambers. This then allowed the proportional and integral feedback to be more effective.

Rearranging (4.19), the pressure rate of change in a single chamber group can be expressed as:

$$\dot{P} = \frac{\dot{m}kRT - kP\dot{v}}{v} \tag{5.1}$$

which can be rearranged into the standard form:

$$\dot{P} = F\left(\theta, \dot{\theta}, P\right) + G\left(\theta\right)\dot{m} \tag{5.2}$$

Isolating the mass flow rate on the left hand side gives:

$$\dot{m} = \frac{\dot{P} - F\left(\theta, \dot{\theta}, P\right)}{G\left(\theta\right)} \tag{5.3}$$

The controller design begins by using (5.3) with the estimates for F and G, and setting $\dot{P} = u_p$, to obtain the following desired mass flow rate equation:

$$\dot{m}_{des} = \frac{u_p - \hat{F}\left(\hat{\theta}, \hat{\dot{\theta}}, \hat{P}_1, \hat{P}_2\right)}{\hat{G}\left(\hat{\theta}\right)} \tag{5.4}$$

where the "^" is used to indicate an estimate; either due to imperfect sensor data or due to the function having imperfect parameters and/or using imperfect sensor data. The estimates for F and G are:

$$\hat{F} = k\hat{P}\frac{\hat{\dot{v}}}{\hat{v}} \text{ and} \tag{5.5}$$

$$\hat{G} = kR\hat{T}\frac{1}{\hat{v}} \tag{5.6}$$

where $\hat{v}$ is the chamber group volume estimate; and $\hat{\dot{v}}$ is the chamber group volume rate of change estimate. Assuming $\hat{F} = F$, $\hat{G} = G$ and the IVM works perfectly such that $\dot{m} = \dot{m}_{des}$ then setting $u_p = \dot{P}_{des}$ would result in $P = P_{des}$. Of course those assumptions are unrealistic so it is necessary to add proportional and integral feedback as follows:

$$u_p(t) = \dot{P}_{des}(t) + K_{P,pressure}\left(P_{des}(t) - P(t)\right) + K_{I,pressure}\int\left(P_{des}(t) - P(t)\right)dt \tag{5.7}$$

where $K_{P,pressure}$ and $K_{I,pressure}$ are the proportional and the integral gains respectively; P_{des} is the desired pressure coming from the position controller; and t is the continuous time.

For implementation in discrete-time:

$$u_p(t_i) = \hat{\dot{P}}_{des}(t_i) + K_{P,pressure}\left(P_{des}(t_i) - P(t_i)\right) + K_{I,pressure}\left(\sum_{k=0}^{i} T_s\left(P_{des}(t_k) - P(t_k)\right)\right) \quad (5.8)$$

where i is the current sample number, t_i is the time of the current (i^{th}) sample and T_s is the sampling period. In (5.7) the rate of change of $P_{des}(t_i)$ is approximated by:

$$\hat{\dot{P}}_{des}(t_i) = \frac{P_{des}(t_i) - P_{des}(t_{i-1})}{T_s} \quad (5.9)$$

Finally combining (5.4)- (5.6), and(5.8), and rearranging gives:

$$\dot{m}_{des}(t_i) = \frac{\hat{v}(t_i)\left(\dot{P}_{des}(t_i) + K_{P,pressure}\left(P_{des}(t_i) - \hat{P}(t_i)\right)\right)}{kR\hat{T}} + \frac{K_{I,pressure}\left(\sum_{k=0}^{i} T_s\left(P_{des}(t_k) - \hat{P}(t_k)\right)\right) - k\hat{P}(t_i)\hat{\dot{v}}(t_i)}{kR\hat{T}} \quad (5.10)$$

When this equation is used for chamber group 1: (4.28) is used with $\hat{\theta}(t_i)$ to calculate $\hat{v}_1(t_i)$, and (4.33) is used with $\hat{\dot{\theta}}(t_i)$ to calculate $\hat{\dot{v}}_1(t_i)$. For group 2, (4.32) and (4.34) are used in a similar manner to calculate $\hat{v}_2(t_i)$ and $\hat{\dot{v}}_2(t_i)$. The angular velocity estimate, $\hat{\dot{\theta}}(t_i)$, was estimated via the numerical time derivative of the encoder position data, and low-pass filtered to mitigate the quantization noise, via:

$$\hat{\dot{\theta}}(t_i) = \lambda_{\dot{\theta}}\hat{\dot{\theta}}(t_{i-1}) + (1 - \lambda_{\dot{\theta}})\left(\frac{\hat{\theta}(t_i) - \hat{\theta}(t_{i-1})}{T_s}\right) \quad (5.11)$$

where $\lambda_{\dot{\theta}}$ is the angular velocity filter coefficient.

The proportional gain provided the main source of feedback for the rejection of disturbances and modelling errors. The integral term acted to eliminate steady state errors. The tuning of the pressure controller parameters is discussed in section 6.4.1. After $\dot{m}_{des}$ was established from (5.11), for the respective chamber group, the ANNs were then used to determine the appropriate valve duty cycles as follows:

$$u_1(t_i) = ANN_1\left(P_1(t_i), P_2(t_i), \dot{m}_{1,des}(t_i)\right) \quad \text{and} \tag{5.12}$$

$$u_2(t_i) = ANN_2\left(P_2(t_i), P_1(t_i), \dot{m}_{2,des}(t_i)\right) \tag{5.13}$$

where u_1 is the duty cycle to be applied to valve 1 and u_2 is the duty cycle to be applied to valve 2.

5.4 Alternate Pressure Controller

An alternate pressure controller was also developed. This allowed a comparison and contrast to be made, and an evaluation of the effectiveness of the IVM. The alternate controller developed used the same high level controller for position tracking, albeit with different parameter gains. The main difference in the alternate controller was the inner pressure control, which did not make use of the IVM. The alternate controller used deadzone compensation, proportional plus derivative plus feedforward action, and is shown in Figure 5.2. When using this alternate pressure controller, (5.10) through (5.13) of the ANN based controller were replaced with:

$$\begin{aligned} u_1(t_i) = u_{deadzone} &+ K_{P,pressure,alt}\left(P_{1,des}(t_i) - P_1(t_i)\right) - K_{D,pressure,alt}\hat{\dot{P}}_1(t_i) \\ &+ K_{FF,pressure,alt}\hat{\dot{P}}_{1,des}(t_i) \end{aligned} \quad \text{and} \tag{5.14}$$

$$u_2(t_i) = u_{deadzone} + K_{P,pressure,alt}\left(P_{2,des}(t_i) - \hat{P}_2(t_i)\right) - K_{D,pressure,alt}\hat{\dot{P}}_2(t_i) + K_{FF,pressure,alt}\hat{\dot{P}}_{2,des}(t_i) \quad (5.15)$$

where $K_{P,pressure,alt}$, $K_{D,pressure,alt}$, and $K_{FF,pressure,alt}$ are the proportional, velocity and feedforward gains respectively; $u_{deadzone}$ is the valve deadzone compensation value; and $\hat{\dot{P}}_1$ and $\hat{\dot{P}}_2$ are the estimated pressure rates of change for chamber groups 1 and 2 respectively. The pressure sensor data was software low-pass filtered when the time derivative was numerically estimated, similar to the angular velocity, using:

$$\hat{\dot{P}}(t_i) = \lambda_{\dot{P}}\hat{\dot{P}}(t_{i-1}) + (1-\lambda_{\dot{P}})\left(\frac{\hat{P}(t_i) - \hat{P}(t_{i-1})}{T_s}\right) \quad (5.16)$$

where $\lambda_{\dot{P}}$ is the pressure rate of change filter coefficient. While the hardware filter for the pressure sensors (discussed in Chapter 3) acted as the primary low-pass filter, the smoothing provided by this additional software filtering was found to be beneficial in the experiments.

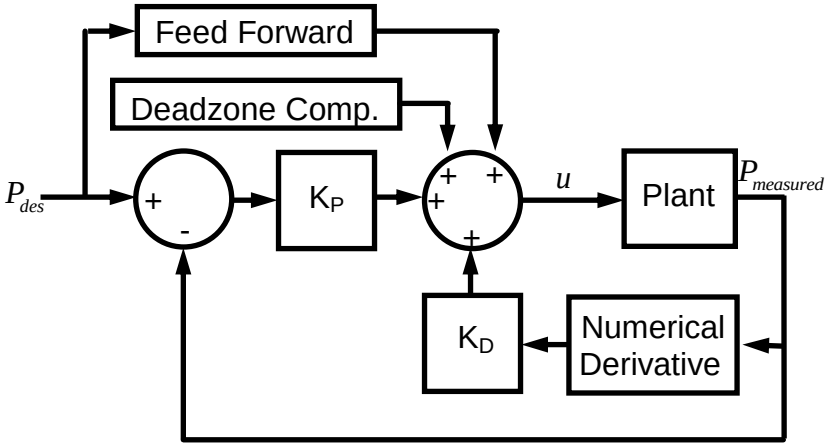

Figure 5.2: Block diagram of the alternate pressure controller. One was used for each chamber group.

5.5 Position Controller

5.5.1 Overview

Accurate position control of the hybrid actuator was the metric for evaluating the performance of the GEN2 system, as position control is the typical robotic operation. The position controller combines model-based compensation (including compensation of the inertial, gravity and friction torques); with an inner loop pressure controller (i.e., the ANN-based controller or the alternate controller); and sensor feedback.

5.5.2 Friction Compensation

The friction model was discussed in Chapter 4. As stated, during controller development the implementation of friction compensation was refined. As the friction compensation was affected by the realities of a discrete time control system, the influence of velocity estimation, and various friction regime regions could significantly affect overall system performance. The best performing implementation was ultimately based on a very simple friction model.

As discussed in Chapter 4, most friction models include viscous, dynamic and static components. The static to dynamic friction regime change typically involves a step change in friction value, as the static friction is larger than the dynamic. When there are small errors in position (as is desirable for a position controller), the controller tries to eliminate the errors by making small positive and negative torque changes, which result in positive and negative accelerations. Depending on the current velocity value and acceleration value, this can lead to rapid sign changes in velocity. When the position error is near zero, the sign change becomes an even more common occurrence than when a large SSE exists. If the estimated velocity is used in the compensator, the sign change introduces a desired torque step change due to the transition between a

positive/negative compensation value. When combined with estimated velocity sign changes due to sensor noise, oscillations can easily occur that degrade the performance of the position control. If the friction compensation is not dependent on estimated velocity it is less physically accurate, but control performance and not physical accuracy is the focus of this research. For these reasons, the chosen friction compensation was based on (4.12) with the desired velocity replacing the actual velocity. The steady-state performance was improved by adding an adjustment mechanism to the compensator. If the trajectory desired involved a move to a specific angle, and then dwelling at that angle, the desired velocity would then be zero. If a small SSE exists then the previous friction value can be retained. If the system has a larger SSE at that zero desired velocity, it must overcome friction to move and achieve zero SSE, and as such the compensation torque must be changed. If the SSE was over a certain threshold value, then each sample the friction compensation was increased to "push" the system towards zero SSE. Since the increase in friction compensation could be added to the previous values, it effectively acted as a type of integral action. The implemented version of the friction compensation can be expressed by:

$$
\begin{aligned}
&IF\left(\dot{\theta}_{des}\left(t_i\right)=0\right)\\
&\quad \tau_f\left(t_i\right)=\begin{cases}\tau_f\left(t_{i-1}\right)+\tau_{f+,offset} & \left(\theta_{des}\left(t_i\right)-\theta\left(t_i\right)\right)>\theta_{thresh}\\ \tau_f\left(t_{i-1}\right) & \left|\theta_{des}\left(t_i\right)-\theta\left(t_i\right)\right|\le\theta_{thresh}\\ \tau_f\left(t_{i-1}\right)+\tau_{f-,offset} & \left(\theta_{des}\left(t_i\right)-\theta\left(t_i\right)\right)<-\theta_{thresh}\end{cases}\\
&ELSE\\
&\quad \tau_f\left(t_i\right)=\begin{cases}\tau_{f+} & \dot{\theta}_{des}\left(t_i\right)>0\\ \tau_{f-} & \dot{\theta}_{des}\left(t_i\right)<0\end{cases}
\end{aligned}
\qquad (5.17)
$$

where $\tau_f\left(t_{i-1}\right)$ is the friction compensation from the previous sample and $\tau_f\left(t_i\right)$ is the friction compensation for the current sample. θ_{thresh}=0.001 rad was the threshold around zero used to account for noise. The tuning of the friction parameters is further discussed in section 6.4.2.

5.5.3 Pneumatic Mode

The position controller must provide the torque needed for acceleration; for overcoming gravity and friction; and for rejecting disturbances. This led to the following equation for the desired torque for the pneumatic actuator:

$$\tau_{pneum,des}(t_i) = \ddot{\theta}_{des}(t_i)\hat{J}_{system} + \hat{\tau}_{grav}(t_i) + \hat{\tau}_f(t_i) + K_{P,\theta}\left(\theta_{des}(t_i) - \hat{\theta}(t_i)\right) + K_{D,\theta}\left(\dot{\theta}_{des}(t_i) - \hat{\dot{\theta}}(t_i)\right) \quad (5.18)$$

where $\theta_{des}(t_i)$, $\dot{\theta}_{des}(t_i)$ and $\ddot{\theta}_{des}(t_i)$ are the desired position, velocity and acceleration for the current sample, respectively; and $K_{P,\theta}$ and $K_{D,\theta}$ are the proportional and derivative gains respectively. The first two terms in (5.18) are based on the system model and the estimates of its parameters. The gravity compensation torque, $\hat{\tau}_{grav}(t_i)$, also uses the sensed position. The fourth term, the friction compensation, was described in the previous section. The proportional and derivative feedback terms compensate for modelling errors and reject disturbances.

It remains to convert the desired torque to the desired pressure for each chamber group. Based on (4.18), the pressure difference, $P_2 - P_1$, required of the pneumatic cylinders is:

$$P_{difference,des} = \frac{\tau_{pneum,des}(t_i)}{\eta_{transmission} r_{gear} A_{pneum}} \quad (5.19)$$

Since the pneumatic torque desired was provided by a difference in pressures, as in (5.19), multiple solutions existed for the individual pressures. That is to say a single torque value could be achieved multiple ways by increasing P_2 while also increasing P_1 appropriately, or by decreasing both.

$P_{difference,des}$ was selected to be centered about the midpoint between supply and atmospheric pressure. This arrangement served several purposes. First, maintaining the chamber pressures around the midpoint of available pressures allowed the most flexibility to increase or decrease the pressure to any desired within the range. Secondly with a larger chamber pressure results in more pneumatic stiffness in the system, improving the controllability of the actuator. As such, the system gained some stiffness, while simultaneously maintaining both pressures away from the limits, except when required. The system speed of response was also favorably affected by this arrangement. Take for the example, a different arrangement where the difference in pressures is provided by keeping one chamber at atmospheric. If a torque increase was desired, one chamber group pressure would have to increase to the value of the pressure difference desired, while the other chamber group maintained atmospheric. This means the entirety of the mass flow to increase the pressure must go through one valve into one chamber group. Compare this to the scheme used where both chamber groups were near the midpoint pressure. Then if a torque increase is requested, the difference in pressure can be achieved by increasing the pressure in one while simultaneously decreasing the pressure in the other. Splitting the mass flow task between the two chamber groups/valves was less likely to hit a mass flow rate/pressure rate change limit, thus allowing for the difference in pressure to be achieved as quickly as possible. Thus $P_{1,des}$ and $P_{2,des}$ were defined by:

$$P_{1,des}\left(t_i\right)=\left(P_{supply}-P_{atm}\right)-\tfrac{1}{2}P_{difference,des}\left(t_i\right) \quad \text{and} \tag{5.20}$$

$$P_{2,des}\left(t_i\right)=\left(P_{supply}-P_{atm}\right)+\tfrac{1}{2}P_{difference,des}\left(t_i\right) \tag{5.21}$$

After the desired pressures were calculated the pressure controller was used to get the appropriate control signal value to send to the solenoid valves.

The desired trajectory was pre-computed before each move or series of moves to generate the appropriate position (θ_{des}), velocity ($\dot{\theta}_{des}$), and acceleration ($\ddot{\theta}_{des}$) points for every sampling instant. The trajectory points were those required to move from the current position to the target position. The exact profile between the current position and target could be anything, and in many cases is dependent on the application. For the purposes of this research a smooth cycloidal trajectory was used, and is further discussed in Chapter 6.

5.5.4 Hybrid Mode

The GEN2 actuator is capable of acting in the pneumatic mode, where the control is entirely provided by the pneumatic actuators, or in the hybrid mode, where the electric motor also contributes to the control. When operating in hybrid mode, since the motor was quick to respond but low in torque capacity, and the pneumatic actuator was slower to respond but high in torque capacity they could be made to work in a complementary fashion. The desired motor torque was set to:

$$\tau_{motor,des}(t_i) = K_{P,motor}\left(\theta_{des}(t_i) - \hat{\theta}(t_i)\right) + K_{D,motor}\left(\dot{\theta}_{des}(t_i) - \hat{\dot{\theta}}(t_i)\right) \qquad (5.22)$$

where $K_{P,motor}$ is the motor proportional gain, and $K_{D,motor}$ is the motor derivative gain. In (5.22) the inertial, gravity and friction torque compensation terms were deliberately left out since they were already included in $\tau_{pneum,des}$. Their total torque is large and slowly varying so providing it with the pneumatic actuator was the logical choice. The proportional and derivative feedback terms are in (5.22) since the motor's quick response will help the hybrid actuator to compensate for higher frequency modelling errors and disturbances.

The motor command signal is obtained from (5.22) using the inverse motor model from (4.17) as follows:

$$u_{motor} = 0.917\tau^3_{motor,des} + 0.0747\tau^2_{motor,des} + 0.5083\tau_{motor,des} + 1.973 \text{ Volts} \quad (5.23)$$

The tuning of the position controller parameters is further discussed in section 6.4.

5.6 Conclusions

In this chapter two pressure controllers were developed. The first combined the cylinder and inverse valve models with proportional and integral feedback. Feedback was more effectively integrated by using the feedback linearization technique. The second pressure controller was designed as an alternate controller, to compare in trajectory tracking performance to the first controller. This alternate controller was a simple combination of deadzone compensation and feed-forward, proportional, and derivative action. An overall position controller was then presented, which could make use of either pressure controller, and operate in the hybrid mode, or the pneumatic mode. The controllers are tuned in the next chapter, and their relative effectiveness in position tracking evaluated.

Chapter 6 – System Validation

6.1 Introduction

With the GEN2 actuator having been designed, built, modeled, and the controllers designed, the remaining tasks was to tune the controllers and evaluate the closed-loop system performance. The system was evaluated by first comparing the ANN based controllers against the alternate PD+FF based controller. The GEN2 system acting in the hybrid mode (pneumatic+electric actuation) and pneumatic mode (purely pneumatic actuation) were compared for position tracking capability. The controllers' robustness to payload mismatch was also investigated. The efficacy of the modelling was investigated by comparing the model based and the feedback based portions of the outputs of the position and pressure control loops. Finally the GEN2 actuator was compared to the prior art, with specific attention to the GEN1 actuator, was it as the most similar in design and intended application. As the HPEA research in the literature was quite limited, the performance was primarily contrasted with several purely pneumatic actuators/controller publications.

6.2 Loading Conditions

As discussed in chapter 4, several system loading conditions were developed. A nominal mass was used for the majority the system evaluation trials. This mass provided both a gravitational and inertial load on the system for the vertical orientation testing of the GEN2 system. As previously discussed, operating the arm in the horizontal plane is a second possible loading configuration. As the horizontal configuration was inconvenient, given the constraints of the lab space available, an alternate analogous loading condition was chosen. A counterweight (recall Figure 3.3) was added to the link, so that when no payload is attached, the gravity load of the arm was balanced. This

results in a purely inertial load, which is analogous to the load condition seen in horizontal operation, while maintaining the practical convenience of the physically vertical arrangement.

To test the controllers' robustness to changes in system mass, additional loading conditions were tested in the vertical configuration. The end of link payload masses were physically increased or decreased from the nominal case, without changing the controller parameters or the mass in the system model used by the controller. Changing the mass of the system affected the overall loading in two ways: via the gravitational load on the system as well as the inertial load. The summary of the overall effects of the various loading conditions are summarized in Table 6.1

Table 6.1 Definition of loading conditions.

Loading Condition	**Inertia (kgm^2)**	**Peak Gravity Load (Nm)**	**Max Expected Torque Requirement (Nm)†**
Zero Gravity	0.086	0	0.530
Mass Increase (change from nominal)	0.765 (+34.4%)	11.0 (+38.2%)	16.70 (+37.0%)
Nominal	0.569	7.93	11.5
Mass Decrease (change from nominal)	0.377 (-33.8%)	4.79 (-39.6%)	7.13 (-37.8%)

†Where the inertia torque was calculated using 6.2 rad/s^2 as maximum acceleration

6.3 Desired Trajectories

A variety of desired trajectories were used to evaluate the effectiveness of the system. As the actuator was designed to be used in robotic arms, a blended point-to-point move was selected for the primary evaluation trajectory as was done with the GEN1 actuator (Bone & Chen, (2012); Bone, Xue, Flett, (2015)). Although step inputs are also common for general controller evaluation, it is not a trajectory that would typically be used in practical robotic implementation. It was preferable to tune a controller to the application, not an arbitrary step input. Smooth trajectories across position, velocity, acceleration, and jerk, were preferred to abrupt trajectory changes which would introduce step changes to the system. These impulses are typically much more difficult to control, as they exceed the physical bandwidth of the system, and can lead to oscillation or instability.

The chosen trajectory was the cycloidal trajectory defined by (6.1) through (6.4). An example of its position, velocity and acceleration curves is given in Figure 6.1. This cycloidal trajectory was selected to allow better comparison to the GEN1 which used the same trajectory.

$$\theta_{Des}(t_i) = \theta_{start} + \omega\frac{\theta_{end} - \theta_{start}}{2\pi}t_i - \frac{\theta_{end} - \theta_{start}}{2\pi}\sin(\omega t_i) \tag{6.1}$$

$$\dot{\theta}_{Des}(t_i) = \omega\frac{\theta_{end} - \theta_{start}}{2\pi} - \omega\frac{\theta_{end} - \theta_{start}}{2\pi}\cos(\omega t_i) \tag{6.2}$$

$$\ddot{\theta}_{Des}(t_i) = \omega^2\frac{\theta_{end} - \theta_{start}}{2\pi}\sin(\omega t_i) \tag{6.3}$$

$$\omega = \frac{2\pi}{t_{move}} \tag{6.4}$$

where θ_{start} and θ_{end} are the starting point and ending point of the move, respectively; ω is the angular frequency used in the move; and t_i is the current

discrete time. The angular frequency is determined by the desired duration for the move, t_{move}. This value is again application dependent. For example if the actuator was used in a production task and involved a point to point move, it would be desirable to cover the distances as quickly as possible (to minimize the time to complete the task and maximize production), while satisfying the desired level of accuracy. If the robot was used in an automatic gluing task, for example, it may need to more accurately match a certain position trajectory at a certain velocity trajectory, rather than performing the fastest possible move. Of course the configuration and geometric specifications of any components distal to the actuator in question (*e.g.* other actuators/links in a robot arm) must also be considered to determine the maximum achievable velocity. Recall the 0.250 m/s tool velocity limit as discussed in section 3.2. In a robotic arm, the tool velocity is a result of the combined effects of multiple joint speeds. As this research addressed only a single joint, the velocity was considered at the end of the link, at the payload mass. If the actuator was used as part of a multi-DOF system, the joint trajectory would need to be re-evaluated in the context of the tool velocity as affected by the other joints. For the GEN2 actuator as the sole actuator, if acting in a collaborative speed reduced mode the maximum angular operating speed would be:

$$\dot{\theta}_{\max} = \frac{\dot{y}_{\max}}{L_{link}} = \frac{0.250 m/s}{0.6m} = 0.417 rad/s = 24°/s \tag{6.5}$$

where $\dot{y}_{\max}$ represents the maximum tangential velocity at the end of the link, where the tool/payload would be. As the link (or multiple links in a full multi-DOF arm) length increases, the maximum joint velocity decreases. The value of maximum angular velocity is, of course, then highly dependent on the link length. Since the robot might need to operate at higher speeds when humans are not actively collaborating, or if a shorter link length was used, the GEN2 should be capable of moving at larger velocities than this maximum safety speed, for this

particular link length. The move time selected for the largest move was 3 s, slightly faster than the 4 s second move time used for the evaluation of the GEN1 actuator (Bone & Chen, (2012)). As is shown in Figure 6.1, for a 0° to 90° move over 3 seconds the maximum angular velocity was 60°/s, which is two and a half times as large as the angular velocity corresponding to 0.250 m/s at the link end. Operating with a larger maximum speed is more difficult for the controller as it requires larger accelerations and thus places a larger load on the actuator.

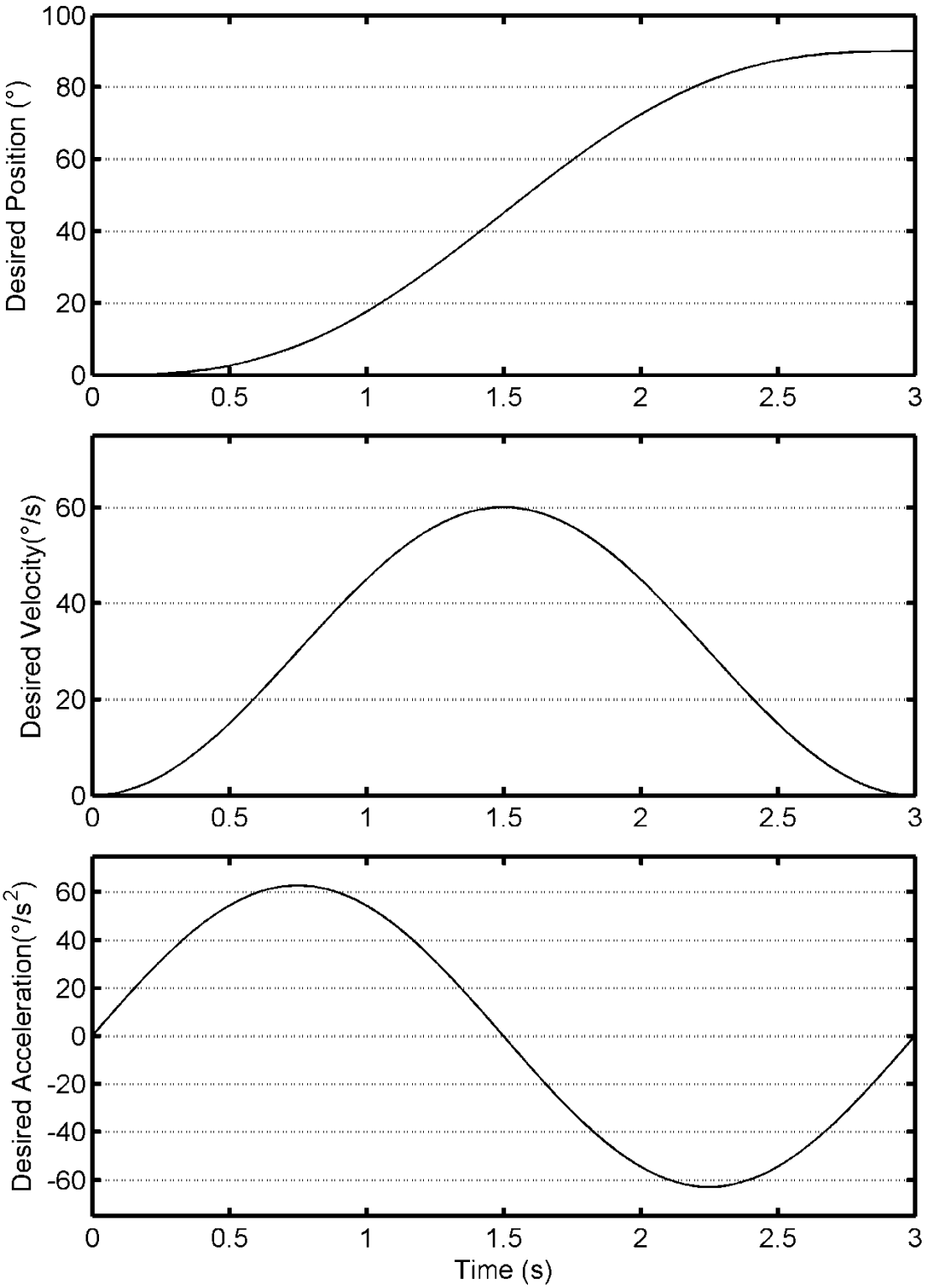

Figure 6.1 Example of cycloidal trajectory, of a 90° move over 3 seconds.

To compare the pneumatic system to those from the prior literature, a sine trajectory was also evaluated. Sine wave trajectories, along with steps, are the most common trajectories seen in the pneumatic actuator control literature. They are often used for generic control design, when the system is not being designed/evaluated for a specific application. An example of the sine position, velocity and acceleration is given in Figure 6.2, and expressed mathematically as:

$$\theta_{Des}(t_i) = \theta_{neutral} + \theta_{amp}\sin(\omega_s t_i + \varphi) \tag{6.6}$$

$$\dot{\theta}_{Des}(t_i) = \omega_s\theta_{amp}\cos(\omega_s t_i + \varphi) \tag{6.7}$$

$$\ddot{\theta}_{Des}(t_i) = -\omega_s^2\theta_{amp}\sin(\omega_s t_i + \varphi) \tag{6.8}$$

where $\theta_{neutral}$ is the offset of the neutral point from zero, θ_{amp} is the amplitude of the sine wave, and ω_s is its frequency. Finally, the phase shift, φ, allowed the phase to be adjusted. This allowed the trajectory to be shifted in time to avoid the infinite acceleration caused by a discontinuous velocity profile when this trajectory is moved into from some other previous trajectory.

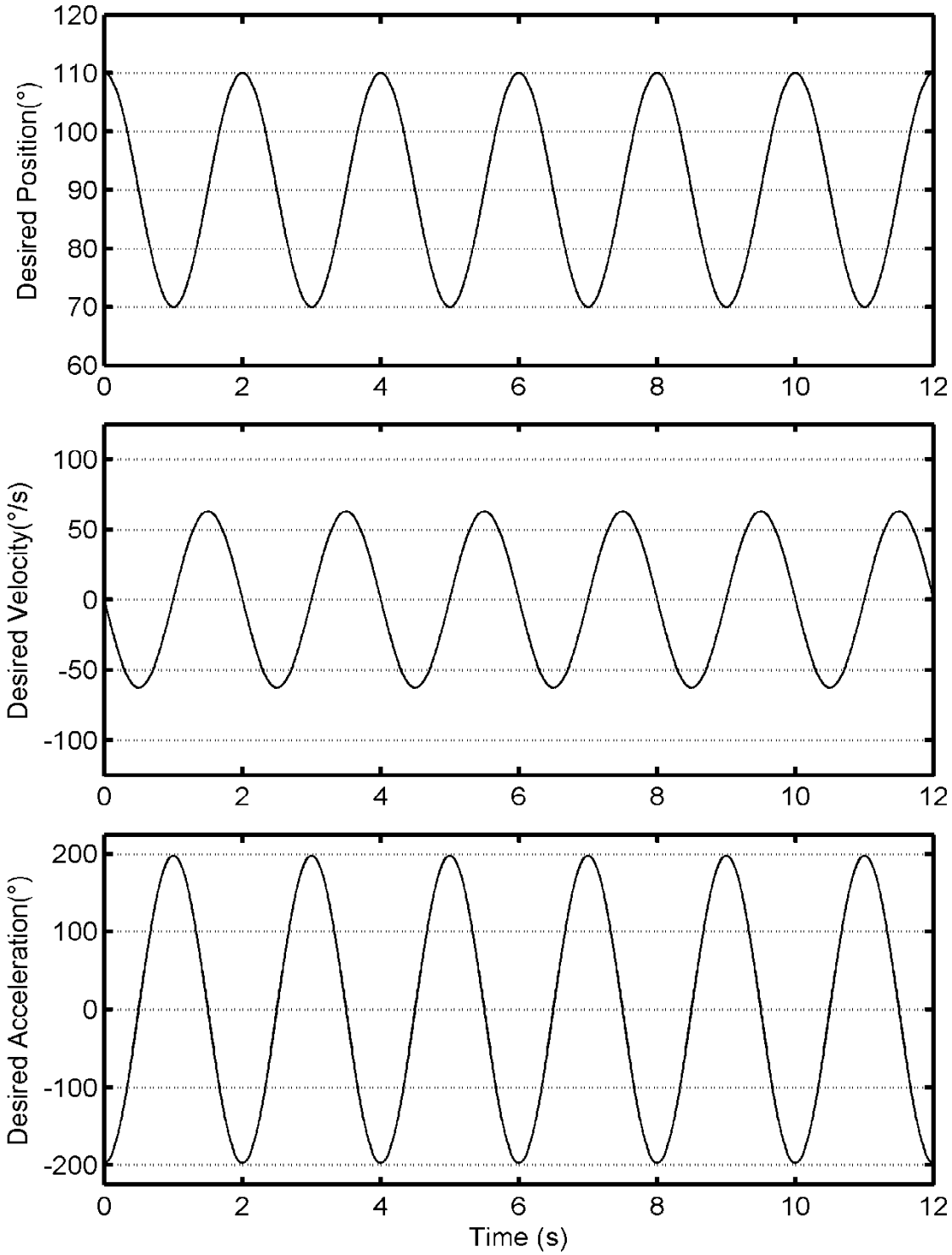

Figure 6.2 Example of 6 cycles of a 0.5 Hz, 20° amplitude sine trajectory, $\varphi = \frac{\pi}{2}$.

6.4 Controller Tuning

Four combinations of controller and plant, as described in Chapter 5, were separately implemented to evaluate and compare the pneumatic vs. hybrid operation, as well as ANN-based vs. alternate controller for position control. These four combinations are as follows:

1. ANN-based controller applied to the pneumatic actuator only for position control; referred to as **ANNB**.
2. ANN-based controller applied to the hybrid actuator for position control; referred to as **HANNB**.
3. Alternate controller applied to the pneumatic actuator only for position control; referred to as **ALTB**.
4. Alternate controller applied to the hybrid actuator; referred to as **HALTB**.

6.4.1 Pressure Controller Tuning

The overall goal of the actuator was accurate position control. As the primary driving force in the system is provided by the pneumatic actuators, accurate pressure control was important to overall system performance. The two pressure controllers were tuned with the goal to minimize the root mean square pressure error (RMSPE) defined as:

$$RMSPE = \sqrt{\frac{\sum_{k=0}^{N_{points}} \left(P_{des}(t_k) - \hat{P}(t_k) \right)^2}{N_{points}}} \tag{6.9}$$

where N_{points} is the number of points being evaluated.

Tuning of the parameters was performed manually and iteratively. Gains were evaluated experimentally and the RMSPE calculated. The link was set to ~50% of its range and clamped in place, as without a position controller, the

actuator could damage itself if allowed to move freely. A pressure trajectory was applied and tracked using the equations of (5.10), (5.12), and (5.13) for the ANN based pressure controller. Similarly, using (5.14) and (5.15), the alternate pressure controller was tuned. The tuned parameters of the ANN pressure controller are listed in Table 6.2. The tuned parameters of the alternate controller are listed in Table 6.3.

Table 6.2: Tuned parameters of the ANN based pressure controller.

Parameter	Value
$\lambda_{\dot{p}}$	0.95
$K_{P,pressure,1}$	40
$K_{P,pressure,2}$	20
$K_{I,pressure,1}$	15
$K_{I,pressure,2}$	5

Table 6.3: Tuned parameters of the alternate pressure controller.

Parameter	Value
$\lambda_{\dot{p}}$	0.95
$u_{deadzone}\left(\times 10^{-2}\%\right)$	0.2
$K_{P,pressure,alt}$	3×10^{-5}
$K_{D,pressure,alt}$	1×10^{-8}
$K_{FF,pressure,alt}$	5×10^{-7}

6.4.2 Position Controller Tuning

With the pressure controllers tuned, the outer position controllers could be tuned in position tracking experiments. A multi-step cycloidal trajectory, as in Figure 6.3, was used to tune the position controller parameters. The trajectory contains both large (90°) and small (1°) moves to ensure the tuned parameters result in an effective controller over a variety of cases. The details of this trajectory are further discussed in section 6.5, where it is used to evaluate the system position tracking performance. The position controllers were tuned for the nominal payload, as well as for the zero gravity loading condition, as in Table 6.1. The controllers were tuned for both cases, as larger masses act to damp out errors in torque/pressure. When the external load is small, (as in the zero gravity loading condition) the same torque/pressure error magnitude has a much larger impact on the magnitude of position error, due to the ease of acceleration of the smaller mass. A larger acceleration error would lead to a larger position error. As such different controller parameters were required for the two cases.

As trajectory tracking was the goal, the position controllers were manually, iteratively tuned to minimize the position error via RMSE:

$$RMSE = \sqrt{\frac{\sum_{k=1}^{N_{points}} \left(\theta_{des}(t_k) - \hat{\theta}(t_k) \right)^2}{N_{points}}} \tag{6.10}$$

Using (5.18), (5.19)-(5.21) and the appropriate pressure controller (tuned per Table 6.2 and 6.3) the ANNB and ALTB position controllers were iteratively tuned. With the addition of (5.22) and (5.23), the HANNB and HALTB position controllers were tuned in the same manner. The tuned parameters for the ANNB and HANNB position controllers are listed in Table 6.4, note that the same pneumatic gains were used in both cases. Similarly the ALTB and HALTB tuned parameters are listed in Table 6.5. Due to the natural damping of the pneumatic

system, the derivative feedback for the pneumatic component had little useful influence and only a relatively small value was used.

Table 6.4: Tuned parameters of the ANNB and HANNB position controllers.

Parameter	**Value Tuned for Nominal Payload**	**Value Tuned for Zero Gravity Loading Condition**
$\lambda_{\dot{\theta}}$	0.94	0.94
$K_{P,\theta}$	290	75
$K_{D,\theta}$	0.05	0.05
$K_{P,motor}$	500	80
$K_{D,motor}$	1	5

Table 6.5: Tuned parameters of the ALTB and HALTB position controllers.

Parameter	**Value Tuned for Nominal Payload**	**Value Tuned for Zero Gravity Loading Condition**
$\lambda_{\dot{\theta}}$	0.94	0.94
$K_{P,\theta}$ pneumatic mode	275	75
$K_{D,\theta}$ pneumatic mode	0.1	0.1
$K_{P,\theta}$ hybrid mode	275	60
$K_{D,\theta}$ hybrid mode	0.1	0.1
$K_{P,motor}$	515	200
$K_{D,motor}$	1	10

Concurrent with the position controller parameter tuning the friction compensation was also manually tuned as discussed in Chapters 4 and 5. A sign dependent friction constant proved to be the most suitable, as previously discussed. The approximate range of friction was established in section 4.2.3. The friction compensation values were tuned manually and iteratively, along with the position controller gain. The friction was implemented via (5.17) and tuned for the nominal payload loading condition, as well as for the zero gravity condition. The same compensation values were used for all controllers and are summarized in Table 6.6.

Table 6.6: Tuned parameters of the friction compensation.

Parameter	**Value Tuned for Nominal Payload (Nm)**	**Value Tuned for Zero Gravity Loading Condition (Nm)**
τ_{f+}	0.65	0.2
τ_{f-}	-1	-0.25
$\tau_{f+,offset}$	0.005	0.0025
$\tau_{f-,offset}$	-0.005	-0.0025

6.5 Cycloidal Vertical Experiments

The cycloidal trajectory in the vertical loaded orientation was the primary trajectory used to evaluate the system, as it represented the envisioned typical operation in the highest loading orientation. Further, it was the most comparable trajectory to the GEN1 actuator, as in Bone & Chen (2012) and Bone, Xue, Flett (2015). A variety of tests were performed to characterize the position tracking performance of the system. As the majority of the torque was provided by the pneumatic system, all tests could be performed in the pneumatic mode, where

the motor is left idle. Alternately the tests could also be performed in the hybrid mode where the electric motor contributes to the net torque output of the system. Pneumatic mode testing allowed for a more direct comparison to the prior art, which primarily employs pneumatic rather than hybrid actuation. Further, it served to establish a baseline for the system which was used to determine the amount of improvement introduced by the hybrid mode. As the motor was ungeared, and the torque capacity relatively small, purely electric tests could not be performed with this trajectory, as the motor could not satisfy even the gravitational torque required across the angular position range.

Tests were performed across different point-to-point ranges. A 0° to 90° move was used to evaluate the systems performance at larger velocities and accelerations. This move started with the lowest gravitational load and ends at the largest (recall Figure 4.6). A 90° to 91° to 90° move was used to evaluate the system's ability to perform small moves, as they are typically more difficult to achieve with pneumatic systems (van Varseveld & Bone, 1997). Finally a 90° to 45° to 0° move was evaluated to show moderate, multi-segmented moves, and return the system to the zero gravity position where it could be safely shut down and depressurized. These moves were performed over a single multi-segment cycloidal trajectory tracking experiment. The results were analyzed across the four distinct regions shown in Figure 6.3. As shown, between each region a dwell period was inserted to allow the system to settle. A "pre-charge" region is also shown. During this region the cylinder chambers were pressurized to their desired initial pressures. The data from the pre-charge region was not evaluated for performance. The test trajectory regions were as follows:

1. **Region 1**: 0° to 90°.
2. **Region 2**: 90° to 91° to 90°.
3. **Region 3**: 90° to 45° to 0°.
4. **Region 4**: the combination of regions 1 to 3, *i.e.* motion from 0° to 90° to 91° to 90° to 45° to 0°.

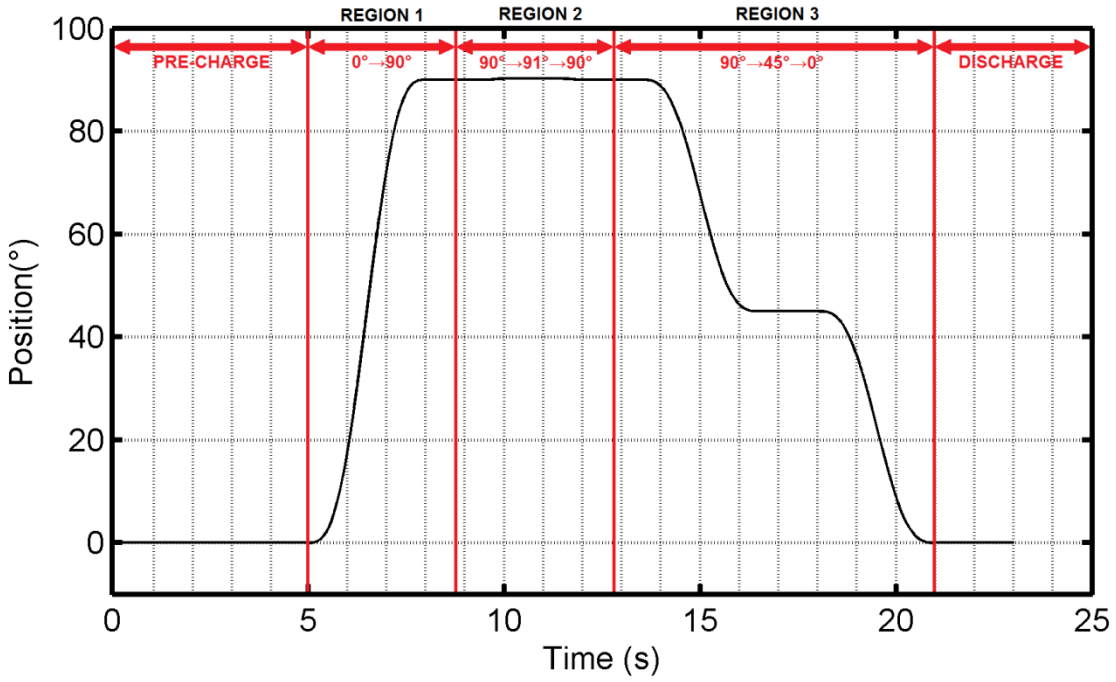

Figure 6.3 Illustration of the desired trajectory for a full experimental trial, including the pre-charging of the system, the three individual regions and the full discharging of the system to atmosphere.

Four combinations of controller and plant, as described in section 6.4, were separately implemented to evaluate the performance, namely the ANNB, HANNB, ALTB, and HALTB position controllers. With each of these position controllers three distinct loading conditions were tested, as listed in Table 6.1:

1. Mid-range payload, at which the controllers were tuned, and the model values populated. Referred to as **Nominal**.
2. Increased loading by ~37% of the torque of loading condition 1. Referred to as **+Inertia**.
3. Decreased loading by ~38% of the torque of loading condition 1. Referred to as **–Inertia**.

The data for the four regions was collected over a single continuous experiment, as shown in Figure 6.3. This experiment was repeated for each combination of the three loading conditions and four controllers, five times each.

A total of 60 experiments were performed, the data was analyzed over a total of 4 regions, for a total of 240 datasets. These datasets were individually analyzed and the results of the 5 like repetitions of each averaged to produce a single metric for each region, loading condition, and controller combination. Finally the resultant 48 averaged cases were compared. The summaries of the non-averaged data for each individual dataset are listed in Appendix B.

The system tracking error and performance could have been evaluated in a variety of ways due to the dual linear and rotational nature of the hybrid actuator. It could have been reported as position error at the end of the link, in mm, though error would be a function dependent on the length of the link which could skew the interpretation of the level of error. Reporting the error in angular units would be more reasonable as it is consistent, regardless of output link length, but the error in mm in the coupled cylinder would be dependent upon pinion size selection. Due to the small number of hybrid actuators discussed in the literature, the results were also compared to the larger number of purely pneumatic actuator control publications. As these were typically linear pneumatic cylinders, the error in mm of the piston position was the typical result reported. Thus the error in mm at the cylinder was the evaluation method selected, for ease of comparison with prior literature. The angular errors in radians were converted by multiplying them by the pinion gear radius (r_{gear} = 0.0315 m). The resolution of the encoder corresponds to a linear resolution of 0.00247 mm at the cylinder.

For each region, a Maximum Absolute Error (MAE) and a RMSE (as in (6.10)) were calculated to evaluate the position tracking performance. Where MAE was defined as:

$$MAE = \max\left(\left|\theta_{des}(t_i) - \hat{\theta}(t_i)\right|\right),\ for\ i = 1,2,3,\ldots,N_{points} \tag{6.11}$$

Table 6.7 shows the summary of the results of the averaged data. An example of the full test, *i.e.* Region 4, is shown in Figure 6.4 and 6.5 for the ANNB controller in the nominal loading condition. These figures illustrate the position tracking error as well as the inner loop pressure tracking error. Figures 6.6 and 6.7 show an example of the HANNB, also using the nominal loading condition. Figures 6.8 and 6.9 show an example of the ALTB, also using the nominal loading condition. Finally, Figures 6.10 and 6.11 show a typical example of the HALTB controller for the nominal loading condition.

The pressure tracking errors shown in Figures 6.5, 6.7, 6.9. and 6.11 were all predominately high frequency. The amplitude of this error became largest during the portions of the trajectory where the link is being moved, and requires a pressure difference change to happen simultaneously with a chamber volume change. The ALTB and HALTB pressure errors had a slightly larger amplitude for the high frequency component than the ANNB and HANNB. The pressure error changes from pneumatic mode to hybrid mode of each controller were fairly minimal. This was expected; as the inner pressure controller has no direct hybrid related inputs. The hybrid mode only altered the position controller portion.

Position tracking is shown in Figures 6.4, 6.6, 6.8, and 6.10. The errors were both fairly low across all cases, though some trends do differ between controllers. Across all controllers the error tends to be biased towards the positive direction. This means that the link was moving slightly below the trajectory desired. This bias was introduced due to the direction of the predominant load, the gravitational torque. It can be seen that at the dwell angles between cycloidal trajectories that all cases tended towards zero steady state error (SSE). The tendency towards zero SSE was due to position controller feedback and the friction compensation term (recall Section 5.5.2). The error tended to be larger and more oscillatory for the larger moves, where the largest accelerations and velocities were desired. For the small Region 2 trajectory, there was typically a non-oscillatory error, as less of an acceleration/torque change was required. For

both the ANNB/HANNB and ALTB/HALTB there was a clear reduction in error magnitude when the hybrid action was included.

In Figure 6.6, the HANNB controller, it can be seen that the amplitude of oscillation, and peak errors of the moves tended to be in the middle of the move. This corresponds to the largest velocity trajectory, as is shown in Figure 6.1. In Figure 6.4, the ANNB controller, the error peaks per move, especially seen in Region 1 and the first move of Region 2, appear to be largest in two places. These correspond being the maximum and minimum acceleration requirements of the move, again as seen in Figure 6.1. This implies that the hybrid mode was most capable of improving the acceleration related error, which when reduced leaves the velocity related error as the largest component.

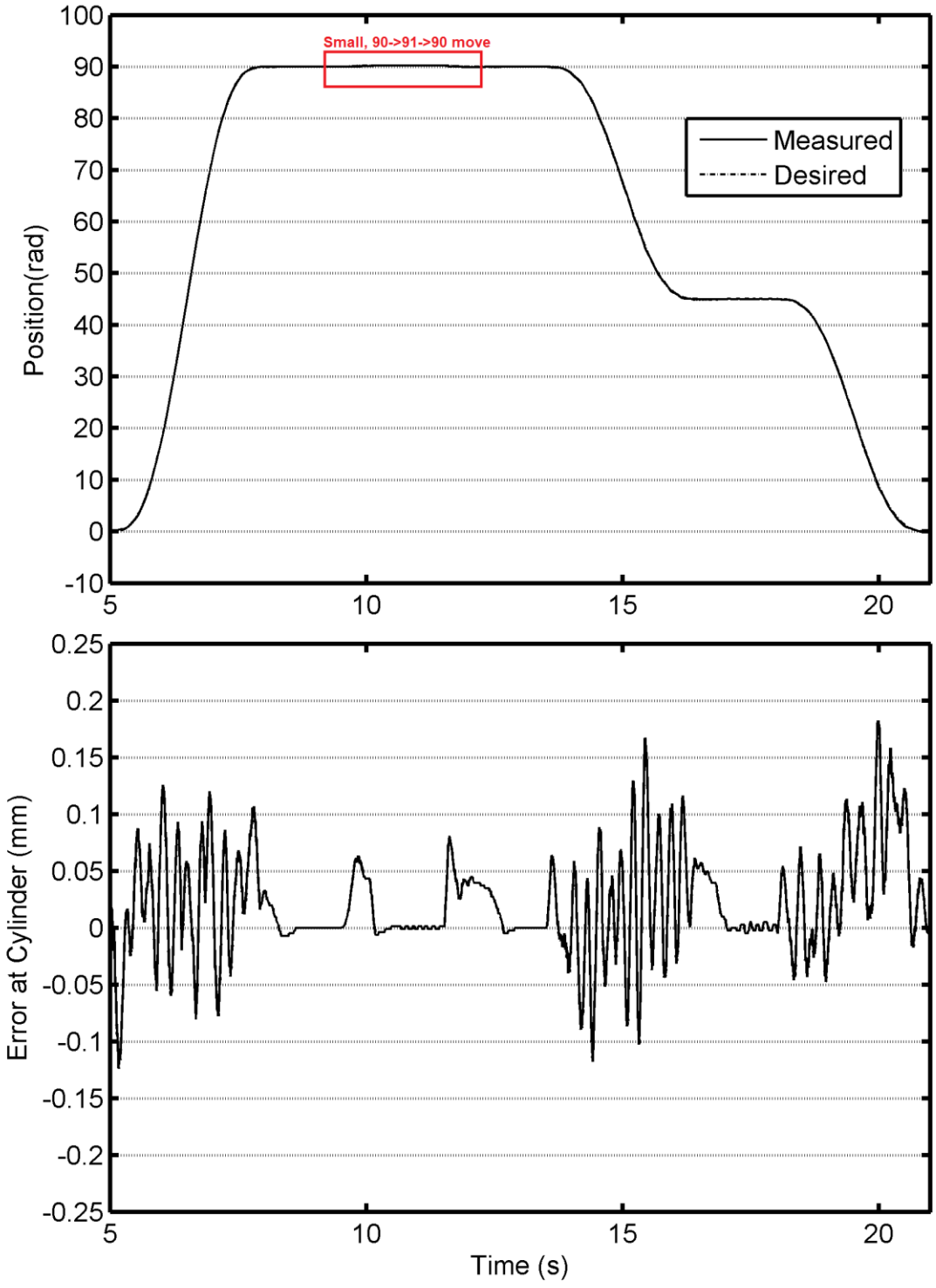

Figure 6.4 Typical position error for ANNB controller multi-cycloidal move. Error in mm at the cylinder. Under nominal loading condition.

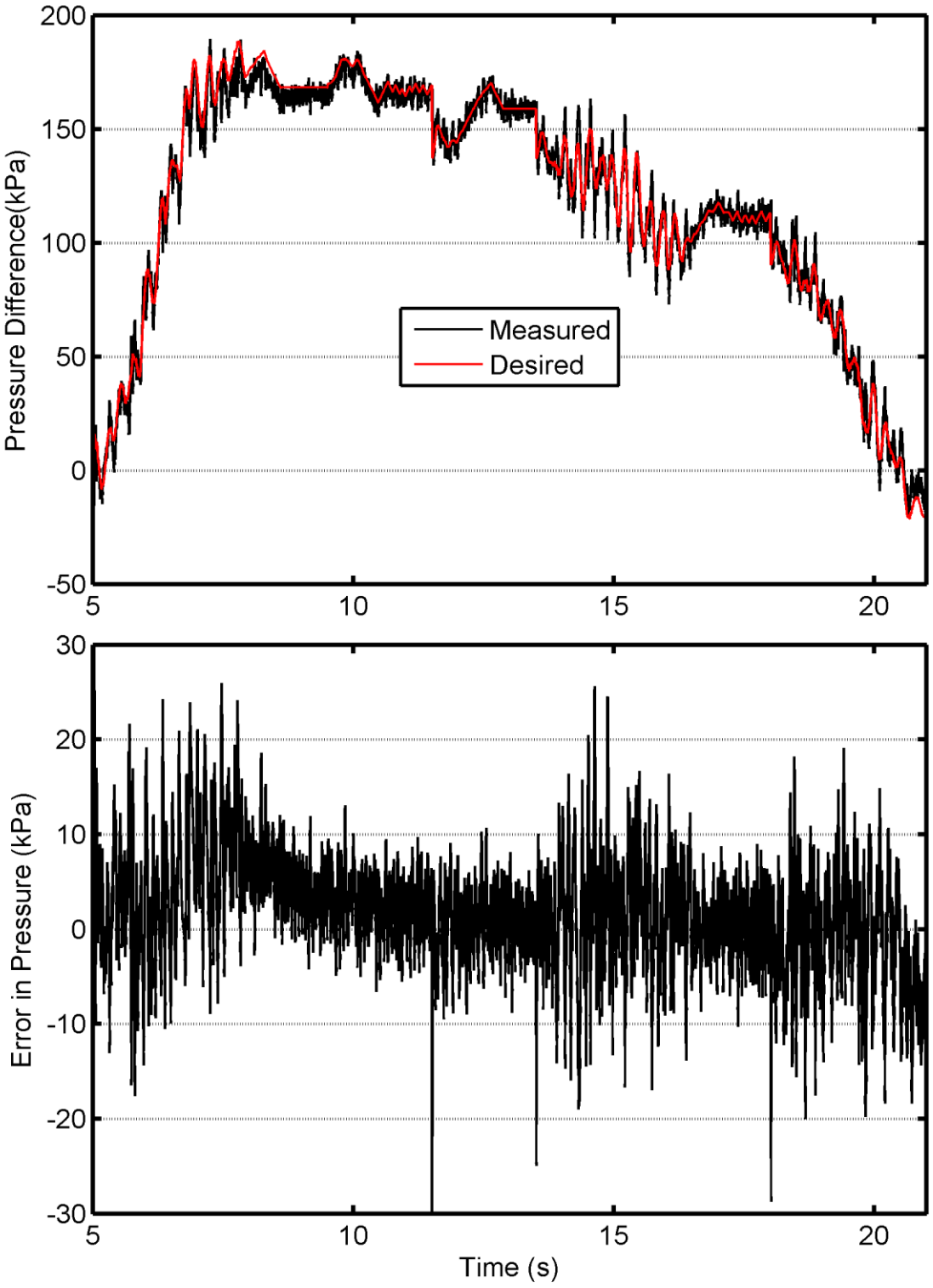

Figure 6.5 Typical pressure error for ANNB controller multi-cycloidal move. Under nominal loading condition.

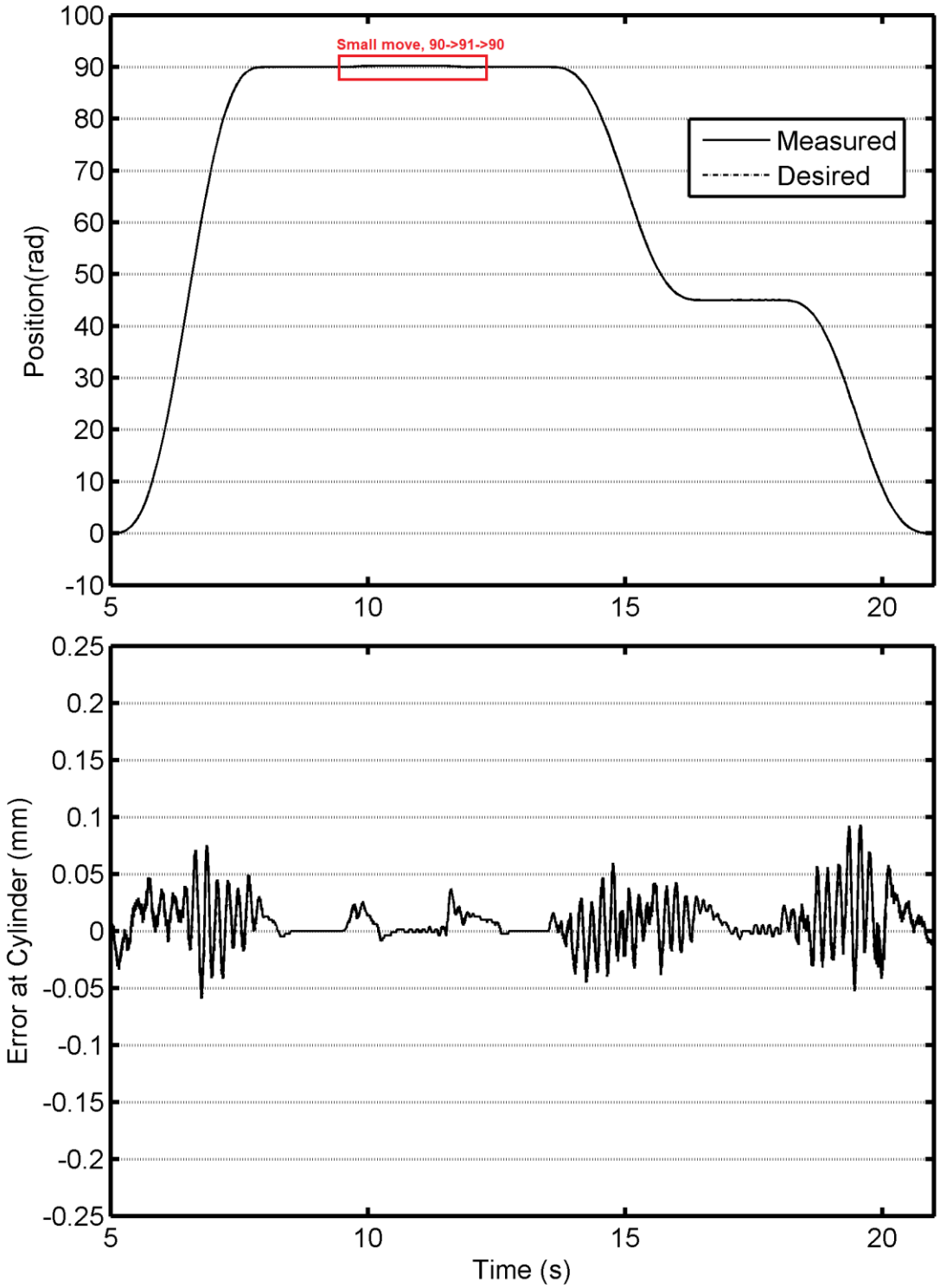

Figure 6.6 Typical position error for HANNB controller multi-cycloidal move. Error in mm at the cylinder. Under nominal loading condition.

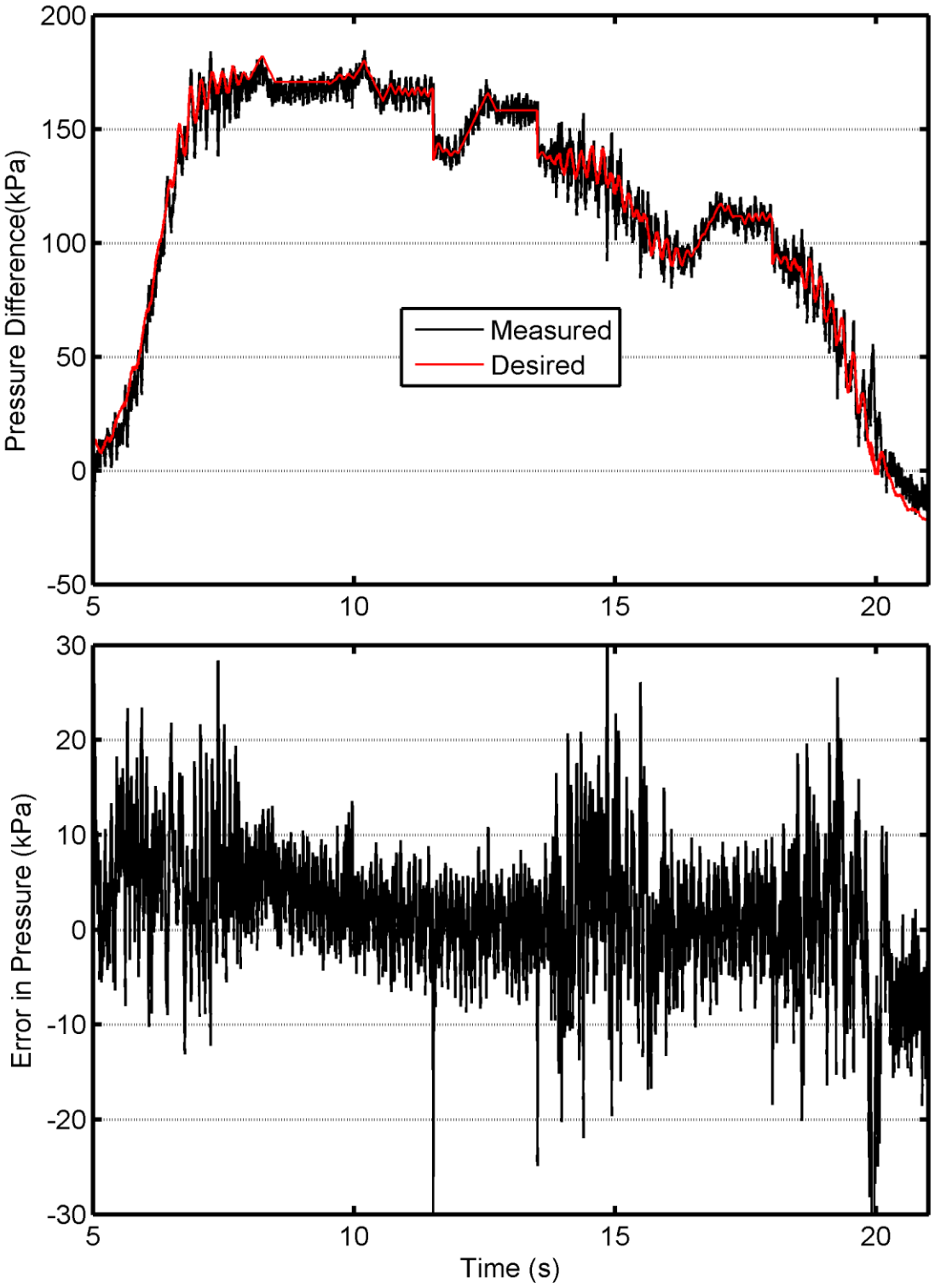

Figure 6.7 Typical pressure error for HANNB controller multi-cycloidal move. Under nominal loading condition.

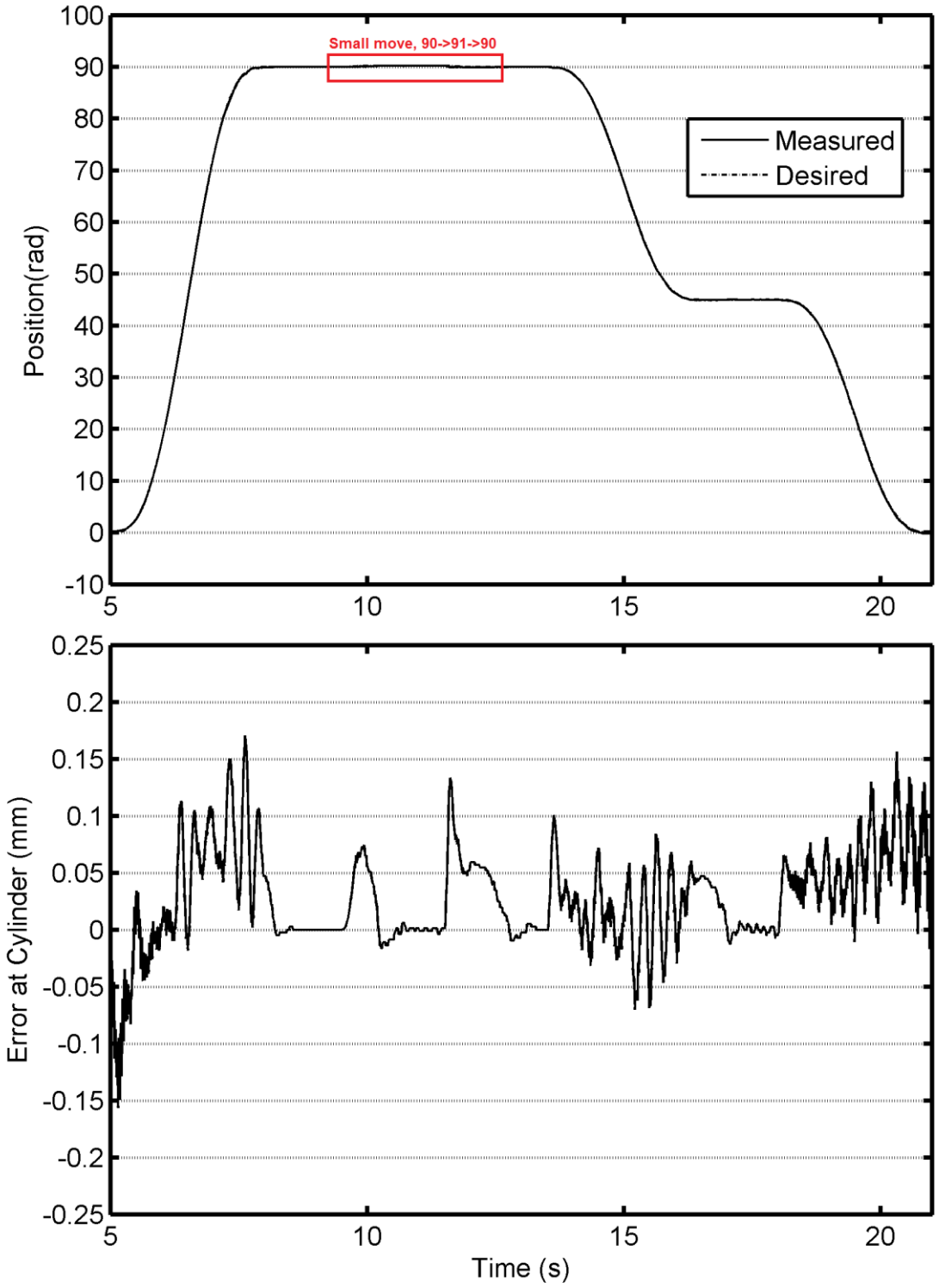

Figure 6.8 Typical position error for ALTB controller multi-cycloidal move. Error in mm at the cylinder. Under nominal loading condition.

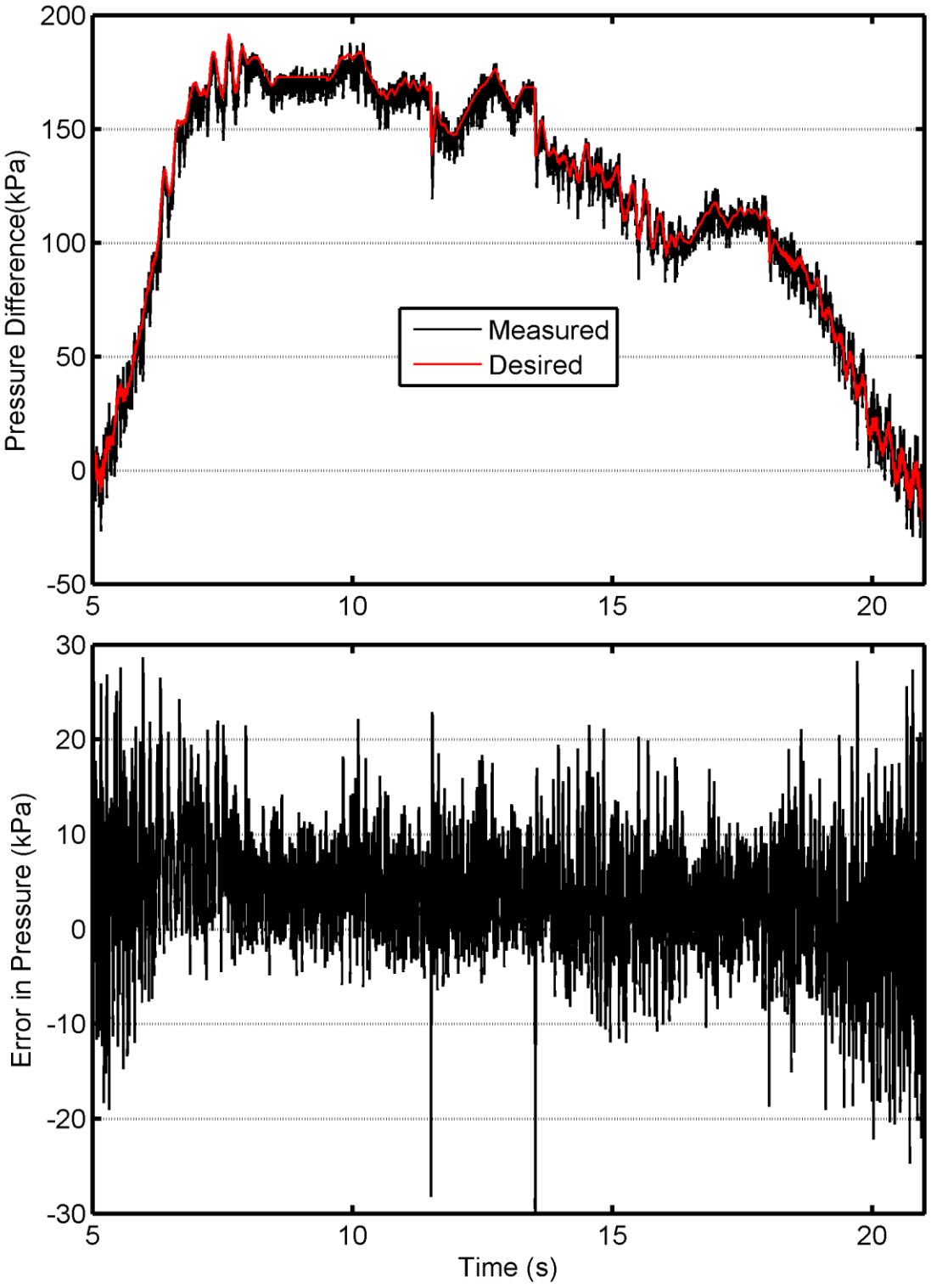

Figure 6.9 Typical pressure error for ALTB controller multi-cycloidal move. Under nominal loading condition.

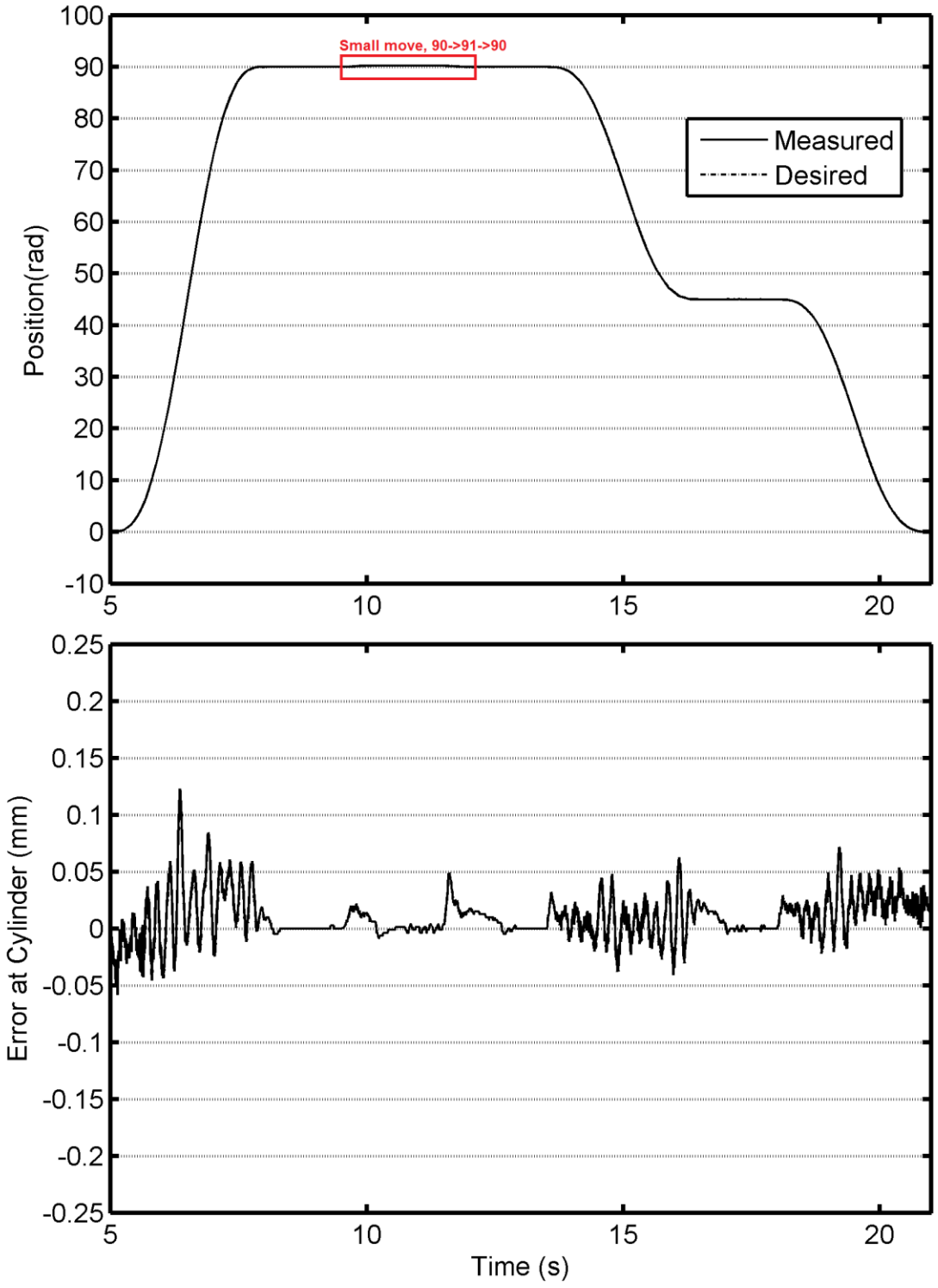

Figure 6.10 Typical position error for HALTB controller multi-cycloidal move. Error in mm at the cylinder. Under nominal loading condition.

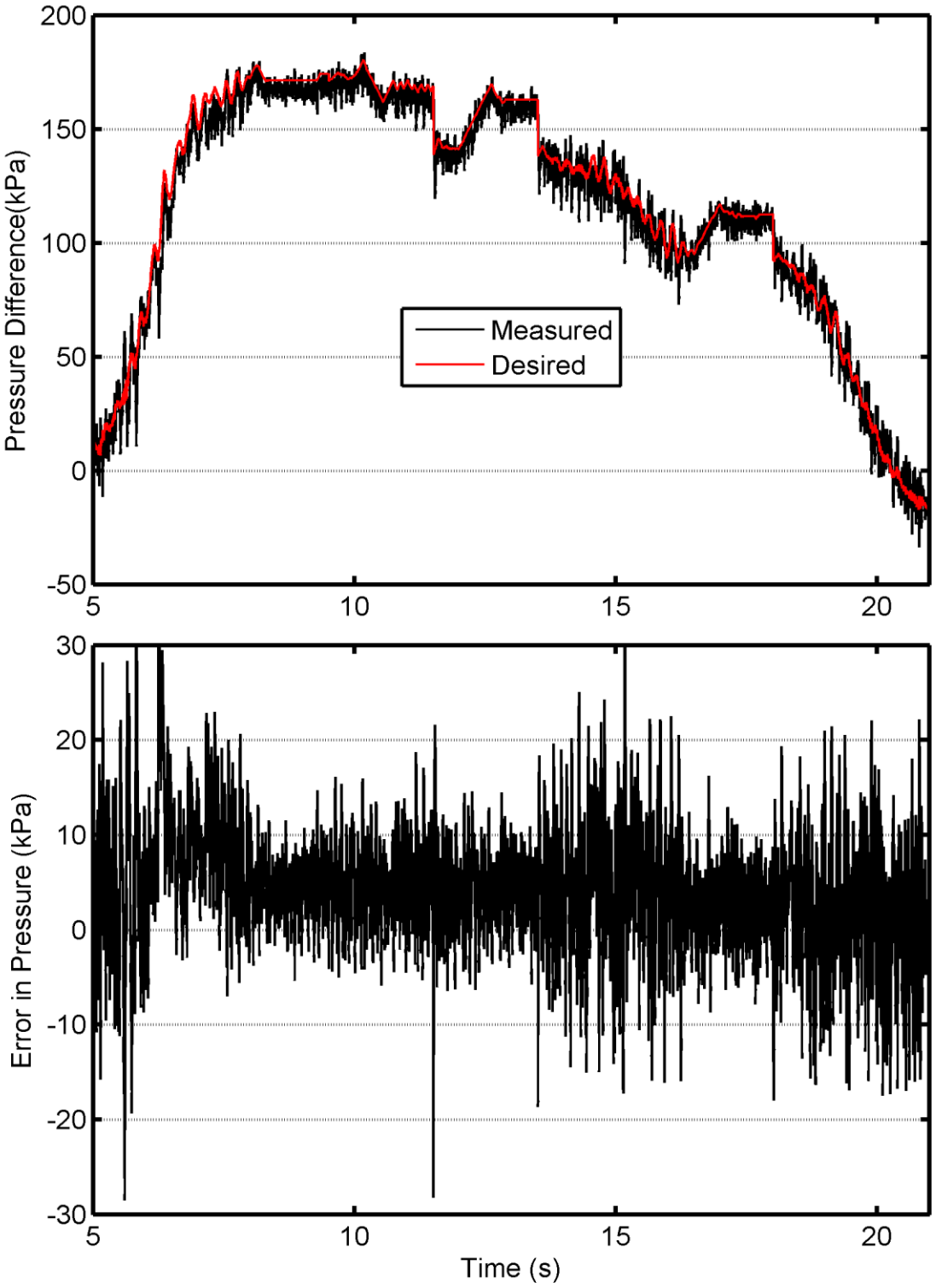

Figure 6.11 Typical pressure error for HALTB controller multi-cycloidal move. Under nominal loading condition.

Table 6.7 Summary of trials comparing controllers across a variety of loading conditions. Lowest RMSE, or MAE for each loading condition indicated in blue. Averaged from 5 trials.

		Region 1: 0°→90° Piston Error (mm)				Region 2: 90°→91°→90° Piston Error (mm)			
		ANNB	**ALTB**	**HANNB**	**HALTB**	**ANNB**	**ALTB**	**HANNB**	**HALTB**
+Inertia	**RMSE (mm)**	0.230	0.263	0.104	0.111	0.247	0.283	0.148	0.163
Nominal		0.053	0.067	0.026	0.027	0.038	0.036	0.010	0.011
-Inertia		0.203	0.209	0.089	0.082	0.211	0.217	0.090	0.087
+Inertia	**MAE (mm)**	0.502	0.505	0.269	0.294	0.573	0.784	0.467	0.450
Nominal		0.164	0.193	0.098	0.097	0.093	0.119	0.040	0.046
-Inertia		0.386	0.363	0.231	0.229	0.450	0.472	0.244	0.235
		Region 3: 90°→45°→0° Piston Error (mm)				**Region 4: 0°→90°→91°→90°→45°→0° Piston Error (mm)**			
		ANNB	**ALTB**	**HANNB**	**HALTB**	**ANNB**	**ALTB**	**HANNB**	**HALTB**
+Inertia	**RMSE (mm)**	0.194	0.215	0.080	0.094	0.217	0.245	0.105	0.118
Nominal		0.045	0.051	0.021	0.021	0.045	0.053	0.021	0.021
-Inertia		0.147	0.149	0.069	0.062	0.178	0.183	0.080	0.074
+Inertia	**MAE (mm)**	0.415	0.475	0.306	0.372	0.597	0.784	0.467	0.469
Nominal		0.177	0.164	0.091	0.092	0.186	0.194	0.103	0.106
-Inertia		0.359	0.339	0.245	0.199	0.462	0.472	0.259	0.268

Inspecting Table 6.7 the controllers could be compared most easily by first inspecting the results for the nominal loading conditions. The hybrid vs pneumatic controller/plant performance was established, by comparing the ANNB to the HANNB, and the ALTB to the HALTB. The HANNB was often the best result across all regions in both RMSE and MAE. Where the HANNB was not the best result (lowest error of all controllers) the HALTB controller was, illustrating the improvement of hybrid actuation. A similar result was seen across the payload mismatched conditions as well, where the lowest magnitudes of error were seen in the hybrid modes exclusively. Next, the two hybrid mode controllers/plants were compared to one another. The HANNB and HALTB errors

were fairly similar in magnitude across the nominal cases. Finally the pneumatic controller/plant performance could be seen by comparing the ANNB and ALTB cases. In most cases the ANNB control led to lower errors, although the magnitudes are fairly similar.

The absolute values of error listed in Table 6.7 were a good evaluation of objective performance of the individual cases. Yet since the magnitudes are similar, and the relative performance was being evaluated, the data was further analyzed to extract the percent change between cases. The percent change between the appropriate cases is summarized in Tables 6.8 to 6.11, Regions 1 through 4 respectively. Note that in Tables 6.8 to 6.11 that "%↓ in error from X to Y" implies the calculation in (6.12). The choice of denominator was based upon which controller was predicted to be superior. A negative value indicates that the controller predicted to be superior was in fact inferior for that case. In Tables 6.8 to 6.11, results conforming to the predicted superiority are marked in green, where those that were not are marked in red.

$$\%Change = 100\frac{X-Y}{X} \tag{6.12}$$

Table 6.8 Comparison of results for Region 1. Green indicates expected superior/inferior controller. Red indicates that the opposite was true. Averaged from 5 trials.

Region 1: 0→90	**Nominal**		**-inertia**		**+inertia**	
	RMSE	**MAE**	**RMSE**	**MAE**	**RMSE**	**MAE**
%↓ in error from ALTB to ANNB	20.1%	16.3%	2.71%	-6.34%	12.6%	0.61%
%↓ in error from HALTB to HANNB	3.55%	-1.12%	-7.36%	-1.05%	6.95%	8.73%
%↓ in error from ANNB to HANNB	51.8%	40.2%	56.4%	40.1%	55.0%	46.5%
%↓ in error from ALTB to HALTB	60.0%	49.9%	60.5%	36.9%	57.7%	41.7%

Table 6.9 Comparison of results for Region 2. Green indicates expected superior/inferior controller. Red indicates that the opposite was true. Averaged from 5 trials.

Region 2: 90→91→90	Nominal		-inertia		+inertia	
	RMSE	MAE	RMSE	MAE	RMSE	MAE
%↓ in error from ALTB to ANNB	-6.22%	21.7%	2.91%	4.78%	12.8%	26.9%
%↓ in error from HALTB to HANNB	10.9%	13.5%	-3.44%	-3.75%	9.59%	-3.79%
%↓ in error from ANNB to HANNB	73.7%	57.0%	57.0%	46.7%	40.2%	18.6%
%↓ in error from ALTB to HALTB	68.7%	61.1%	59.7%	50.2%	42.3%	42.6%

Table 6.10 Comparison of results for Region 3. Green indicates expected superior/inferior controller. Red indicates that the opposite was true. Averaged from 5 trials.

Region 3: 90→45→0	Nominal		-inertia		+inertia	
	RMSE	MAE	RMSE	MAE	RMSE	MAE
%↓ in error from ALTB to ANNB	11.0%	-7.67%	1.52%	-6.72%	9.87%	12.6%
%↓ in error from HALTB to HANNB	-1.93%	0.99%	-11.1%	-23.1%	16.4%	17.9%
%↓ in error from ANNB to HANNB	52.3%	48.4%	53.2%	31.8%	59.0%	26.4%
%↓ in error from ALTB to HALTB	58.3%	43.9%	58.5%	41.4%	56.3%	21.7%

Table 6.11 Comparison of results for Region 4. Green indicates expected superior/inferior controller. Red indicates that the opposite was true. Averaged from 5 trials.

Region 4: 0→90→91→90→45→0	Nominal		-inertia		+inertia	
	RMSE	MAE	RMSE	MAE	RMSE	MAE
%↓ in error from ALTB to ANNB	16.6%	4.01%	2.36%	2.25%	11.5%	23.8%
%↓ in error from HALTB to HANNB	1.11%	3.00%	-7.34%	3.35%	10.8%	0.52%
%↓ in error from ANNB to HANNB	53.1%	44.7%	56.4%	43.8%	51.5%	21.8%
%↓ in error from ALTB to HALTB	59.9%	46.3%	59.5%	43.2%	51.9%	40.1%

First inspecting these tables to compare hybrid vs pneumatic performance, the "%↓ in error from ANNB to ANNB" and "%↓ in error from ALTB to HALTB" can be evaluated. It can be seen across every region, and every loading condition that the hybrid mode was an improvement from the pneumatic mode, as was indicated in Table 6.7. In region 4 across all loading conditions and pressure controllers, the hybrid mode improves the RMSE by an average of 55.4% and the MAE by an average of 40%.

Next the hybrid controllers were compared to one another by inspecting the "%↓ in error from HALTB to HANNB". The percent difference was fairly small, but in most nominal cases the HANNB was the superior controller. For the overall test, Region 4, an RMSE difference of 1.11% and an MAE difference of 3.00% was observed. The largest difference was seen in the small move, Region 2, where the RMSE difference is 10.9% and the MAE difference 13.5% in favour of the HANNB. For the +inertia and –inertia cases, the superior/inferior controller varied much more.

Finally, the pneumatic only controllers were compared by inspecting the "%↓ in error from ALTB to ANNB". In the nominal loading conditions, depending on the region, and error metric the superior/inferior controller varies. In the overall test, Region 4, the ANNB improved the RMSE by 16.6% and the MAE by 4.01%.

Though the superior/inferior controllers varied depending on loading condition and region, overall the ANNB is typically superior to the ALTB, and the HANNB was typically superior to the HALTB. In all cases the HANNB was superior to the ANNB, and the HALTB is superior to the ALTB. The evaluation of Region 4, illustrates these trends most clearly, being an evaluation of the overall position tracking, over multiple step tests.

Table 6.7 also contains the RMSEs and MAEs for the robustness testing loading conditions, where the payload mismatch was introduced. To evaluate the robustness, the most useful metric was established by comparing the relative

change in error from the nominal payload to the +inertia and –inertia cases. The nominal loading condition RMSEs and MAEs were compared to the other loading cases as a percent change. The percent increase in error, indicates to what degree the controller is affected by the payload mismatch, and thus how robust. The percent increases in error are summarized in Tables 6.12 through 6.15. Both outer position controllers relied on the same acceleration model of the system. This meant that a change in dynamics, such as a payload mismatch from the value included in the acceleration model, should have a similar effect on the desired torque (via the position controllers). The pressure controllers then responded to this desired torque, with no additional payload dependence within the pressure controllers. For the +inertia case the desired torque requested would be too small, as mass value in the controller was the smaller nominal value, and the link would not accelerate as much as desired. For the –inertia case, the desired torque would be too high and the system would over accelerate. The mismatch would eventually be compensated for via the feedback in the position controller and the error would drop.

When inspecting Table 6.12 to 6.15 note that even though a controller type might have had a larger increase in percent error, the actual value of the error in the mismatch case might still be the lowest of the controllers, as indicated in Table 6.7. This can be illustrated by an example in Table 6.12 below. Observe Region 1's percent increase in error for the nominal vs. +inertia RMSE, for the ALTB and HALTB cases. The percent error increase was larger for the HALTB (319%) than the ALTB (304%). Though it can be seen in Table 6.7 that the magnitudes of RMSE for the +inertia for the HALTB and ALTB were: 0.111 mm and 0.263 mm respectively. So despite the larger percent increase for the HALTB, it still had the lower magnitude of error.

Table 6.12 Summary of Region 1 percent error increase in RMSE and MAE to payload mismatches. Averaged from 5 trials. Lowest error per case in blue.

		Region 1			
		ANNB	**ALTB**	**HANNB**	**HALTB**
%↑ in error from nominal to +inertia	**RMSE**	333%	297%	304%	319%
%↑in error from nominal to –inertia		282%	213%	244%	210%
%↑ in error from nominal to +inertia	**MAE**	206%	161%	174%	204%
%↑in error from nominal to –inertia		137%	87.7%	136%	136%

Table 6.13 Summary of Region 2 percent error increase in RMSE and MAE to payload mismatches. Averaged from 5 trials. Lowest error per case in blue.

		Region 2			
		ANNB	**ALTB**	**HANNB**	**HALTB**
%↑ in error from nominal to +inertia	**RMSE**	549%	690%	1376%	1358%
%↑in error from nominal to –inertia		454%	507%	804%	680%
%↑ in error from nominal to +inertia	**MAE**	515%	558%	1064%	869%
%↑in error from nominal to –inertia		382%	296%	509%	407%

Table 6.14 Summary of Region 3 percent error increase in RMSE and MAE to payload mismatches. Averaged from 5 trials. Lowest error per case in blue.

		Region 3			
		ANNB	**ALTB**	**HANNB**	**HALTB**
%↑ in error from nominal to +inertia	**RMSE**	328%	323%	268%	343%
%↑in error from nominal to –inertia		224%	193%	218%	192%
%↑ in error from nominal to +inertia	**MAE**	135%	189%	235%	303 %
%↑in error from nominal to –inertia		103%	106%	168%	116%

Table 6.15 Summary of Region 4 percent error increase in RMSE and MAE to payload mismatches. Averaged from 5 trials. Lowest error per case in blue.

		Region 4			
		ANNB	**ALTB**	**HANNB**	**HALTB**
%↑ in error from nominal to +inertia	**RMSE**	387%	365%	402%	458%
%↑in error from nominal to –inertia		301%	247%	280%	251%
%↑ in error from nominal to +inertia	**MAE**	221%	304%	353%	342%
%↑in error from nominal to –inertia		148%	143%	152%	152%

Over all cases in Table 3.12 to 3.15 it is clear that none of the controllers/plants are particularly robust to the payload mismatch. Across all cases the minimum increase in MAE or RMSE was 88%, the maximum 1376% and the average 350%. When inspecting the tables two effects were apparent. First the hybrid controllers/plants typically had larger RMSE error percent increases than the pneumatic mode. Secondly the small move, Region 2, typically resulted in the largest percent error increases across all cases. As the payload mismatch affects the common element, the system acceleration model, it causes a similar magnitude of error in all cases. Cases that previously had the smallest magnitudes of error thus have the largest percent increases, due to this similar error. That is to say, if the same additional error was introduced, the percent increase became larger when the original error was smaller. Also seen across all cases were the trends for the RMSE percent error to increase more than the MAE value, and for both errors to be larger for the +inertia case than for the –inertia case.

In addition to the table summaries of the robustness, examples of a single trial of the -inertia and +inertia loading conditions for vertical cycloidal trajectory tracking are shown in Figures 6.12 and 6.13 respectively. It can be seen in all controllers that, for the –inertia loading condition, the error was primarily biased

towards the negative. This follows since the controller use the nominal payload mass and as such generated too much torque for the decreased actual load. As such the link was typically above the desired trajectory, due to the overcompensation for gravity. This biased the load, regardless of the move direction, since in the 0°-180° range of motion the gravity torque is always opposing positive acceleration. Near 20 seconds and after, where the arm was near 0° and the move was downward, the error changed sign. This is expected as the gravitational load approaches 0 Nm near 0°. Here the torque mismatch was dominated by the torque desired to accelerate the mass downward. Since the model mass was larger than the physical payload mass, too much torque was desired, and the gravitational load (due to position) was too small to bias this error to the negative.

Figure 6.13 shows error examples for the +inertia case, where errors skewed almost entirely positive for the same reason. The position controller desired too little torque for the payload against gravity. Again the gravitational load effect was much larger than the acceleration load effect which was direction dependent. The error sign change seen around 20 s in Figure 6.12 are not seen in 6.13. Though the gravitational load was low near 0° the sign of the torque mismatch led to the general bias of the error being positive for a negative torque move, due to the acceleration effect, with or without gravity. Similarly, a small error sign change, at low gravity can be seen around 5 s, where the move was positive, and the gravity low, for the same reason as in Figure 6.12 near 20 s. In both payload mismatch loading conditions it can be seen that at the steady state holding positions between moves, the system tended towards zero steady state error, as the feedback had more of an opportunity to take effect.

In both cases, as is clear from Tables 6.12 to 6.15, and the Figures 6.12 and 6.13, that the hybrid cases of both controllers led to smaller magnitudes of RMSE and MAE. The low SSE at the dwell positions was achieved through a combination of position/velocity feedback as well the friction compensation as in

(5.17). There were steep error magnitude increases seen at the start of each move (after the dwell positions), caused by the payload mismatched. The acceleration/gravity portions of the position controllers constitute the largest torque component of the position controller output. As such soon as a new move began, a new acceleration and new positions in the trajectory were desired. Since both have mass dependent terms, the payload mismatch between the model and the physical case caused the error to rapidly increases in magnitude until the feedback terms begin to take appreciable effect. Further the integral like portion of friction compensation does not begin until the end of the desired move, where the desired velocity becomes zero again, thus only aiding to reduce error in the steady state dell portions of the overall experiment.

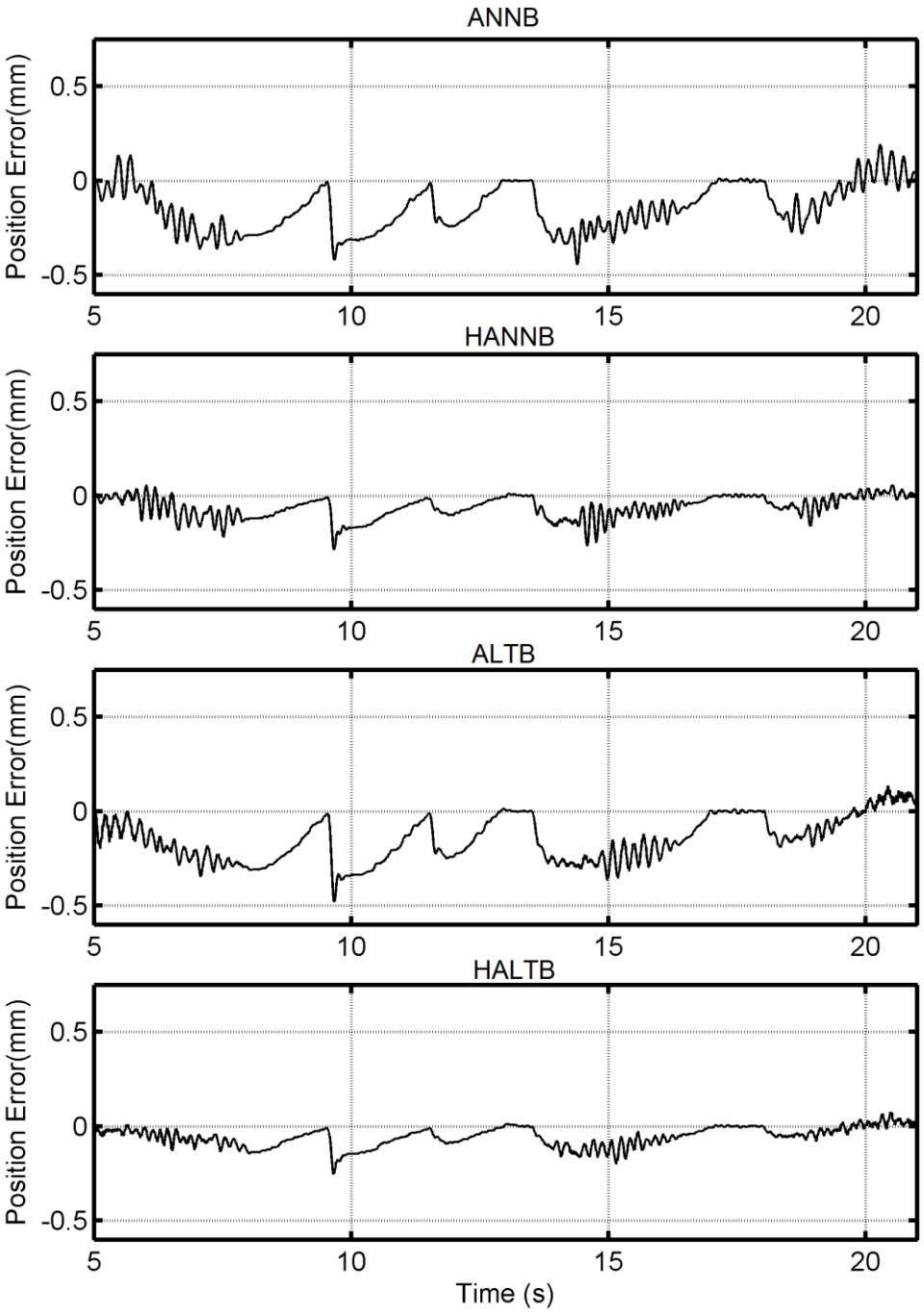

Figure 6.12 Example position error for a typical –inertia robustness trial for each of the four controllers. Top to bottom the controller used was: ANNB, HANNB, ALTB and HALTB. Corresponding to the same trial as the desired trajectory, as in Figure 6.3.

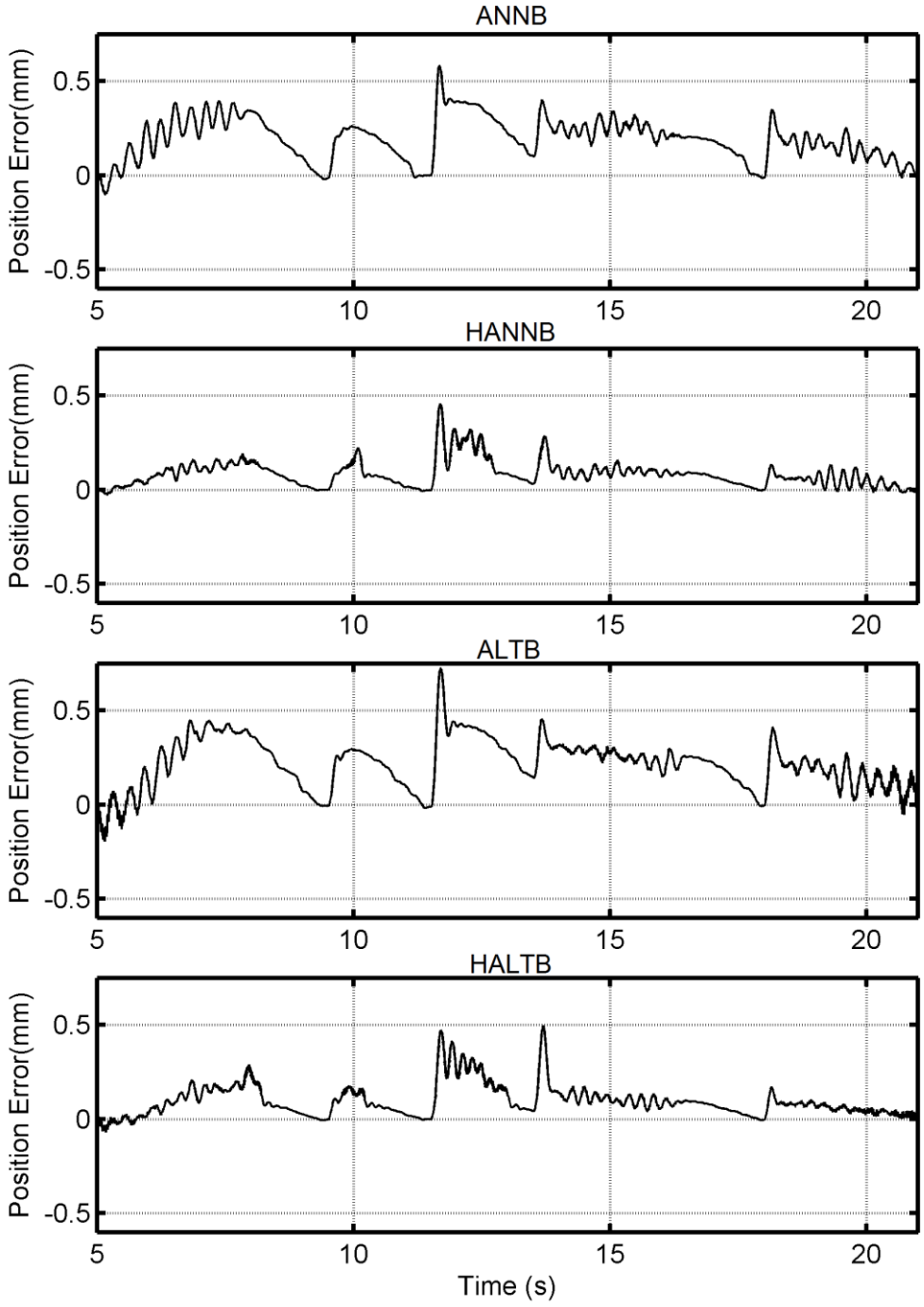

Figure 6.13 Example position error for a typical +inertia robustness trial for each of the four controllers. Top to bottom the controller used was: ANNB, HANNB, ALTB and HALTB. Corresponding to the same trial as the desired trajectory, as in Figure 6.3.

6.6 Model Accuracy

Simulations were not performed in Chapter 5, as such the experimental results could be compared to the ideal simulated controller performance. To evaluate the efficacy of the modeling, and the degree to which the feedback was required, additional analysis of the data from section 6.5 was performed. Specifically, the model based and feedback contributions to the control signals of the position and pressure controllers were extracted and compared.

For the outer position controller, the control signal was the desired torque. It was calculated via (5.18). The acceleration model should contribute the majority of the desired torque, with the proportional and derivative position/velocity error feedback providing a correction for modelling errors and unknown disturbances. The desired torque was broken into the model based and feedback components of the desired torque, the output of the position controller. For ease of comparison, the model based and the total (model based + feedback) torque as plotted. For the Region 1 the 0°-90° portion of the move seen in Figures 6.4, 6.6, 6.8, and 6.10, the desired torque values are plotted in Figures 6.14 and 6.15. The 0°-90° move occurs over the 5-8 s region, where 8 s and onward was a constant 90° dwell desired position.

Figure 6.14 shows the model based and feedback contributions to the desired torque for the same example tests shown in Figure 6.4 and 6.8. Similarly, for the HANNB and HALTB controllers seen in Figures 6.6 and 6.10, the position controller torque components were separated in Figure 6.15. Based on the plots, it can be seen that the model based portion was fairly smooth, and the feedback more oscillatory. The "feedback + model based" represents the value actually used in the controller, with the difference between that and the model based portion being the effect of the feedback terms. The feedback was oscillatory about the model based portion, as was to be expected as error terms change sign. Across all cases the feedback diminished to zero near the end of the plot

move, where the desired position becomes constant and the friction compensation term eliminated the steady-state error, as per (5.17). Inspecting Figures 6.4 to 6.10 it can be seen that little to no steady state error exists at these positions, and the desired velocity is zero. So it follows that the feedback would likewise be small or zero about these positions. The triangular shape seen after 8 s is the effect of the friction compensation slowly taking effect, as in (5.17). The shape is triangular as opposed to a ramp, as the system overshot the holding position. The peak of the triangle corresponds to where the position error changed signs and the friction compensation decreased to push the system towards 0 error. This multi-direction effect of the friction compensation can be seen in figure 6.4 as the small error sign change just before the first steady state error of 0 can be seen, just after 8 s. The amplitude of oscillation seen in the hybrid mode was smaller than that of the pneumatic mode, as less error was present. The smaller RMSEs and MAEs of the hybrid cases, as discussed in section 6.5, means that less feedback was produced or was necessary. Across the all four controller cases it can be seen that the model is fairly accurate, as it provides the large majority of overall desired torque value, with a much smaller percentage provided from the feedback contribution.

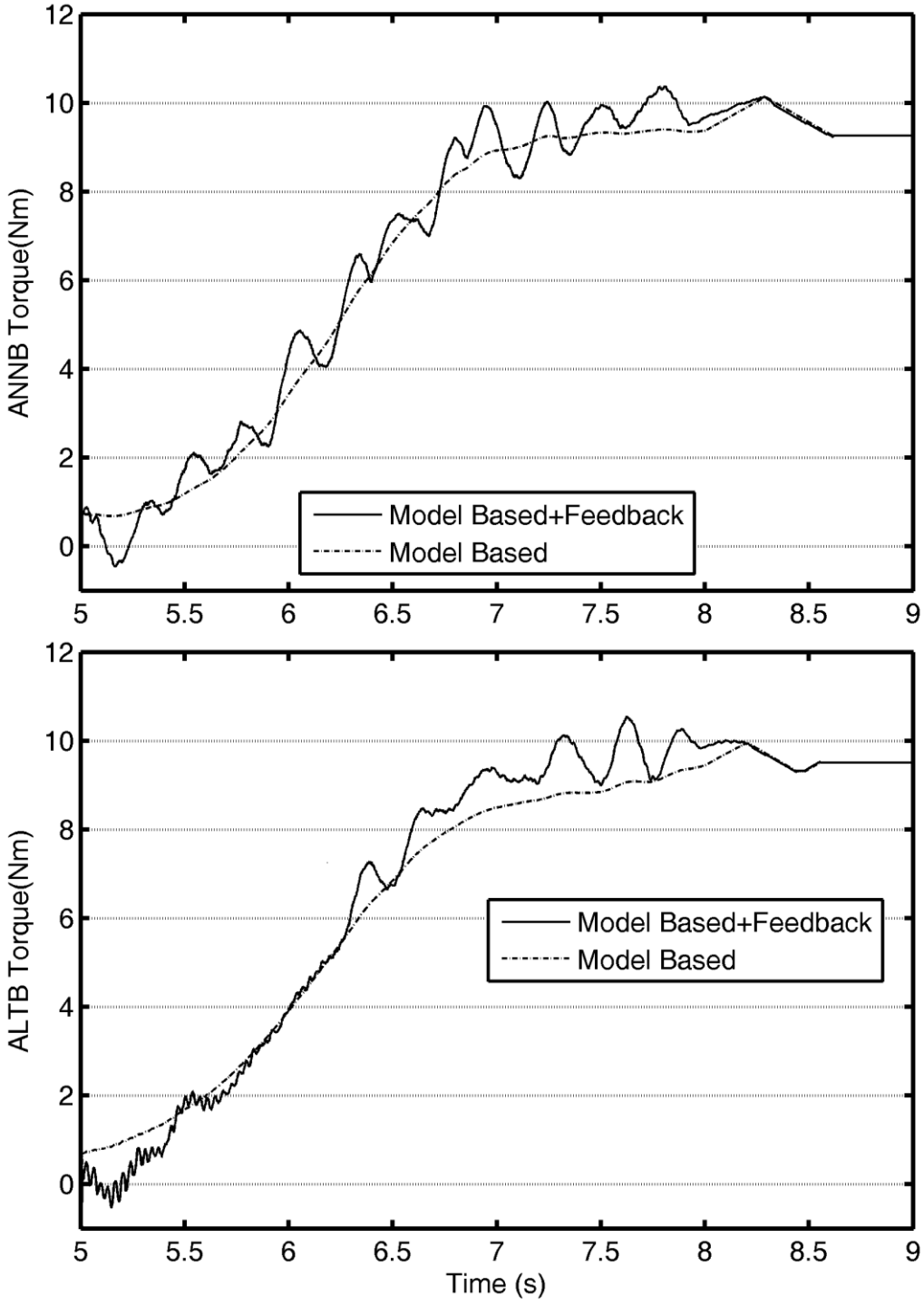

Figure 6.14 Comparison of the model based component of the desired torque, and the feedback portion. Under nominal loading condition. Top: ANNB controller results for Region 1 of Figure 6.4 Bottom: ALTB controller results for Region 1 of Figure 6.8.

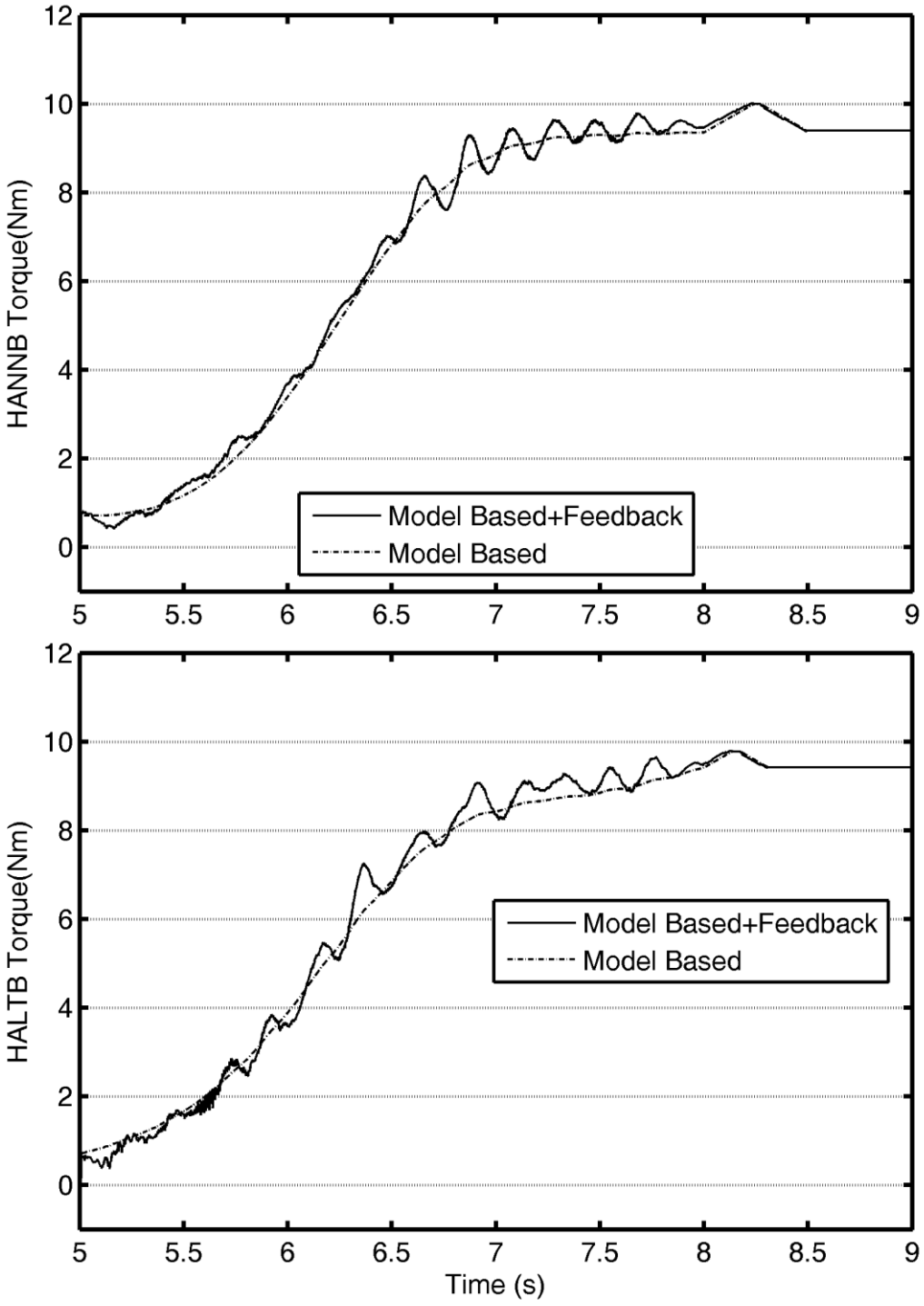

Figure 6.15 Comparison of the model based component of the desired torque, and the feedback portion. Under nominal loading condition. Top: HANNB controller results for Region 1 of Figure 6.6 Bottom: HALTB controller results for Region 1 of Figure 6.10.

For the inner pressure controller the separation of model based contribution and feedback contribution was more complex. In pressure control, the feedback was incorporated via (5.10), the feedback linearization stage, by modifying $\dot{m}_{des}$, and was then used with the IVM ANN to determine the valve duty cycle. To separate the model based contributions from the feedback two separate evaluations were performed. u_{total} was the control signal actually applied to the valve in the experiment and was the model based +feedback result. u_{model} was determined by using (4.35) instead of (5.10), to first calculate $\dot{m}_{model}$. This mass flow rate was then used with the IVM ANN, as in (5.12)/ (5.13), to determine u_{model}. These values, again shown for the Region 1 portion of the moves seen in Figure 6.4 and 6.10, are plotted in Figure 6.16, where the ANN based model could be evaluated. The alternate controller, as expressed by (5.14)/(5.15), had no model based component, and as such just u_{total} for the alternate pressure controller was plotted to provide context for the ANN based duty cycle.

The most apparent difference between the ANN duty cycle and the alternate pressure controller duty cycle was the amplitude of oscillation, which was significantly larger for the alternate pressure controller. This is expected for a non-model based controller. The feedback used in the ANN based pressure controller generally contributed to a larger amplitude of oscillation in the control signal, centered around the same midpoint as the model based contribution, for the majority of the trial. The model based + feedback began to diverge from the model based portion around 6.25 seconds which, as can be seen in Figure 6.14, was where the torque rate of change begins to decrease. The divergence from the model based stabilizes to a fairly constant steady state shift by the end of the trial, where arm was in a dwell state. After 8 s the oscillation across both terms also significantly reduced. This corresponds to the end of 0˚ to 90˚ move, where

the system velocity has significantly decreased. The accuracy of the pressure model is more ambiguous than that of the position controller, though it can certainly be said that portions of the required feedback are quite large, as compared to the model based portion.

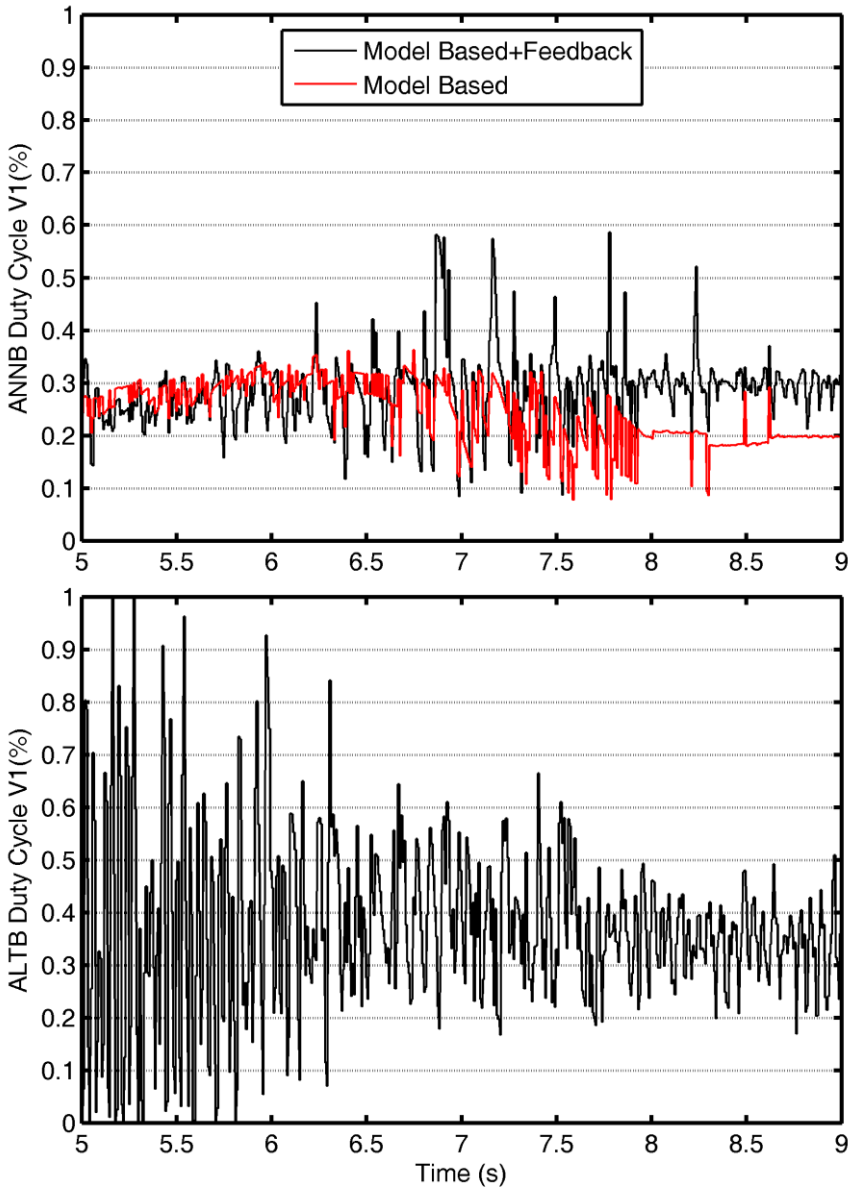

Figure 6.16 Comparison of the model based component of the valve 1 duty cycle, and the feedback portion. Under nominal loading condition. Top: ANN based pressure controller results for Region 1 of Figure 6.4 Bottom: Alternate pressure controller results for Region 1 of Figure 6.8.

6.7 Zero Gravity Experiments

Position control experiments were also performed with a cycloidal trajectory and the system loading analogous to that of a horizontal configuration. As previously discussed the physically horizontal orientation is inconvenient given the limited testing area, and instead the zero gravity loading condition of Table 6.1 is used. In the zero payload case, the torque due to the link's weight is balanced via particular placement of a counterweight. Experiments, data collection and analysis similar to section 6.5 was repeated for the zero gravity loading condition. Again five trials of each combination were performed, analyzed and averaged. The results are summarized in Table 6.11. As discussed in section 6.4, the model mass/inertia and controller gains were retuned for this zero gravity loading condition.

Table 6.16 Zero gravity loading condition cycloidal trajectory position tracking. RMSEs and MAEs averaged across 5 trial results. Lowest error per region and error type marked in blue.

	Region 1: 0°→90° Piston Error (mm)				**Region 2: 90°→91°→90° Piston Error (mm)**			
	ANNB	**ALTB**	**HANNB**	**HALTB**	**ANNB**	**ALTB**	**HANNB**	**HALTB**
RMSE (mm)	0.048	0.055	0.020	0.019	0.015	0.037	0.012	0.011
MAE(mm)	0.198	0.186	0.067	0.063	0.059	0.127	0.035	0.031
	Region 3: 90°→45°→0° Piston Error (mm)				**Region 4: 0°→90°→91°→90°→45°→0° Piston Error (mm)**			
	ANNB	**ALTB**	**HANNB**	**HALTB**	**ANNB**	**ALTB**	**HANNB**	**HALTB**
RMSE (mm)	0.036	0.061	0.017	0.016	0.036	0.055	0.017	0.016
MAE (mm)	0.135	0.196	0.054	0.054	0.198	0.204	0.069	0.063

In the case of the zero gravity loading condition the errors were lower than those seen in the vertical case (compare to Table 6.7), though not substantially so. This is not surprising, as the controller was retuned for the payload, and as such should perform similarly. Comparing the controllers for this loading condition, in all cases the HALTB was the superior controller of the four, although not by a significant margin over the HANNB controller. This is in contrast to the HANNB being slightly better than the HALTB in the nominal payload case (section 6.5). The ANNB is superior in all cases to the ALTB controller. The ANNB/ALTB differences are larger than the HANNB/HALTB differences. This was to be expected as the zero gravity loading condition, which was purely inertial has lower torque requirements than the nominal (or most gravity loaded condition). With a reduced torque requirement the electric motor was capable of providing a larger portion of the torque. As such, it was unsurprising that the hybrid mode controllers have similar results to one another, as the pneumatic portion becomes less dominant.

Table 6.17 shows the percent differences between cases. It can be seen that for most cases the relative errors were in the predicted directions. The only deviation from the expected superior cases was in the HALTB vs HANNB cases, as previously discussed. This table shows more clearly the improvement which the motor introduced to both controllers, in this loading condition. It can be seen that in Region 4, the hybrid operation improves overall performance in RMSE and MAE by significant amounts. The results can be compared to the nominal payload percent changes, as seen in Table 6.8 to 6.11. For Region 4 (Table 6.11), of the nominal payload condition the RMSE percent improvements by operating in the hybrid mode were ANN-to-HANN: 53.1% and ALTB-to-HALTB: 59.9%. In this loading condition the RMSE percent improvements from operating in the hybrid mode were ANNB-to-HANNB: 53.7% and ALTB-to-HALTB: 251%. Where the improvement in ANNB-to-HANNB was similar, the ALTB-to-HALTB was much larger. Similar results can be observed for MAE and RMSE across all

4 regions. Regardless of the magnitude of improvement, it was apparent, as was also seen in the nominal, +inertia, and –inertia loading conditions, that there is a significant improvement to position control when operating in the hybrid mode.

Table 6.17 Summary of percent differences between cases of Table 6.11. Green indicates expected direction of percent error change (*i.e.* decrease in direction indicated). Red indicates increase in error.

	Region 1		Region 2	
	RMSE	**MAE**	**RMSE**	**MAE**
%↓ in error from ALTB to ANN B	13.1%	-1.20%	58.9%	6.70%
%↓ in error from HALTB to HANNB	-2.50%	-7.90%	-8.30%	-13.8%
%↓ in error from ANNB to HANNB	59.2%	65.9%	22.4%	41.3%
%↓ in error from ALTB to HALTB	189%	66.4%	239%	75.8%
	Region 3		**Region 4**	
	RMSE	**MAE**	**RMSE**	**MAE**
%↓ in error from ALTB to ANN B	40.7%	6.00%	33.7%	0.60%
%↓ in error from HALTB to HANNB	-11.2%	-0.50%	-7.70%	-9.70%
%↓ in error from ANNB to HANNB	52.2%	60.0%	53.7%	65.3%
%↓ in error from ALTB to HALTB	292%	72.4%	251%	69.3%

6.8 Sine Trajectory Experiments

Typical trajectories for the purely pneumatic actuators in the literature were step and sine trajectories. These trajectories were commonly used for general control characterization, and were not selected with an application in mind, as the cycloidal was in sections 6.5 and 6.7. To be more comparable to these publications (discussed in section 6.9), the experiments and analysis of section 6.5 and 6.7, were repeated with a sine trajectory. For the GEN2 comparison, the sine wave's neutral position was offset from 0° to be centered on the highest gravity loading condition, *i.e.* 90°. Five experiments each with six cycles of the sine wave, at 0.25 Hz and amplitude of 20 mm (at the piston) were performed, centered at maximum gravity load, *i.e.* 90°. As in section 6.5, the RMSE and MAE

results were calculated individually for each trial and then averaged. An example of the desired trajectory is shown in Figure 6.7. To be more comparable to the literature only the pneumatic mode was used. The summary of the sine results are listed in Table 6.18, and a plot of the position tracking and error of a typical trial shown in Figure 6.17.

Table 6.18 Pneumatic only sine trajectory position tracking, average of 5 trials. Lowest errors per case marked in blue.

		Sine Test Error (mm)	
		ANNB	**ALTB**
Nominal	**RMSE (mm)**	0.060	0.091
Zero Gravity		0.076	0.106
Nominal	**MAE (mm)**	0.165	0.305
Zero Gravity		0.220	0.296

Based on the results listed in Table 6.13, it can be seen that the ANNB performs better than the ALTB controller in all cases for this trajectory. The zero gravity loading condition actual performs more poorly than the nominal condition. The increased error seen in the lower loading condition could be a combination of effects. First, both conditions had an inertial load, but the zero gravity loading condition had a smaller inertia, and had no gravity load (see Table 6.1). As such the overall load is smaller. If the inertia was smaller but the pressure/torque errors were of the same magnitude, the smaller inertia would accelerated more, thus resulting in a larger position error. Secondly, without the gravity load, the rack/pinion gear backlash can have more of an effect. The nominal load has a constant gravity torque in a single direction, which varies with the sine of the position, over the range. Any acceleration desired in the positive direction, acts against the gravity load, save for the 0° degree position. Thus the gear teeth would be loaded on one side, and would remain in contract. If the acceleration

was desired in the negative direction, that is to say the same direction as the gravity load, the gear teeth would come out of contact. If the desired acceleration as large enough, and exceeds the gravity load (which varies with position, being largest at 90° and smallest near 0° or 180°), then the gear teeth could come out of contract until the teeth contact again on their opposite side. The degree of "play" between the gear teeth contacting in each direction is the backlash of the gear. Without a gravitational load this bias is not present and the gear teeth could come out of contact when the desired torque changes direction. In this case the backlash between the gear teeth meshing makes control more difficult.

It can be seen in the error plot of the Figure 6.17 that there was a high and low frequency error component. The low frequency error was of similar frequency as the position tracking, 0.25 Hz. The peaks of the error are close to the peaks of the desired position. This result was not surprising as these points correspond to the desired maximum acceleration, as is shown in Figure 6.2, and thus had a larger torque requirement. Furthermore, these points correspond to a velocity sign change, where the direction of the friction compensation torque changes. The friction compensation step changes from the positive friction compensation value to the negative friction compensation value (recall (5.17)). These combined effects result in the generally larger low frequency error, and the large spikes in error seen at a higher frequency, at these positions.

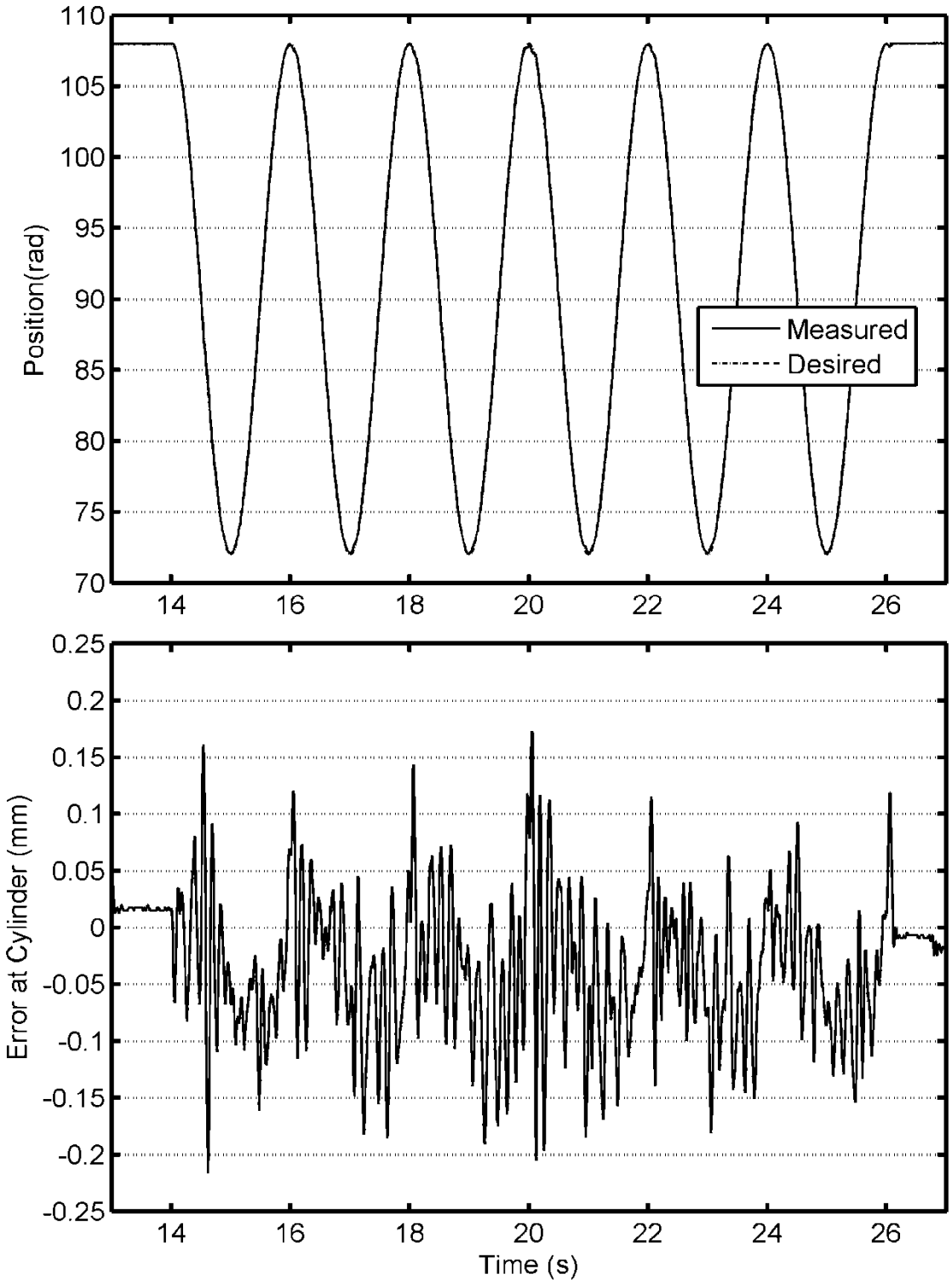

Figure 6.17 Example of typical ANNB controller sine trajectory trial under nominal loading condition, 0.5Hz, 36° (20 mm) amplitude, centered at 90°.

6.9 Position Control Comparison to Literature

6.9.1 Summary of Relevant Prior Art

There were very few HPEAs published in the literature. Many more publications existed for the control of purely pneumatic cylinders. Within this set, there are also very few publications on position controlled pneumatic actuators which produce a rotary output, or move in the vertical plane (with gravity loading). The majority of the actuators move linearly, in the horizontal plane, with only inertial and frictional loads. Regardless of the lack of direct comparability, it was worthwhile exploring the prior art of purely pneumatic actuators, as well as HPEAs, to provide more context to the magnitudes of errors in the GEN2 as seen in sections 6.5, 6.7 and 6.8. Table 6.19 summarizes a variety of actuators, configurations, trajectories and their position tracking results from the prior literature. These publications are discussed in more detail in Chapter 2.

Table 6.19 Summary of prior art configuration and performance.

Paper	**Configuration**	**Trajectory**	**Error Results**
van Varseveld & Bone, (1997)	Horizontal, double acting, single rod pneumatic cylinder, solenoid valves. 0.94 kg mass	S-Curve: 64 mm, 2 s	SSE: 0.21 mm MAE: 2 mm Robustness: Same SSE for steps even with 600% mass mismatch.
Takemura *et al.,* (2000)	Horizontal Pneumatic motor, proportional valves coupled with DC motor as hybrid. 1.5 kg mass	Sine: 200° PTP 0.5 Hz	Pneumatic MAE: ~17.5° Hybrid MAE: ~9°
Shen *et al.,* (2006)	Horizontal, double acting, single rod pneumatic cylinder, solenoid valves 10 kg mass	Sine: 40 mm PTP 0.25Hz 0.5 Hz 1 Hz	 MAE: >2mm MAE: >3mm MAE: ~4mm

Nguyen *et al.,* (2007)	Horizontal Double acting rodless pneumatic cylinder, solenoid valves. 2 kg mass	Sine: 40 mm PTP 0.5 Hz Step: 40 mm	MAE: ~2mm SSE: 0.1 mm
Rao & Bone, (2008)	Horizontal, double acting, single rod pneumatic cylinder, proportional valves. 1.5 kg mass	S Curve: 20 mm, 1 s Sine: 35 mm PTP 1HZ	MAE: ~0.3 mm RMSE: 0.074 mm MAE: 0.5 mm RMSE: 0.136 mm Robustness: With 52% increase in mass, RMSE increased by 5%. With 39% reduction in mass, system became unstable.
Shin *et al.,* (2009)	Vertical Antagonistic PAMs in parallel with an electric motor for hybrid operation	Sine: 10° PTP 6 Hz	Pneumatic MAE: <1° Hybrid MAE: <0.25°
Hodgson *et al.,* (2012)	Horizontal, double acting, single rod pneumatic cylinder, solenoid valves 0.9 kg mass plus constant external loading via pulley.	Sine: 40 mm PTP: 0Nm ext. 0.5 Hz 4.9Nm ext. 0.5 Hz 9.8Nm ext. 0.5 Hz	RMSE: ~0.5 mm ~0.6 mm ~0.75 mm
Carneiro, (2012b)	Horizontal, double acting, single rod pneumatic cylinder, proportional valves. 5.9 kg	Sine: 300mm PTP 2 Hz	MAE: ~6 mm
Bone & Chen, (2012)	Vertical, double acting, single rod pneumatic cylinder, solenoid valves. With electric motor as hybrid system. 17.1 kg equivalent mass	Cycloidal: 75 mm (115°), 4 s Sine: 80 mm PTP, 1 Hz	**Pneumatic Only:** MAE: 1.9 mm SSE: <0.1 mm **Hybrid** MAE: 0.3 mm SSE: <0.1 mm **Hybrid** MAE: 0.9mm

Teramae *et al.,* (2013)	Vertical, Single PAM in parallel with electric motor for hybrid operation 2.5 kg at 0.4 m	Sine: 28.6° PTP, 2 Hz	**Hybrid** MAE: ~5.7°
Bone, Xue, & Flett, (2015)	Vertical, double acting single rod pneumatic cylinder, solenoid valves. With electric motor as hybrid system. With no payload: 0.432 kg arm of length 0.43 m	Cycloidal: 2.85s to 90°(47.1 mm) Hold for 2.3 s, 2.85s return to 0	**Pneumatic Only:** RMSE: 0.64° (0.34 mm) SSE: 0.23°(0.12 mm) **Hybrid:** RMSE: 0.11° (0.06 mm) SSE: 0.04° (0.02 mm) <u>90% Payload Mismatch</u> <u>No Payload Estimator</u> **Pneumatic Only:** RMSE: 3° (1.57 mm) SSE: 3.61° (1.89 mm) **Hybrid** RMSE: 1.83° (0.96 mm) SSE: 1.26° (0.66 mm) <u>With Payload Estimator</u> **Pneumatic Only:** RMSE: 0.69° (0.36 mm) SSE: 0.28° (0.15 mm) **Hybrid** RMSE: 0.33° (0.17 mm) SSE: 0.04° (0.02 mm)
Ramhuzaini, He, & Sepehri, (2015)	Vertical, double acting single rod pneumatic cylinder, proportional valves. 9 kg (linkage torque transmission)	Sine: 200 mm PTP, 0.1 Hz S curve 10 mm 2.5 s Sine: 200 mm PTP, 0.1 Hz S curve 10 mm 2.5 s	MAE: ~5 mm RMSE: 1.94 mm MAE: ~5 mm RMSE: 1.11 mm SSE: 0.53 mm <u>50% Payload Mismatch</u> MAE: ~5 mm RMSE:1.42 mm MAE: ~4 mm RMSE: 0.96 mm SSE: 0.53 mm
Hodgson *et al*., (2015)	Horizontal, double acting, double rod, four 3 way solenoid valves. 0.9 kg nominal,	Saw-Tooth: 70 mm PTP, 2 s ramps	RMSE: 1.06 mm <u>56% Payload Mismatch</u> RMSE: 1.28 mm <u>111% Payload Mismatch</u>

	1.4 kg and 1.9 kg for mismatch.		RMSE: 1.53 mm

The position tracking performance of the GEN2 system is difficult to compare to commercially available purely electric robots. Typically these robot specifications list only the repeatability of the positioning of the end effector, that is to say the repeatability of the steady state error of the system. As the commercial robots have multiple joints, the overall error is a compounding of the errors of each of the actuators through the system. Whereas the GEN1 has only one joint at which the error can occur at. For example, the UR5 robot (Table 3.1) has a repeatability of ±0.1 mm (Universal Robots, 2015), and a reach of 0.85 m. The Baxter robot on the other hand has an accuracy of 10 mm and a reach of 1.21 m (Guizzo & Ackerman, 2012). As can be seen in Figures 6.4, 6.6, 6.8, and 6.10 the GEN2 system is capable of achieving a SSE of zero (based on the position sensed by the encoder) at the holding positions. Assuming the encoder quantization is the only source of error, this means that the SSE is at worst ±½ encoder count, *i.e.* ±0.0000373 Rad. Assuming mechanical deflections do not contribute to the repeatability, this encoder error corresponds to a GEN2 HPEA repeatability of ±0.033 mm at a 0.85 m reach, and ±0.048 mm at a 1.21 m reach. Errors are larger during motions but are rarely reported by robot manufacturers. To compare MAE or RMSE, experiments would need to be performed with the commercial robots.

6.9.2 Sine Trajectory Comparison to Purely Pneumatic Literature

The majority of the purely pneumatic systems in the literature were experimentally validated using a sine trajectory. These results, as summarized in Table 6.19, were compared to the experimental results of sine testing with the GEN2 system operating in the pneumatic mode, as discussed in section 6.8. It

should be noted that the papers cited utilized a variety of different pneumatic cylinders, many with much higher friction values and much smaller payloads. Additionally some of the publications use the more easily controllable proportional valves instead of solenoid valves. The specific type of valve, and other pneumatic components also vary from publication to publication. Further, a variety of other amplitudes, frequencies, pressures and payloads were used across all of these prior experiments. As such the errors listed in Table 6.19 serve primarily to illustrate the order of magnitudes of errors to be compared to the GEN2 system. The results in the literature pertaining to sine moves were compared to the GEN2 system values in Table 6.18, focusing on the nominal loading condition. From Table 6.18 the smallest errors were 0.060 mm RMSE and 0.165 mm MAE, both found in the ANN based controller. In Table 6.19 it can be seen that the GEN2 actuator, operating even in the solely pneumatic mode was capable of better performance than any of the cited publications, despite the GEN2s increased load. The GEN2 system was tested in the vertical, where the gravitational torque is the most significant, though an inertial component does exist. The majority of systems listed in Table 6.19 operate in the horizontal plane. As such they have no gravitational load, and simply accelerate a mass (listed in the table) linearly. For comparison, in the nominal loading condition the GEN2 actuator has a rotational inertia of 0.569 kgm^2, which, through the pinion gear is seen by the cylinders as equivalent to a 573 kg mass to be accelerated in the horizontal. This is significantly larger than any of the payloads used in the literature, and was accelerated with the addition of the gravitational load.

Of the publications which report RMSE (most only reported MAE) for the sine trajectories, the GEN2 system again reported lower values than that of the prior art which used sine trajectories. The results of the sine testing comparison make apparent that the GEN2 system is capable of high accuracy position control for a pneumatically actuated system.

6.9.3 Blended Curve Trajectory Comparison to Purely Pneumatic Literature

Selections of the prior art used "S-curves", blended moves similar to the cycloidal move. In these cases a point-to-point move is performed with a ramp trajectory with blended starts and ends. This blending achieved the same goal of the cycloidal, to avoid commanding infinite acceleration at the step changes in velocity. The smoothing was typically accomplished by polynomial blends. Most of these prior experiments only reported MAE and SSE for the endpoint. These results are most comparable to the cycloidal move results. Recall from Table 6.2, for Region 1, with the nominal payload condition, operating in the vertical, the 0° to 90° move achieved, with the ANNB controller/plant, an RMSE of 0.053 mm with an MAE of 0.164 mm. Comparing these values to all S-Curves of the prior art, a lower MAE was observed for the GEN2 system, which is desirable. Compared to those few publications which reported RMSE, the GEN2 actuator again returned lower error values, even operating in its pneumatic mode. The closest S-curve error values to the GEN2 system's are that of Rao & Bone (2008). Hodgson *et al.* (2015) used a saw-tooth trajectory, acts like a square wave with ramp increases and decreases (unblended). Though the magnitudes of error were much larger than the GEN2, the SMC used had good robustness, with a 111% payload mismatch increasing error by only 44%.

6.9.4 Comparison to Hybrid Pneumatic-Electric Actuator Literature

Takemura *et al.* (2000) was a more unique case with merit for discussion, as it as an alternate type of HPEA. The results were reported in degrees at the output shaft, as all components were rotary. Similarly, Shin *et al.* (2009) was a third type of HPEA which also reported error in degrees. As such the GEN2 could be compared by considering the tracking errors in degrees at the output shaft, recalling the pinion gear radius (r_{gear} =0.0315 m). The GEN2 pneumatic mode errors reported in Table 6.7, can be expressed in degrees as an RMSE and an

MAE 0.12° and 0.30° respectively. The GEN2 actuator certainly performs better than that of Takemura *et al.* (2000). The GEN2 also performs much better than Shin *et al.* (2009) in the pneumatic mode and similarly in the hybrid mode. Unfortunately they did not report the average MAE, and the value used for this comparison was estimated from their plot. Finally Teramae *et al.* (2013) also reports error in degrees for their HPEA. It should be noted that this system behaved more as a controlled pendulum than like that of a robotic arm, and was not designed as a precision position controller (see Chapter 2 for more details). Regardless, the GEN2 system, even in the pneumatic mode, significantly outperforms this system in the sine trajectory.

The most relevant results of the literature are those of Bone & Chen(2012) and Bone, Xue, & Flett (2015), both of which used cycloidal trajectories, operate in the vertical plane, and use the GEN1 actuator, used both in hybrid and purely pneumatic modes. The results of GEN 2 system, operating in the vertical for cycloidal moves are summarized in Table 6.7 and were compared to the results of the GEN1, summarized in Table 6.19. Compared to Bone & Chen(2012), the GEN2 reports lower MAE for the nominal case of both the hybrid and pneumatic modes, though of similar performance for the hybrid mode at least. Compared to Bone, Xue, & Flett (2015), the RMSE reported by the GEN2 in the hybrid and pneumatic modes is superior. For example the GEN2, for Region 1 achieves an RMSE of 0.053 mm for the ANNB and 0.026 mm for the HANNB. Bone, Xue & Flett (2015) reported an RMSE of 0.34 mm in purely pneumatic and 0.06 mm for hybrid mode in a similar cycloidal move.

Bone, Xue, & Flett (2015), also compared its tuned/nominal payload to a 90% inertia mismatch to evaluate robustness. Two controllers were presented, one with a payload estimation subcomponent and one without. For the GEN2 system, recalling the discussion of robustness and Table 6.12, a comparison of the robustness results is presented in Table 6.20. As can be seen, without a

payload estimator incorporated into the controller, the GEN1 and GEN2 achieve similar robustness.

Table 6.20 Comparison of robustness results between GEN1 and GEN2 .

	GEN 2 Actuator 38% mismatch	**GEN 1 Actuator Without Estimator 90% mismatch**	**GEN 1 Actuator With Estimator 90% mismatch**
% Increase in Pneumatic RMSE	333%	369%	8%
% Increase in Hybrid RMSE	304%	1564%	200%

6.10 Conclusion

The GEN2 system was evaluated primarily for the cycloidal trajectory, a smooth trajectory suitable for practical robotic operation. Operating in the pneumatic mode, the ANNB controller was compared to the ALTB controller and in most cases the ANNB improved performance over the alternate. The hybrid operation mode illustrated a clear improvement in both RMSE and MAE over the non-hybrid actuation for both pressure controllers. For the cycloidal trajectories, over both the ANNB and the ALTB controllers, the hybrid mode improved over the pneumatic mode testing in the RMSE by an average of 55% and the MAE by an average of 40%. Sinusoidal comparison of the GEN2's pneumatic mode as compared to purely pneumatic actuators in the literature showed at least comparable performance to all surveyed and superior performance to most. This superiority would be further improved by hybrid actuation as indicated by the nominal payload evaluation of the four controller types.

Overall the system performed well for position tracking with a known payload compared to the GEN1 actuator while simultaneously meeting the goal of increased load capacity. Bone, Xue, & Flett (2015), using the GEN1 actuator investigated robustness improvements via a payload estimator which improved GEN1 performance, and was superior to the GEN2 in robustness. Improvement of the robustness GEN2 is quite likely possible by implementing additional or alternate controllers including such elements as a payload estimator. Overall the GEN2 actuator produced superior position tracking results with the developed controllers. Further it will be a superior test-bed, as compared to the GEN1 actuator, for future research for both pneumatic and hybrid actuation.

Chapter 7 – Conclusions

7.1 Summary

An improved hybrid pneumatic electric actuator was designed, built, and tested. The GEN2 actuator was based on extending the GEN1 actuator developed by Chen (2012) while addressing the capacity limitations and improving on elements of mechanical design. A system model was built to express the dynamics of the system. An inverse valve model was created using an ANN. Using the system acceleration model and sensor feedback an outer loop position controller was developed. An ANN based inner loop pressure controller was also developed based around the inverse valve model, with feedback incorporated via a feedback linearization scheme. To compare to the ANN based controller, an alternate pressure controller was developed using proportional, derivative and feed-forward terms, and incorporated into the outer loop position controller. The controller parameters were experimentally tuned. The system was experimentally evaluated to establish the actuator performance with the various controllers and loading conditions for position trajectory tracking experiments. System robustness was also evaluated by introducing payload mismatch. Experiments were performed in the vertical plane, where significant gravitational loading occurs. Additional experiments were performed using a counterweight to balance gravity resulting in purely inertial loading. These validation experiments were performed with purely pneumatic actuation, as well as hybrid actuation. Both the ANN based controller and the alternate controller yielded small position tracking errors. The ANN based controllers had the better performance in both pneumatic mode and hybrid mode tests for vertical cycloidal trajectories. In all experiments performed, operating in the hybrid mode improved the position tracking performance. A comparison to relevant results from the literature found that the GEN2 actuator achieved superior performance.

7.2 Achievements

The achievements of this research can be summarized as:

1. An improved prototype hybrid pneumatic electric actuator was developed, based on similar concepts to the GEN1 system of Chen (2012). The GEN2 actuator increased system continuous torque by 511% to 39.1 Nm (41.8 Nm peak), while increasing inertia by only 292% to 0.0862 kgm^2. The mechanical design of the GEN2 actuator was also much more physically robust than the GEN1, and is expected to have fewer maintenance issues. The GEN2 system met all four goals, as described in Chapter 1. As such GEN2 system will be a suitable and superior test-bed for further research into collaborative robotics as well as pneumatic, and hybrid pneumatic electric actuator control.
2. The GEN2 actuator, for a vertical sine trajectory using the ANN based controller and operating in the pneumatic mode, achieved better position tracking performance to all purely pneumatic systems reviewed, despite them having much lower inertial loads and typically operating without gravity loading. Compared to the other hybrid systems evaluated, pneumatic motor or PAM based, the GEN2 system again achieved superior performance. Comparing the pneumatic and hybrid vertical cycloidal testing to the GEN1 system, the GEN2 achieved better position tracking performance for both the pneumatic and hybrid operating modes. For example, the GEN2, for Region 1 achieved an RMSE of 0.053 mm for the pneumatic mode and 0.026 mm for the hybrid mode, whereas Bone, Xue & Flett (2015) reported an RMSE of 0.34 mm in pneumatic mode and 0.06 mm for hybrid mode for a similar cycloidal move.

3. In all experiments performed with the GEN2 system, superior performance was found with the hybrid operating mode over the purely pneumatic mode. For a nominal payload and a 90° cycloidal move, the GEN2 achieved for the hybrid mode an RMSE of 0.026 mm (0.05%) and MAE 0.098 mm (0.20%) as seen at the cylinder position. For the purely pneumatic mode an RMSE of 0.053 mm (0.11%) and MAE 0.164 mm (0.33%). For a nominal payload and a 1° cycloidal move, the GEN2 achieved for the hybrid mode an RMSE of 0.01 mm (1.8%) and MAE 0.04 mm (7.3%) as seen at the cylinder position. For the pneumatic mode an RMSE of 0.038 mm (6.9%) and MAE 0.119 mm (22%). For vertical cycloidal testing, using the hybrid mode reduced position tracking RMSE by an average of 55% and MAE by an average of 40%.

7.3 Recommendations for Future Work

Throughout the development and evaluation of the GEN2 actuator several limitations and improvements to be noted for future work became apparent. Additionally, suggestions as to the areas of investigation for which the GEN2 actuator might be used were also considered. These findings were:

1. A vast improvement was seen in the robustness of the GEN1 actuator in Bone, Xue, & Flett (2015) through the inclusion of a payload estimation algorithm. When the GEN1 system did not incorporate the estimator its robustness was poor, similar to the GEN2's. Due to the system similarities it is quite likely that the incorporation of such a payload estimator could vastly improve GEN2's robustness to payload mismatch.
2. The position controller used was relatively simple, and a variety of different controllers, including the discrete value model predictive control of (Bone, Xue, & Flett 2015), or one of the many sliding mode controllers should be

compared to find the best controller for the system. The GEN2 system was developed so that further and alternate control methods for pneumatic and hybrid actuators could be investigated. Using the GEN2 system, with its improved torque capacity and mechanical reliability will allow for control development and testing with loads comparable to those seen in commercially available collaborative robots.

3. The system was designed with larger payloads in mind and should be experimentally compared to commercially available electric motor plus gearing based robot arms being marketed as collaborative robots. These systems could be evaluated in impact testing to evaluate the relative improvement in the inherent safety with the hybrid pneumatic-electric actuators. Further collaborative robotics and human safety research could be evaluated with the possible inclusion of additional safety features such as the incorporation of compliant coverings or novel sensor technologies.
4. The next generation (GEN3) of hybrid actuator developed should focus on a multiple degree of freedom (multi-DOF) system where the difficulties of actuating multiple joints must be considered. With a multi-DOF system more complex trajectories and human safety experiments could be performed.

References

ABB. (2015). "YuMi – Creating an automated future together", < http://new.abb.com/products/robotics/yumi>

Ahn, K., & Yokota, S. (2005). "Intelligent switching control of pneumatic actuator using on/off solenoid valves", *Mechatronics*, *15*(6), pp 683–702.

Anadan, T., (2013). "Safety and control in collaborative robotics". Aug, 2015. <http://www.controleng.com/single-article/safety-and-control-in-collaborative-robotics>

ANSI/RIA (2012). "ANSI/RIA R15.06-2012: American National Standard for Industrial Robots and Robot Systems – Safety Requirements" <https://www.iso.org/obp/ui/#iso:std:iso:8373:ed-2:v1:en>

Bobrow, J. E., & Mcdonell, B. W. (1998). "Modeling , Identification , and Control of a Pneumatically Actuated, Force Controllable Robot", *IEEE Transactions on Robotics and Automation*, *14*(5), pp 732–742.

Bone, G. M., & Chen, X. (2012). "Position Control of Hybrid Pneumatic-Electric Actuators", *2012 American Control Conference*, Montreal, Canada, pp 1793–1799.

Bone, G. M., Xue, M., & Flett, J. (2015). "Position control of hybrid pneumatic–electric actuators using discrete-valued model-predictive control", *Mechatronics*, *25*, pp 1–10.

CAN/CSA (2014). "CAN/CSA-Z434-14: Industrial Robots and Robot Systems" <http://shop.csa.ca/en/canada/industrial-robotics/cancsa-z434-14/invt/27017992014>

Carneiro, J., and Almeida, F., (2006), "Pneumatic Servovalve Models Using Artificial Neural Networks", *Proceedings of the Bath Symposium on Power Transmission and Motion Control*, Bath, UK, pp. 195–208.

Carneiro, J., & de Almeida, F. (2012a). "A Neural Network Based Nonlinear Model of a Servopneumatic System", *Journal of Dynamic Systems, Measurement, and Control*, *134*(2), pp 1-8.

Carneiro, J., & de Almeida, F. (2012b). "A high-accuracy trajectory following controller for pneumatic devices", *The International Journal of Advanced Manufacturing Technology*, *61*(1-4), pp 253–267.

Chen, X. (2012). "Development of a Hybrid Pneumatic-Electric Actuator", (Master's Thesis). Retrieved from MacSphere Database. (http://hdl.handle.net/11375/11890)

Guizzo, E. & Ackerman, E. (2012). "The Rise of the Robot Worker", *IEEE Spectrum*, 49(10), pp 33-41.

Hodgson, S., *et al*. (2012). "Improved tracking and switching performance of an electro-pneumatic positioning system", *Mechatronics*, *22*(1), pp 1–12.

Hodgson, S., *et al*. (2015). "Nonlinear Discontinuous Dynamics Averaging and PWM-Based Sliding Control of Solenoid-Valve Pneumatic Actuators", *IEEE/ASME Transactions on Mechatronics, 20*(2), pp 876–888.

ISO (2011). "ISO 10218-1:2011(en): Robots and robotic Devices – Safety Requirements for Industrial Robots – Part1 Robots" <https://www.iso.org/obp/ui/#iso:std:iso:8373:ed-2:v1:en>

ISO (2014). "ISO 8373:2012(en): Robots and Robotic Devices - Vocabulary" <https://www.iso.org/obp/ui/#iso:std:iso:8373:ed-2:v1:en>

Kawada Industries, (2015). " Next Generation Industrial Robot Nextage" Aug, 2015 <http://nextage.kawada.jp/en/specification/>

Kuka (2015) "LBR iiwa" Aug, 2015 <http://www.kukahealthcare.com/NR/rdonlyres/310A3034-1F44-47D7-8B37-F681BFCF7757/0/db_LBRiiwa_en.pdf>

McCloy, D., & Martin, H. (1980), "Control of Fluid Power: Analysis", New York, USA:Ellis Horwood Limited

Mills, J. K. (1990). "Hybrid Actuator for Robot Manipulators: Design, Control and Performance", *1990 IEEE International Conference on Robotics and Automation*, Cincinnati, USA, pp 1872-1878.

Misumi USA, (2015). "Ball Rollers – Hex Head, Stud Type" Aug, 2015 < http://us.misumi-ec.com/vona2/detail/110300427550/>

Nguyen, T., *et al*. (2007) "Accurate Sliding-Mode Control of Pneumatic Systems Using Low-Cost Solenoid Valves", *IEEE/ASME Transaction on Mechatronics*, 12(2), pp 216-219.

Ning, S. & Bone, G. M. (2005). "Development of a Nonlinear Dynamic Model for a Servo Pneumatic Positioning System", *Proceedings of the IEEE International Conference on Mechatronics & Automation*, Niagara Falls, Canada, pp 43–48.

Petrosky, J. (1998), "Hybrid Electro-Pneumatic Robot Joint Actuator", U.S. Patent 478225828, November 1988.

Ramhuzaini, A., He, L., & Sepehri, N., (2015) : "Design and experimental study of a dynamical adaptive backstepping–sliding mode control scheme for position tracking and regulating of a low-cost pneumatic cylinder", *International Journal of Robust and Nonlinear Control*.

Rao, Z., & Bone, G. M. (2008). "Nonlinear Modeling and Control of Servo Pneumatic Actuators", *IEEE Transactions on Control Systems Technology, 16*(3), pp 562–569.

Rethink Robotics, (2015a). "Baxter Tech Specs". Aug, 2015. <http://www.rethinkrobotics.com/baxter/tech-specs/>

Rethink Robotics, (2015b). "Baxter Research Robot: Hardware Specifications". Aug, 2015. <http://sdk.rethinkrobotics.com/wiki/Hardware_Specifications>

Richer, E., & Hurmuzlu, Y. (2000a). "A High Performance Pneumatic Force Actuator System : Part I — Nonlinear Mathematical", *ASME Journal of Dynamic Systems, Measuremnet, and Control*, *122*(3), pp 416-425.

Richer, E., & Hurmuzlu, Y. (2000b). "Force Actuator System : Part II — Nonlinear Controller Design", *ASME Journal of Dynamic Systems, Measurement, and Control*, *122*(3), pp 426-434.

Shearer, J. (1956). "Study of Pneumatic Processes in the Continuous Control of Motion With Compressed Air – I", *Transactions of the ASME*, 78, pp 233-242.

Shen, X., Zhang, J., Barth, E., & Goldfarb, M. (2006). "Nonlinear Model-Based Control of Pulse Width Modulated Pneumatic Servo Systems", *Journal of Dynamic Systems, Measurement, and Control*, *128*(3), pp 663-669.

Shin, D., *et al*. (2009). "Design Methodologies of a Hybrid Actuation Approach for a Human-Friendly Robot", 2009 *IEEE International Conference on Robotics and Automation*, pp 4369–4374.

Shin, D., *et al*. (2010). "Analysis of Torque Capacities in Hybrid Actuation for Human-Friendly Robot Design", 2010 *IEEE International Conference on Robotics and Automation*, pp 799–804.

Slotine, J., & Li, W. (1991), "Applied Nonlinear Control", New Jersey, USA: Prentice Hall

Song, C., *et al.* (2015). "Modeling of pneumatic artificial muscle using a hybrid artificial neural network approach", *Mechatronics*, Available online: June, 29, 2015.

Spong, M., & Vidyasagar, M. (1989), "Robot Dynamics and Control", New York, USA:Wiley

Takemura, F., *et al*. (2000). "Control of a Hybrid Pneumatic / Electric Motor", *Proceedings of the 2000 IEEE/RSJ International Conference on Intelligent Robots and Systems, 1*, pp 209–214.

Teramae, T., *et al*. (2013). "Modeling and Control of A Pneumatic-Electric Hybrid System", *2013 IEEE/RSJ International Conference on Intelligent Robots and Systems*, pp 4887–4892.

Texas Instruments, (2013). "LM1949 Injector Drive Controller (Rev. C)" Aug, 2015 < www.ti.com/lit/ds/symlink/lm1949.pdf>

Thermo-CRS (2002). "F3 Robot System User Guide".

Universal Robots, (2015). "Products from Universal Robots". Aug, 2015. <http://www.universal-robots.com/products/>

van de Vegte, J., (1986). "Feedback Control Systems", Upper Saddle River, NJ, USA: Prentice-Hall.

van Varseveld, R. & Bone, G. M. (1997). "Accurate Position Control of a Pneumatic Actuator Using On / Off Solenoid Valves", *IEEE/ASME Transactions on Mechatronics*, *2*(3), pp 195–204.

Zinn, M., Roth, B., Khatib, O., & Salisbury, J. K. (2004). "A New Actuation Approach for Human Friendly Robot Design", *The International Journal of Robotics Research*, *23*(4), pp 379–398.

Appendix A – Shaft Design

Using AutoDesk Inventor 2014's shaft analysis tool, the shaft was refined to the appropriate diameters given the geometry of parts to be mounted as well as the final stress state in shaft. Recall Figure 3.X, for a profile of the shaft. Table A.1 summarizes the material properties and analysis conditions used. Table A.2 summarizes the loads and their locations. Table A.3 summarizes the two support positions, 1: the pinion gear(to rack gear to ball roller), and 2: the back to back angular contact bearing set. Table A.3 summarizes the results of the various maximum stresses in the shaft. The maximal reduced stress is the largest stress combination seen in the shaft using the HMH (Huber – Misis - Hencky) criterion. Figures A.1 to A.10 show the relevant stresses and deflections in the shaft. The worst case stress has a factor of safety of 2.6 from the yield point of the material, as such the shaft diameters selected were sufficient. The maximum deflection is 0.275 µm, and maximum rotational deflection is 0.17 degrees.

Table A.1 Analysis Properties.

Material	1045 Steel
Modulus of Elasticity	200 GPa
Modulus of Rigidity	80 GPa
Tensile Strength, Yield	565 MPa
Tensile Strength, Ultimate	310 MPa
Density	7860 kg/m^3
Shear Displacement Ratio	1.188 ul
Number of Divisions	1000 ul
Mode of reduced stress	HMH

Table A.2 Loading conditions.

Index	Location (mm)	Radial Force (N)	Axial Force (N)	Torque (Nm)	Deflection (µm)
					Y
1	5.5			4	-0.091
2	34.5			42	-0.000
3	91.5			-46	-0.178
4	91.5		-40		-0.178
5	91.5	40			-0.178

Table A.3 Support Conditions.

Index	Type	Location (mm)	Reaction Force (Nm)	
			Y	Axial Force
1	Free	34.5 mm	-16.098 N	
2	Fixed	74.5 mm	58.028 N	-40.000 N

Table A.4 Analysis Results.

Maximal Bending Stress	0.874 MPa
Maximal Shear Stress	0.562 MPa
Maximal Torsional Stress	69.415 MPa
Maximal Tension Stress	0.127 MPa
Maximal Reduced Stress	120.232 MPa
Yield Factor of Safety to Maximal Reduced Stress	2.6
Maximal Deflection	0.275 µm
Angle of Twist	0.17 deg

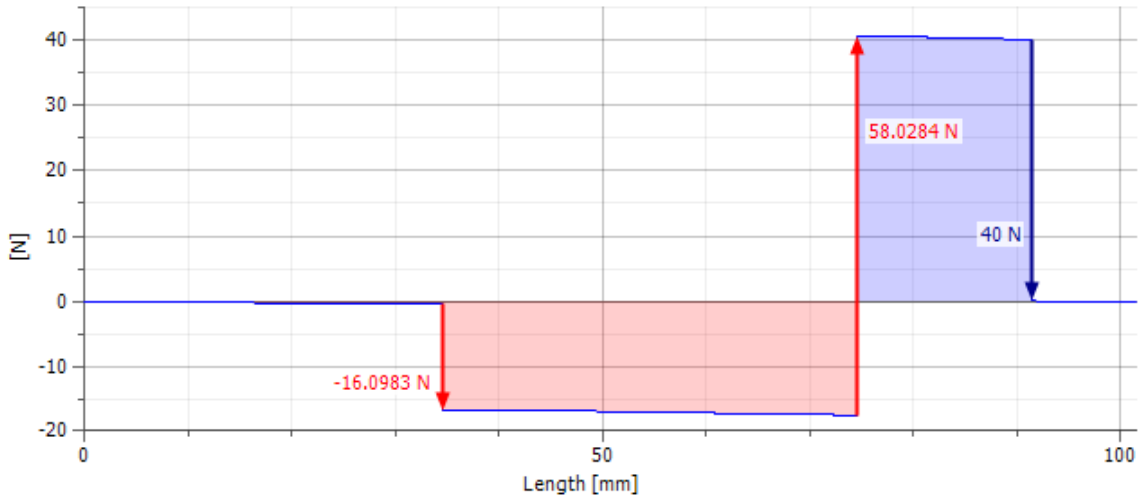

Figure A.1 Shear Force, YZ Plane.

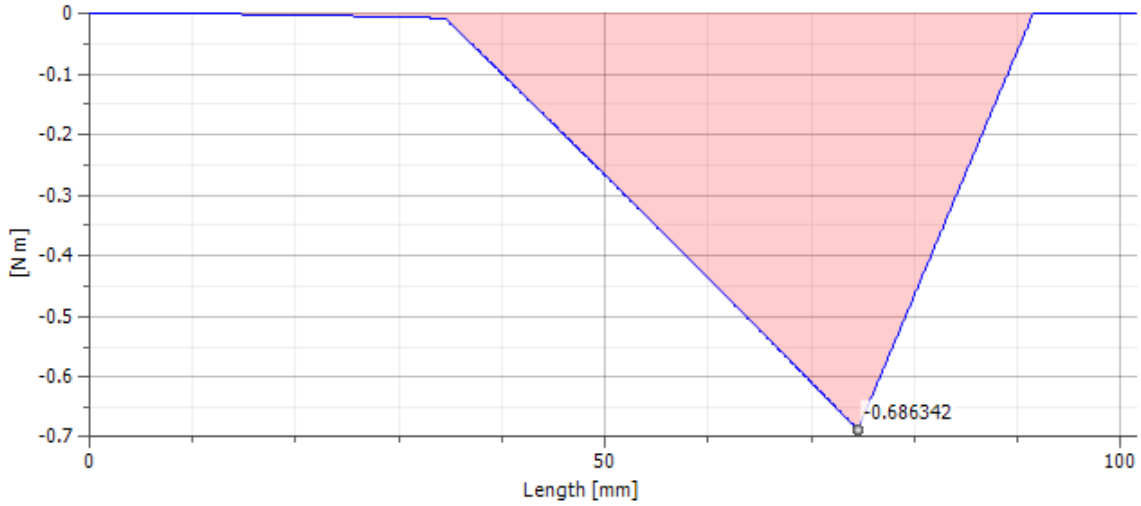

Figure A.2 Bending Moment, YZ Plane.

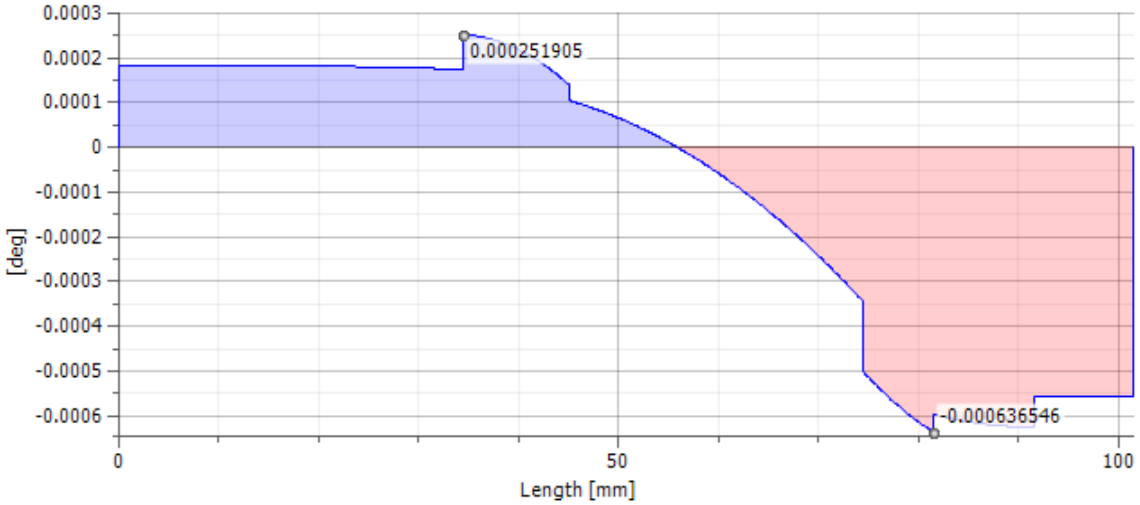

Figure A.3 Deflection Angle, YZ Plane.

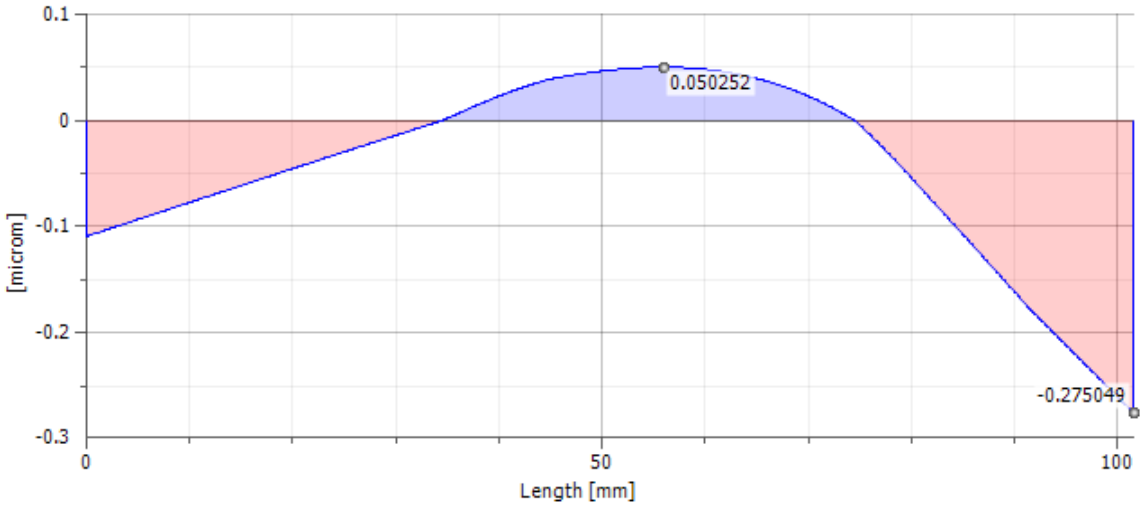

Figure A.4 Deflection.

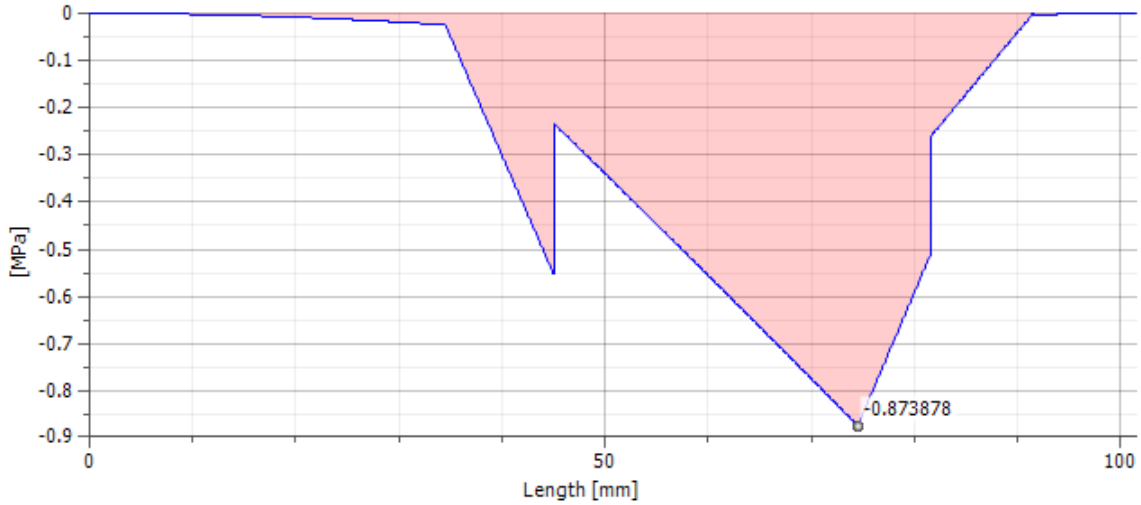

Figure A.5 Bending Stress, YZ Plane.

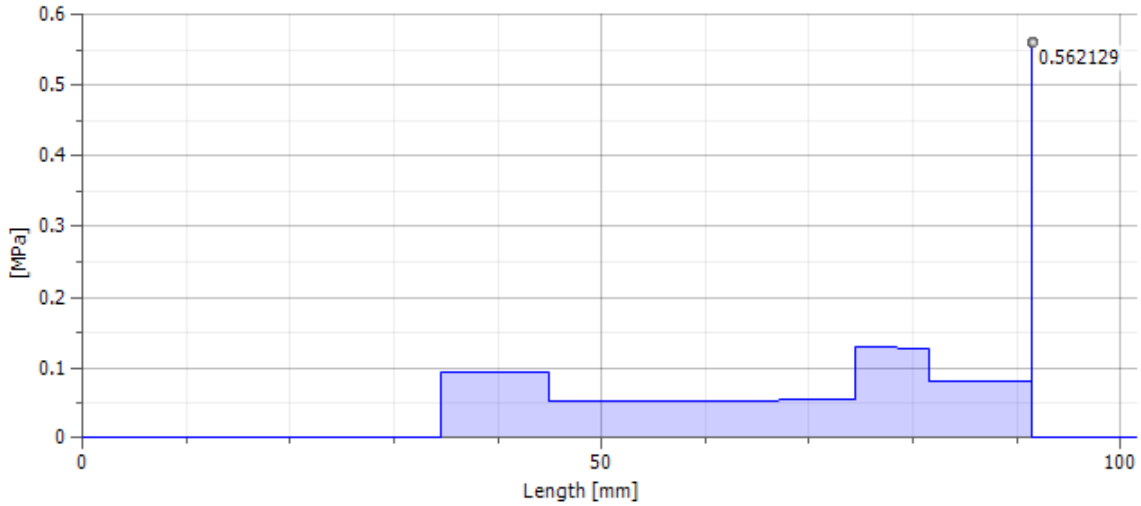

Figure A.6 Shear Stress.

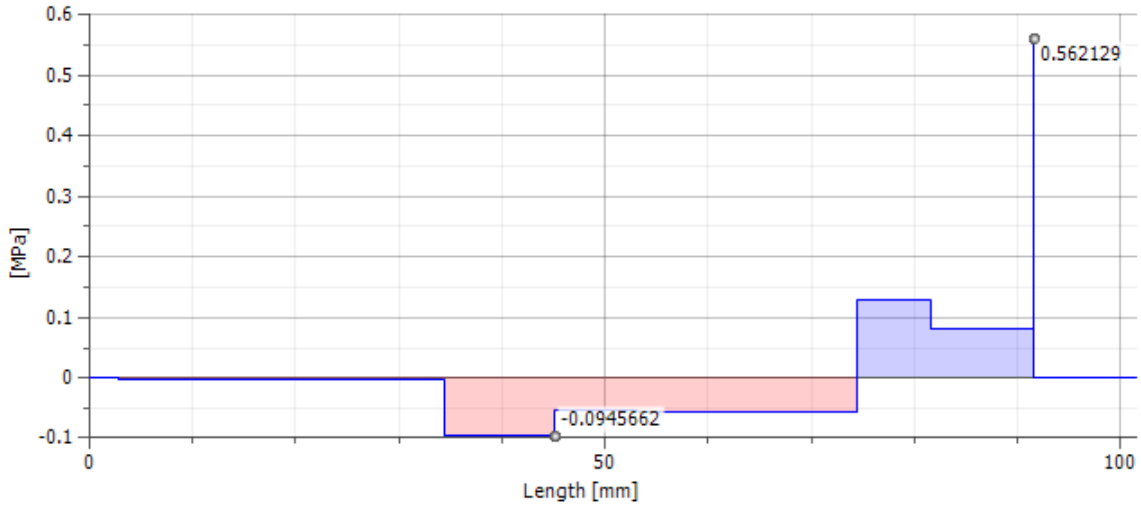

Figure A.7 Shear Stress, YZ Plane.

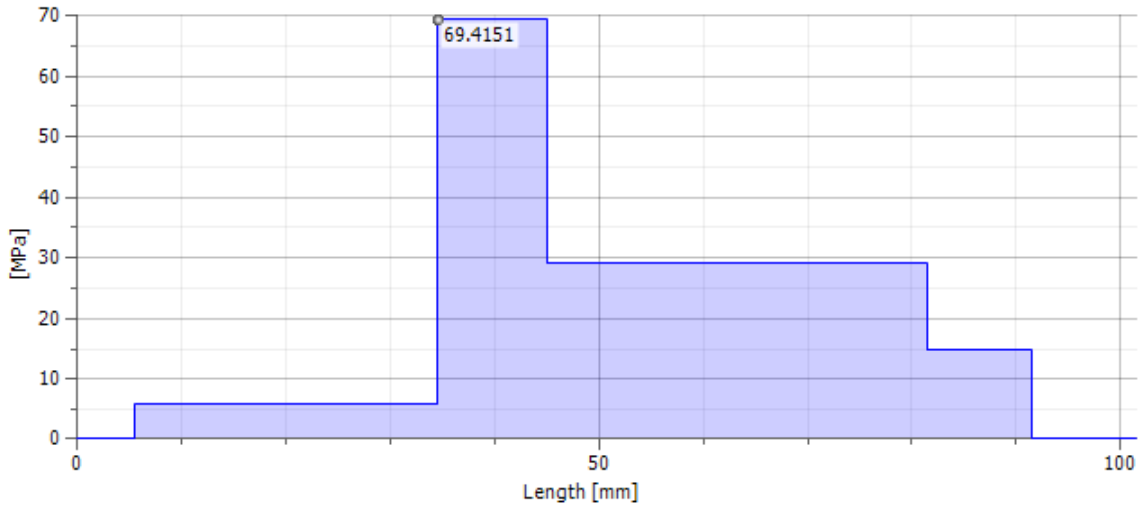

Figure A.8 Torsional Stress.

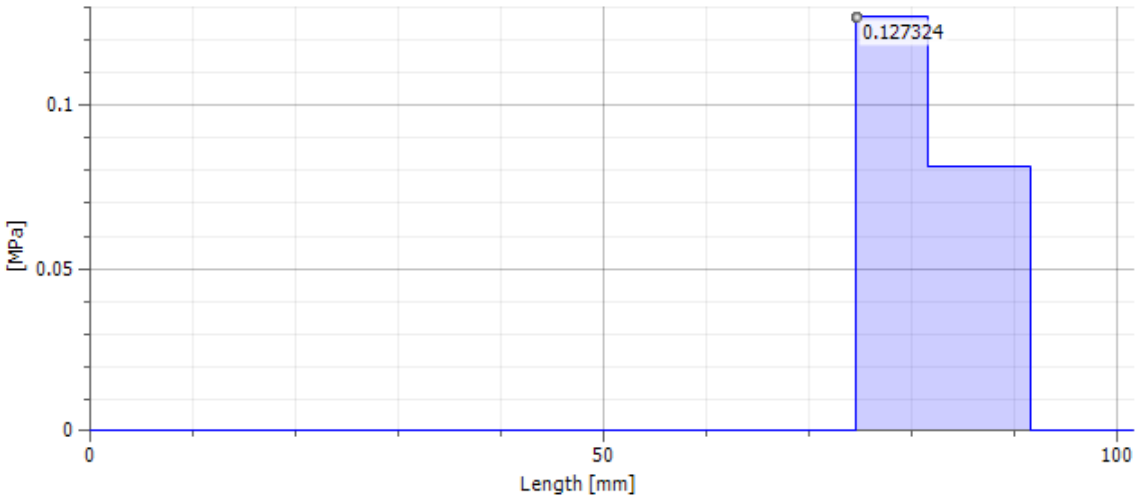

Figure A.9 Tension Stress.

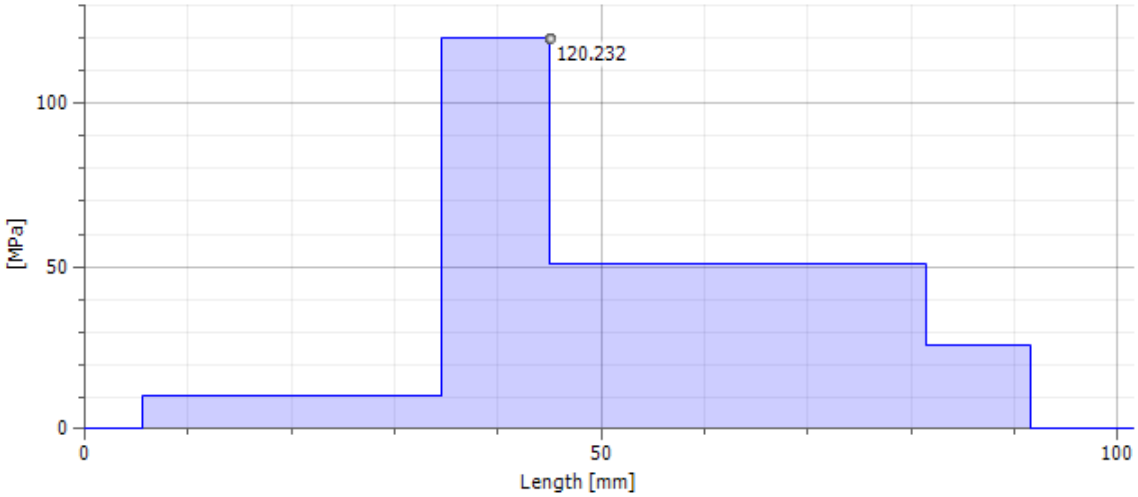

Figure A.10 Reduced Stress.

Appendix B – Additional Data Tables

Table B.1 Force Sensor Calibration Data

Load (N)	Voltage(V)
0	0.24
0.755	0.32
12.77	1.53
24.45	2.71
36.24	3.79
46.91	4.97

Table B.2 Force Sensor Calibration Data

Motor Control Signal (V)	Measured Torque (Nm)
2.0	0.049
2.1	0.200
2.2	0.434
2.3	0.553
2.4	0.697
2.5	0.829
2.6	0.962
2.7	1.066
2.8	1.159
2.9	1.246
3.0	1.332
3.1	1.412
3.2	1.483
1.9	-0.123
1.8	-0.397
1.7	-0.562
1.6	-0.724
1.5	-0.899
1.4	-1.070
1.3	-1.209
1.2	-1.339
1.1	-1.464
1.0	-1.588

Table B.3 Weights and biases of ANN for INV1 model.

		Connected Neuron Hidden Layer 1				
		HN1	**HN2**	**HN3**	**HN4**	**HN5**
Connecting Neuron Input Layer	**IN1**	1.410443	-1.072925	-1.230943	4.257275	2.711458
	IN2	0.410994	4.021710	2.030566	-0.526137	-0.006512
	IN3	-1.881347	1.947973	0.214683	-6.877818	4.19866
	BN1	0.375735	-1.354144	0.980373	-0.945610	-0.583716
		Connected Neuron Hidden Layer 2				
		HN6	**HN7**	**HN8**	**HN9**	**HN10**
Connecting Neuron Hidden Layer 1	**HN1**	-0.448406	-0.439373	0.508634	0.171192	0.032192
	HN2	1.777050	22.706066	1.278113	1.261680	12.571058
	HN3	0.022448	-0.320256	0.790523	0.213899	-0.650581
	HN4	-0.867658	2.392657	-0.985621	0.216422	6.004337
	HN5	-1.267491	-0.823562	-0.492983	0.226712	-1.636014
	BN2	0.063252	-1.926301	1.001872	0.172204	-1.835995
		Connected Neuron Output Layer				
		ON1				
Connecting Neuron Hidden Layer 2	**HN5**	-0.300370				
	HN6	0.287880				
	HN7	0.685481				
	HN8	0.700475				
	HN9	0.326765				
	BN3	0.637087				

Table B.4 Weights and biases of ANN for INV2 model.

		Connected Neuron Hidden Layer 1				
		HN1	**HN2**	**HN3**	**HN4**	**HN5**
Connecting Neuron Input Layer	**IN1**	0.322546	0.021538	-1.689767	-0.451583	-0.081006
	IN2	-2.094913	-0.947167	19.264496	6.601645	-2.191380
	IN3	-0.449591	-0.489720	3.854236	2.249239	-0.474172
	BN1	0.496184	0.105072	-4.040916	-2.658832	0.171960
		Connected Neuron Hidden Layer 2				
		HN6	**HN7**	**HN8**	**HN9**	**HN10**
Connecting Neuron Hidden Layer 1	**HN1**	0.783043	9.961076	0.659584	1.461120	-2.469181
	HN2	1.194763	0.795733	1.241952	0.529709	0.241596
	HN3	0.848312	2.117206	0.880507	0.089521	0.051308
	HN4	-0.016658	-26.16582	-0.151828	-0.002898	0.158596
	HN5	1.099733	0.860093	1.267270	0.348937	0.337281
	BN2	0.180857	0.459334	0.172777	0.151188	-0.123260
		Connected Neuron Output Layer				
		ON1				
Connecting Neuron Hidden Layer 2	**HN5**	0.156539				
	HN6	-0.212835				
	HN7	-0.337036				
	HN8	-4.497675				
	HN9	-1.095248				
	BN3	0.784343				

Table B.5 RMSE and MAE for 5 trials of each position controller. Nominal loading condition, Region 1, cycloidal trajectory.

	Nominal: 0-90							
	RMSE (mm)				MAE (mm)			
Controller	ANNB	ALB	HANNB	HALTB	ANNB	ALB	HANNB	HALTB
Trial 1	0.061	0.077	0.026	0.024	0.203	0.220	0.095	0.074
Trial 2	0.061	0.075	0.021	0.023	0.153	0.227	0.075	0.087
Trial 3	0.049	0.059	0.024	0.033	0.164	0.168	0.107	0.114
Trial 4	0.047	0.060	0.022	0.025	0.173	0.170	0.092	0.086
Trial 5	0.047	0.062	0.034	0.028	0.126	0.181	0.121	0.123
Average	0.053	0.067	0.026	0.027	0.164	0.193	0.098	0.097

Table B.6 RMSE and MAE for 5 trials of each position controller. Nominal loading condition, Region 2, cycloidal trajectory.

	Nominal: 90-91-90							
	RMSE (mm)				MAE (mm)			
Controller	ANNB	ALB	HANNB	HALTB	ANNB	ALB	HANNB	HALTB
Trial 1	0.034	0.035	0.011	0.011	0.120	0.105	0.045	0.042
Trial 2	0.025	0.037	0.010	0.012	0.089	0.130	0.037	0.050
Trial 3	0.024	0.034	0.010	0.011	0.085	0.108	0.040	0.043
Trial 4	0.026	0.039	0.009	0.011	0.092	0.133	0.038	0.048
Trial 5	0.081	0.035	0.009	0.011	0.081	0.120	0.041	0.049
Average	0.038	0.036	0.010	0.011	0.093	0.119	0.040	0.046

Table B.7 RMSE and MAE for 5 trials of each position controller. Nominal loading condition, Region 3, cycloidal trajectory.

	Nominal: 90-45-0							
	RMSE (mm)				MAE (mm)			
Controller	ANNB	ALB	HANNB	HALTB	ANNB	ALB	HANNB	HALTB
Trial 1	0.043	0.048	0.021	0.018	0.159	0.158	0.100	0.063
Trial 2	0.044	0.054	0.021	0.021	0.151	0.180	0.093	0.103
Trial 3	0.043	0.052	0.025	0.022	0.167	0.172	0.110	0.107
Trial 4	0.045	0.047	0.018	0.027	0.226	0.157	0.065	0.118
Trial 5	0.052	0.053	0.022	0.018	0.182	0.156	0.089	0.072
Average	0.045	0.051	0.022	0.021	0.177	0.164	0.091	0.092

Table B.8 RMSE and MAE for 5 trials of each position controller. Nominal loading condition, Region 4, cycloidal trajectory.

	Nominal: 0-90-91-90-45-0							
	RMSE (mm)				**MAE (mm)**			
Controller	**ANNB**	**ALB**	**HANNB**	**HALTB**	**ANNB**	**ALB**	**HANNB**	**HALTB**
Trial 1	0.048	0.055	0.021	0.019	0.203	0.220	0.100	0.074
Trial 2	0.046	0.057	0.019	0.020	0.153	0.227	0.093	0.103
Trial 3	0.041	0.050	0.022	0.024	0.167	0.172	0.110	0.114
Trial 4	0.042	0.049	0.018	0.024	0.226	0.170	0.092	0.118
Trial 5	0.046	0.052	0.024	0.020	0.182	0.181	0.121	0.123
Average	0.045	0.053	0.021	0.021	0.186	0.194	0.103	0.106

Table B.9 RMSE and MAE for 5 trials of each position controller. –Inertia loading condition, Region 1, cycloidal trajectory.

	- Inertia: 0-90							
	RMSE (mm)				**MAE (mm)**			
Controller	**ANNB**	**ALB**	**HANNB**	**HALTB**	**ANNB**	**ALB**	**HANNB**	**HALTB**
Trial 1	0.204	0.211	0.099	0.080	0.503	0.435	0.312	0.232
Trial 2	0.205	0.213	0.081	0.074	0.348	0.353	0.189	0.152
Trial 3	0.202	0.203	0.092	0.080	0.361	0.322	0.222	0.231
Trial 4	0.203	0.204	0.086	0.073	0.363	0.344	0.219	0.143
Trial 5	0.200	0.212	0.085	0.105	0.355	0.362	0.216	0.386
Average	0.203	0.209	0.088	0.082	0.386	0.363	0.231	0.229

Table B.10 RMSE and MAE for 5 trials of each position controller. –Inertia loading condition, Region 2, cycloidal trajectory.

	- Inertia: 90-91-90							
	RMSE (mm)				**MAE (mm)**			
Controller	**ANNB**	**ALB**	**HANNB**	**HALTB**	**ANNB**	**ALB**	**HANNB**	**HALTB**
Trial 1	0.212	0.216	0.092	0.087	0.468	0.477	0.268	0.230
Trial 2	0.213	0.217	0.087	0.088	0.462	0.490	0.237	0.237
Trial 3	0.208	0.213	0.086	0.086	0.465	0.439	0.221	0.235
Trial 4	0.210	0.219	0.101	0.090	0.420	0.479	0.286	0.251
Trial 5	0.209	0.219	0.085	0.086	0.433	0.476	0.209	0.224
Average	0.211	0.217	0.090	0.087	0.450	0.472	0.244	0.235

Table B.11 RMSE and MAE for 5 trials of each position controller. –Inertia loading condition, Region 3, cycloidal trajectory.

	- Inertia: 90-45-0							
	RMSE (mm)				MAE (mm)			
Controller	ANNB	ALB	HANNB	HALTB	ANNB	ALB	HANNB	HALTB
Trial 1	0.145	0.147	0.076	0.061	0.335	0.369	0.335	0.210
Trial 2	0.142	0.149	0.064	0.061	0.353	0.334	0.208	0.176
Trial 3	0.145	0.150	0.070	0.060	0.345	0.322	0.223	0.185
Trial 4	0.155	0.150	0.070	0.064	0.445	0.364	0.266	0.199
Trial 5	0.148	0.150	0.063	0.063	0.315	0.307	0.190	0.224
Average	0.147	0.149	0.069	0.062	0.359	0.339	0.244	0.199

Table B.12 RMSE and MAE for 5 trials of each position controller. –Inertia loading condition, Region 4, cycloidal trajectory.

	- Inertia: 0-90-91-90-45-0							
	RMSE (mm)				MAE (mm)			
Controller	ANNB	ALB	HANNB	HALTB	ANNB	ALB	HANNB	HALTB
Trial 1	0.178	0.182	0.086	0.073	0.503	0.477	0.335	0.232
Trial 2	0.178	0.184	0.075	0.072	0.462	0.490	0.237	0.237
Trial 3	0.177	0.180	0.080	0.072	0.465	0.439	0.223	0.235
Trial 4	0.182	0.183	0.082	0.073	0.445	0.479	0.286	0.251
Trial 5	0.178	0.185	0.075	0.081	0.433	0.476	0.216	0.386
Average	0.178	0.183	0.079	0.074	0.462	0.472	0.259	0.268

Table B.13 RMSE and MAE for 5 trials of each position controller. +Inertia loading condition, Region 1, cycloidal trajectory.

	+ Inertia: 0-90							
	RMSE (mm)				MAE (mm)			
Controller	ANNB	ALB	HANNB	HALTB	ANNB	ALB	HANNB	HALTB
Trial 1	0.224	0.258	0.112	0.119	0.438	0.498	0.307	0.273
Trial 2	0.224	0.264	0.118	0.116	0.443	0.478	0.285	0.415
Trial 3	0.236	0.271	0.091	0.108	0.630	0.651	0.218	0.262
Trial 4	0.229	0.263	0.092	0.110	0.398	0.449	0.194	0.289
Trial 5	0.240	0.261	0.105	0.104	0.599	0.447	0.338	0.231
Average	0.230	0.263	0.104	0.111	0.501	0.505	0.268	0.294

Table B.14 RMSE and MAE for 5 trials of each position controller. +Inertia loading condition, Region 2, cycloidal trajectory.

	+ Inertia: 90-91-90							
	RMSE (mm)				MAE (mm)			
Controller	ANNB	ALB	HANNB	HALTB	ANNB	ALB	HANNB	HALTB
Trial 1	0.253	0.283	0.139	0.171	0.587	0.851	0.374	0.513
Trial 2	0.241	0.274	0.147	0.141	0.523	0.625	0.529	0.343
Trial 3	0.237	0.293	0.144	0.165	0.511	0.895	0.567	0.398
Trial 4	0.246	0.278	0.152	0.170	0.583	0.725	0.458	0.472
Trial 5	0.257	0.286	0.156	0.169	0.662	0.822	0.407	0.523
Average	0.247	0.283	0.148	0.163	0.573	0.784	0.467	0.450

Table B.15 RMSE and MAE for 5 trials of each position controller. +Inertia loading condition, Region 3, cycloidal trajectory.

	+ Inertia: 90-45-0							
	RMSE (mm)				MAE (mm)			
Controller	ANNB	ALB	HANNB	HALTB	ANNB	ALB	HANNB	HALTB
Trial 1	0.197	0.213	0.080	0.104	0.469	0.484	0.302	0.513
Trial 2	0.195	0.211	0.075	0.093	0.387	0.481	0.233	0.297
Trial 3	0.195	0.217	0.083	0.087	0.397	0.471	0.326	0.255
Trial 4	0.191	0.217	0.079	0.100	0.400	0.456	0.288	0.497
Trial 5	0.192	0.217	0.081	0.086	0.422	0.483	0.380	0.298
Average	0.194	0.215	0.080	0.094	0.415	0.475	0.306	0.372

Table B.16 RMSE and MAE for 5 trials of each position controller. +Inertia loading condition, Region 4, cycloidal trajectory.

	+ Inertia: 0-90-91-90-45-0							
	RMSE (mm)				MAE (mm)			
Controller	ANNB	ALB	HANNB	HALTB	ANNB	ALB	HANNB	HALTB
Trial 1	0.218	0.242	0.104	0.126	0.587	0.851	0.374	0.513
Trial 2	0.214	0.241	0.107	0.112	0.523	0.625	0.529	0.415
Trial 3	0.216	0.251	0.102	0.115	0.630	0.895	0.567	0.398
Trial 4	0.214	0.244	0.103	0.122	0.583	0.725	0.458	0.497
Trial 5	0.221	0.246	0.108	0.115	0.662	0.822	0.407	0.523
Average	0.217	0.245	0.105	0.118	0.597	0.784	0.467	0.469

Table B.17 RMSE and MAE for 5 trials of each position controller. Zero gravity loading condition, Region 1, cycloidal trajectory.

	Zero Gravity Loading Condition: 0-90							
	RMSE (mm)				MAE (mm)			
Controller	**ANNB**	**ALB**	**HANNB**	**HALTB**	**ANNB**	**ALB**	**HANNB**	**HALTB**
Trial 1	0.045	0.057	0.017	0.019	0.169	0.210	0.049	0.057
Trial 2	0.046	0.051	0.022	0.018	0.205	0.154	0.074	0.059
Trial 3	0.056	0.056	0.018	0.019	0.249	0.205	0.065	0.067
Trial 4	0.045	0.054	0.021	0.021	0.169	0.141	0.082	0.057
Trial 5	0.044	0.059	0.022	0.018	0.149	0.221	0.079	0.073
Average	0.045	0.057	0.017	0.019	0.169	0.210	0.049	0.057

Table B.18 RMSE and MAE for 5 trials of each position controller. Zero gravity loading condition, Region 2, cycloidal trajectory.

	Zero Gravity Loading Condition: 90-91-90							
	RMSE (mm)				MAE (mm)			
Controller	**ANNB**	**ALB**	**HANNB**	**HALTB**	**ANNB**	**ALB**	**HANNB**	**HALTB**
Trial 1	0.018	0.031	0.011	0.012	0.055	0.117	0.029	0.031
Trial 2	0.015	0.032	0.013	0.011	0.085	0.114	0.043	0.029
Trial 3	0.012	0.042	0.011	0.011	0.038	0.148	0.031	0.034
Trial 4	0.015	0.039	0.012	0.010	0.059	0.125	0.036	0.031
Trial 5	0.012	0.039	0.011	0.010	0.047	0.129	0.032	0.029
Average	0.015	0.037	0.012	0.011	0.059	0.127	0.035	0.031

Table B.19 RMSE and MAE for 5 trials of each position controller. Zero gravity loading condition, Region 3, cycloidal trajectory.

	Zero Gravity Loading Condition: 90-45-0							
	RMSE (mm)				MAE (mm)			
Controller	**ANNB**	**ALB**	**HANNB**	**HALTB**	**ANNB**	**ALB**	**HANNB**	**HALTB**
Trial 1	0.041	0.061	0.017	0.016	0.131	0.201	0.054	0.049
Trial 2	0.037	0.059	0.017	0.017	0.185	0.209	0.056	0.052
Trial 3	0.033	0.068	0.018	0.016	0.116	0.210	0.053	0.056
Trial 4	0.035	0.059	0.017	0.015	0.110	0.167	0.054	0.047
Trial 5	0.032	0.058	0.017	0.014	0.155	0.190	0.053	0.065
Average	0.036	0.061	0.017	0.016	0.135	0.196	0.054	0.054

Table B.20 RMSE and MAE for 5 trials of each position controller. Zero gravity loading condition, Region 4, cycloidal trajectory.

	Zero Gravity Loading Condition: 0-90-91-90-45-0							
	RMSE (mm)				MAE (mm)			
Controller	**ANNB**	**ALB**	**HANNB**	**HALTB**	**ANNB**	**ALB**	**HANNB**	**HALTB**
Trial 1	0.038	0.055	0.016	0.016	0.169	0.210	0.054	0.057
Trial 2	0.036	0.052	0.017	0.016	0.205	0.209	0.074	0.059
Trial 3	0.037	0.060	0.017	0.016	0.249	0.210	0.065	0.067
Trial 4	0.035	0.054	0.017	0.016	0.169	0.167	0.082	0.057
Trial 5	0.033	0.055	0.018	0.014	0.155	0.221	0.079	0.073
Average	0.036	0.055	0.017	0.016	0.198	0.204	0.069	0.063

Table B.21 RMSE and MAE for 5 trials of ANNB and ALTB position controllers. Zero gravity loading condition, sine trajectory.

	Zero Gravity Load: Sine			
	RMSE (mm)		MAE (mm)	
Controller	**ANNB**	**ALTB**	**ANNB**	**ALTB**
Trial 1	0.077	0.101	0.217	0.294
Trial 2	0.076	0.109	0.206	0.318
Trial 3	0.075	0.111	0.237	0.263
Trial 4	0.074	0.102	0.222	0.300
Trial 5	0.076	0.107	0.216	0.304
Average	0.076	0.106	0.220	0.296

Table B.22 RMSE and MAE for 5 trials of ANNB and ALTB position controllers. Nominal loading condition, sine trajectory.

	Nominal: Sine			
	RMSE (mm)		RMSE (mm)	
Controller	**ANNB**	**ALTB**	**ANNB**	**ALTB**
Trial 1	0.058	0.099	0.156	0.344
Trial 2	0.059	0.083	0.153	0.235
Trial 3	0.066	0.096	0.184	0.317
Trial 4	0.057	0.088	0.162	0.250
Trial 5	0.058	0.090	0.170	0.376
Average	0.060	0.091	0.165	0.305